OUKA
The University of Osaka
Institutional Knowledge Archive

Title	Dissipationless spin current and nonreciprocal heat transport in a Kitaev chiral spin liquid
Author(s)	瀧川, 大地
Citation	大阪大学, 2023, 博士論文
Version Type	VoR
URL	https://doi.org/10.18910/92218
rights	
Note	

The University of Osaka Institutional Knowledge Archive : OUKA

https://ir.library.osaka-u.ac.jp/

The University of Osaka

Dissipationless spin current and nonreciprocal heat transport in a Kitaev chiral spin liquid

DAICHI TAKIKAWA

MARCH 2023

Dissipationless spin current and nonreciprocal heat transport in a Kitaev chiral spin liquid

A dissertation submitted to
THE GRADUATE SCHOOL OF ENGINEERING SCIENCE
OSAKA UNIVERSITY
in partial fulfillment of the requirements for the degree of
DOCTOR OF PHILOSOPHY IN SCIENCE

BY

DAICHI TAKIKAWA

MARCH 2023

Abstract

α-$RuCl_3$ is a promising candidate material for the Kitaev spin liquid state where the half quantization of the thermal Hall effect, suggesting a topological character, has been observed. Motivated by the experimental observation of the half-quantized thermal Hall conductivity for the Kitaev spin liquid candidate material, α-$RuCl_3$ [1], we have investigated the effects of non-Kitaev exchange interactions, which exist in the real material, on the gapped chiral spin-liquid state realized in the case with an applied magnetic field. We have found two main contributions. First, we have found that off-diagonal exchange interactions significantly enhance the mass gap of Majorana fermions. This result explains the robust quantization of the thermal Hall conductivity observed in the experiment, as mentioned above. Second, we have found that the off-diagonal exchange interaction dramatically changes the Majorana band structure in the case of the antiferromagnetic Kitaev interaction and gives rise to a topological phase transition from a non-Abelian topological phase with the Chern number equal to 1 to an Abelian phase with the Chern number equal to 2, in which the Z2 vortices behave as Abelian anyons.

However, on the other hand, according to the later researches [2, 3], it was found that the sample quality strongly influences the thermal Hall experiment, and there is no agreement among researchers that a Majorana has been observed. Thus, we need more reliable approaches for detection of Majorana fermions than the observation of the half-quantized thermal Hall effect.

To resolve this issue, we first propose a more direct signature of a chiral Majorana edge mode which emerges in a universal scaling of the Drude weight of the edge spin Seebeck effect in the Kitaev model. Moreover, the absence of backscatterings in the chiral edge mode results in the generation of a dissipationless spin current in spite of an extremely short spin correlation length close to a lattice constant in the bulk. This result is experimentally observable and opens a way toward the spintronics application of Kitaev

materials. Second, we propose a non-reciprocal thermal transport induced by the Dzyaloshinskii-Moriya interaction at the edge of the chiral Kitaev spin liquid. We found that the non-reciprocal thermal transport is possible due to the inversion symmetry breaking and becoming asymmetric by combining with the Dzyaloshinskii-Moriya interaction and the magnetic field at the edge. This result paves a way toward new experimental studies about the nonequilibrium steady states of the Kitaev magnets.

Contents

1 Overview **1**

2 Quantum spin liquid **3**
2.1 Background 3
2.2 Purpose of this thesis 4

3 Kitaev spin liquid **7**
3.1 Kitaev Hamiltonian 8
3.1.1 The spectrum and the phase diagram 14
3.1.2 Properties of the A-phase 20
3.1.3 Gapped B-phase in the magnetic field 22
3.1.4 Flip of Z2 gauge fields due to the operation of spin operators 23
3.1.5 Thermal Hall effect by Majorana edge states. 28
3.1.6 Thermal conductivity from the bulk state. 29
3.1.7 Spin correlation function 33
3.2 Mott insulator with strong spin-orbit coupling 33
3.2.1 The effective Hamiltonian of the Kitaev magnets . . . 34

4 Non-Kitaev interaction **45**

5 Experimental studies on α-$RuCl_3$ **57**
5.1 Quantum thermal Hall effect 57
5.2 Specific heat 63
5.3 Inelastic neutron scattering 64
5.4 Raman scattering 67

6 Edge spin Seebeck effect **71**
6.1 Model set-up . . . 72
6.2 Definition of energy current and spin current . . . 73
6.3 Edge spin Seebeck effect . . . 75
6.3.1 Kubo formula . . . 75
6.3.2 Derivation of the conductivity . . . 76
6.3.3 Ballistic edge transport . . . 78
6.4 Conformal field theory description . . . 81
6.5 Application for spintronics . . . 85

7 Nonreciprocal transport of Kitaev spin liquid **87**

8 Conclusion **105**

Acknowledgement **107**

Publication **109**

Bibliography **111**

Chapter 1

Overview

Spin liquids have three important features: first, they are a new quantum phase, different from the conventional magnetic phase due to spontaneous symmetry breaking. This is called the topological ordered phase. The second feature is the presence of strong entanglement. In the topological ordered phase, the wavefunctions have long-range correlations. This state differs from the conventional long-range ordered phases, such as magnetic order, in that there is no spontaneous symmetry breaking, and local order parameters cannot characterize the topological ordered phase. This long-range correlation in the topological ordered phase is related to this strong quantum entanglement. Finally, spin fractionalization and anyons are emerging related to the presence of this strong entanglement. Fractionalization means that the fundamental degrees of freedom of an electron such as charge and spin are fractionalized. In particular, this thesis focuses on the Kitaev spin liquid. The Kitaev model describes this spin liquid, and we can acquire an exact solution of the ground state, and an anyon is expressed as an elementary excitation [4]. In particular, anyons showing Non-abelian statistics appear in the chiral spin liquid realized by applying a magnetic field. Experiments about this spin liquid have also been conducted extensively. Primarily, there have been reports of the observation of this anyon in experiments on the two-dimensional quantum thermal Hall effect [1]. Regarding applications, topological quantum computation using the anyons in this topological phase as quantum dots is actively studied worldwide.

In this thesis, we aimed to propose novel quantum phases and predictions of novel physical properties that realize non-Kitaev interactions in Kitaev candidate materials and to explore new heat transport phenomena in

Majorana particles. First, we investigated the effective Hamiltonian for the non-Kitaev interactions that appear in the Kitaev candidates. As a result, it is found that the Γ' term causes a topological phase transition and transforms to an Abelian phase. We also analyzed other non-Kitaev interactions and obtained the effective Hamiltonian. Moreover, we have proposed a spin Seebeck effect of the Kitaev model at the edge caused by mixing itinerant and gauge Majorana fermions. We analyze using the linear response theory and find that the Drude Weight shows the universal temperature scaling, which is peculiar to Majorana fermions. The spin Seebeck effect is a phenomenon in which a spin current flows when an external temperature gradient is applied. We find that a non-dissipative, ballistic spin current flows at the edge of the system. Since this effect is characterized by the temperature scaling, rather than the absolute value of the conductivity like the thermal Hall effect, the characteristic feature is expected to remain unchanged even when perturbed by other degrees of freedom such as phonons. The observation of this effect can be a smoking gun for the existence of Majorana fermions.

Chapter 2

Quantum spin liquid

2.1 Background

This chapter provides an overview of the quantum spin liquid. In 1973, Anderson first proposed the ground state of the liquid state in the antiferromagnet [5]. This is called the resonating valence bound(RVB) state. He attempted to realize quantum superposition states in the Heisenberg antiferromagnet in the s=1/2 triangular lattice model, where the spins are paired into singlet states. Also, he referred to the importance of frustration in stabilizing the quantum spin liquid. In 1987, Baskaran, Zou, and Anderson discussed a more concrete RVB state and identified the quasiparticle of the quantum spin liquid called the spinons [6]. In 1987, Kallmeyer and Laughlin proposed the chiral spin liquid state and introduced the fractional quantum Hall effect and topology in the quantum spin liquid [7]. Moreover, in 1989, Wen introduced the topological order in the quantum spin liquid [8]. After 2000, the quantum spin liquid tipping point was reached. In 2003, Kitaev realized the toric code phase, which is the topological phase and is essential to quantum computation [9]. This phase shows strong entanglement, and as mentioned in the chapter 1, this entanglement emerges the non-local excitation, anyons. In 2006, Kitaev proposed a honeycomb lattice model with the exact solution and showed the stable gapless and gapped quantum spin liquid phases [4]. This phase also shows strong entanglement and realizes some topological phases and anyons. After this proposal, theoretical and experimental studies about the Kitaev spin liquid are developed extensively.

Here we introduce basic properties of the quantum spin liquid. In the

quantum spin liquid states, spins of electrons are not aligned in the same direction at low temperatures and behave like a liquid due to strong quantum fluctuations. In the case of atoms, when the temperature is cooled, a phase transition occurs from a state where each atom moves in a different direction to a solid. A similar phase transition occurs for the spin degrees of freedom. At low temperature, "liquid," in which spin directions are random(disordered), changes into "solid," in which the spins are aligned in the same direction. Then, the system realizes magnetism, such as ferromagnetism. However, if the quantum fluctuations are sufficiently strong, the quantum spin-liquid state can be realized by quantum fluctuations. They do not have long-range magnetic order despite their strong spin correlation.

We can classify the phase using the order concept in the general spin systems and define the order parameter. On the other hand, the spin liquid states are the phase that the order parameters cannot classify, and as mentioned above, the phase has the correlations but does not have the order. Many spin systems show the long-range order at the temperature, which is predicted from the temperature scale of the interaction, and the elementary excitation is described using the spin wave approximation. On the other hand, the magnetic orders of the spin liquid states disappear due to strong quantum fluctuations. Therefore, the elementary excitation of the spin liquid states is the quasiparticle defined by the non-local and non-linear transformation of the spin operator (the fractional excitation).

Quantum spin liquids have been the focus of attention for many years, theoretically and experimentally. There are different types of spin liquids realized on various lattices. Examples include the triangular lattice type spin liquid CS_2CuCl_4, the Kagome lattice spin liquid $Ca_{10}Cr_7O_{28}$, $ZnCu_3(OH)_6Cl_2$ and the Kitaev spin liquid α-RuCl3. Recently, the Kitaev spin liquids have attracted much attention because of the possibility of applying them to the quantum computer with the use of the chiral Majorana fermions under the magnetic field. Next chapters, we focus on the Kitaev spin liquid states.

2.2 Purpose of this thesis

There are three purposes of this thesis: To investigate the effects of Majorana edge states in Kitaev magnets, to propose experiments that provide conclusive evidence for Majorana fermions, and to propose new applications for the Kitaev spin liquids. In the previous section, we describe the important

characteristics of quantum spin liquids. These are new quantum phases with strong quantum entanglement, and the phases possess anyons. In particular, the Kitaev honeycomb model realizes the ground state of the spin liquid, and there is strong entanglement. Moreover, this model realizes some kinds of topological phases. In recent years, candidate materials have been found, and experiments have been enriched. However, the properties of the Kitaev spin liquid state in real candidate materials have not yet been fully clarified. Therefore, we focus on understanding novel quantum phases induced by non-Kitaev interactions and the nature of the Majorana edge states in Kitaev candidate materials. For this purpose, we propose new transport phenomena characterizing chiral Majorana edge states, spin Seebeck effect, and nonreciprocal thermal transport. Our results also pave the way toward a new thermomagnetic application of the Kitaev spin liquid state.

Chapter 3

Kitaev spin liquid

The Kitaev magnet is expected to realize the spin liquid state, the exotic quantum condensate phase, and the Majorana quasiparticle which can be applied to quantum computation and is attaching much attention in the broad physical fields of material science and quantum information. Recent researches support that the α-$RuCl_3$ is a strong candidate material [4, 10, 11, 12, 13, 14, 15, 16, 17, 18, 19, 20, 21, 22, 23, 24, 25, 26, 27, 28, 29, 30, 31, 32, 33, 34, 35, 36, 37, 38, 39, 40, 41, 42, 43, 44, 45]. However, strong experimental evidences of the existence of the spin liquid state and the Majorana quasiparticle are still lacking. Therefore, it is an essential fundamental problem to explore the direct probe of the Majorana quasiparticle in the Kitaev spin liquid state.

The Kitaev model is a spin system in which Ising-like exchange interactions depending on bond directions act on $S = 1/2$ spins localized on each site of the honeycomb lattice. In terms of the Majorana fermion representation, the model is exactly solvable, and exhibits a quantum spin liquid state regardless of the system size [4]. When time-reversal symmetry is broken by an applied magnetic field, the system becomes a chiral spin liquid state with a chiral Majorana edge, resulting in the Ising topological order in the bulk. The observation of the half-quantized thermal Hall effect, which is a signature of chiral Majorana fermions, has been reported [1]. Although further experimental observations which support the half-quantization of the thermal Hall effect in α-$RuCl_3$ are accumulating [1, 2, 3], it is still an important issue to confirm the existence of Majorana fermions from different and more direct approaches.

In this chapter, first we explain the theoretical aspects of the Kitaev

model. Next, we introduce the Kitaev materials, including how to realize the Kitaev Hamiltonian in materials, and explain previous experiments to probe the Kitaev chiral spin liquid, focusing on the quantum thermal Hall effect.

3.1 Kitaev Hamiltonian

The Kitaev model is a precisely solvable spin model on a two-dimensional lattice and has the character that Non-Abelian anyons appear. Anyons are particles with impressive statistics (neither Bose nor Fermi), which can only occur in two dimensions. Quantum statistics may be understood as a unique interaction: when two particles interchange along specified trajectories, the overall quantum state is multiplied by $e^{i\phi}$. Using these anyons, we can perform the topological quantum calculation. Anyonic systems realize the quantum memory that is protected from decoherence[4]. Some quantum gates can be implemented by braiding. This implementation is exact and does not require explicit error correction[9]. Freedman, Larsen, and Wang [46] proved that we can perform universal quantum computation using certain types of non-Abelian anyons braiding. This is called topological quantum computation (TQC). TQC should have manageable scalability problems, unlike many other quantum computation proposals. Kitaev invented this model for the realization of TQC. The numerical calculation of the non-Abelian Berry phase for applications to the TQC is discussed in [47].

This model is a spin-1/2 system in which spins are located at the sites of a honeycomb lattice; see Fig.3.1. We define the sublattices; the black site is "odd," and the white site is "even." The Hamiltonian is as follows.

$$\mathcal{H}_K = -\sum_{\langle ij \rangle_\alpha} K_\alpha S_i^\alpha S_j^\alpha, \tag{3.1}$$

where S_i^α is an $\alpha = x,\ y,\ z$ component of an $S = 1/2$ spin operator at the ith site. Here, $\langle ij \rangle_\alpha$ denotes that the ith site and the jth site are the nearest-neighbor sites connected by an α-bond on the honeycomb lattice. α-bonds ($\alpha = x,\ y,\ z$) are defined as shown in Fig.3.1 of this thesis. First, we introduce a general spin-fermion transformation for representing spins by Majorana operators. A system with n fermionic modes is usually described by the destruction and creation operators a_k, $a_k^\dagger$(k=1,$\cdots$, n). Instead, we can use their linear combinations,

$$c_{2k-1} = a_k + a_k^\dagger,\ \ c_{2k} = -i(a_k - a_k^\dagger) \tag{3.2}$$

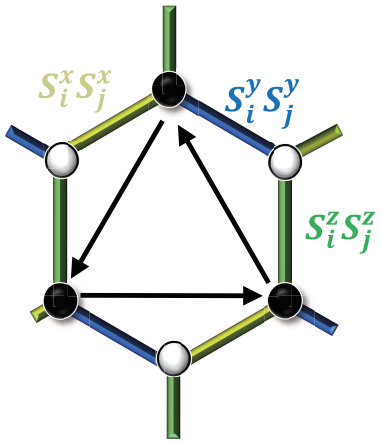


Figure 3.1: Structure of the Kitaev model. Yellow, blue, and green bonds represent x-, y-, and z-bonds, respectively. Black arrows represent the sign convention of the next-nearest-neighbor hoppings.

which are called Majorana operators. These operators c_j(j =1, $\cdots\cdots$, 2n) are Hermitian and obey the following relations.

$$c_i^\dagger = c_i,\ c_j^2 = 1,\ c_i c_j = -c_j c_i \text{ for} j \neq i \tag{3.3}$$

The ideal Kitaev Hamiltonian $\mathcal{H}_K$ is exactly solvable in terms of the Majorana fermion representation by four Majorana operators b^x, b^y, b^z, c.

$$S_j^x = \frac{\mathrm{i}}{2} b_j^x c_j,\ S_j^y = \frac{\mathrm{i}}{2} b_j^y c_j,\ S_j^z = \frac{\mathrm{i}}{2} b_j^z c_j, \tag{3.4}$$

where b_j^α ($\alpha = x,\ y,\ z$) and c_j are Majorana fermion operators. These operator are satisfied $(S^\alpha)^\dagger = S^\alpha$, $(S^\alpha)^2$=1.

The Majorana operators act on the extended space. Thus we need to consider the physical space $\mathcal{M}$ and define the constraint condition to satisfy $D_i |\phi\rangle = |\phi\rangle$ with $D_i = b_i^x b_i^y b_i^z c_i$ for $|\phi\rangle \in \mathcal{M}$[4]. This D operator can also be considered a gauge transformation for the group $\mathbb{Z}_2$.

$$\begin{aligned} \hat{D}_i^2 &= b_i^x b_i^y b_i^z c_i b_i^x b_i^y b_i^z c_i, \\ &= -b_i^x b_i^y b_i^z b_i^x c_i b_i^y b_i^z c_i, \\ &= 1, \qquad (3.5) \\ D_i &= 1, -1. \qquad (3.6) \end{aligned}$$

This spin-Majorana transformation is correct since these spin operators commute with D, and the D operator holds the commutation relation between spin operators as follows.

$$\begin{aligned}
\hat{D}\,|\xi\rangle &= |\xi\rangle\,, && (3.7)\\
[D_i, \sigma_i^\alpha] &= [b_i^x b_i^y b_i^z c_i, i b_i^\alpha c_i],\ (\alpha = x, y, z)\\
&= -i b_i^x b_i^y b_i^z b_i^\alpha + i b_i^\alpha b_i^x b_i^y b_i^z,\\
&= 0, && (3.8)\\
[\sigma^x, \sigma^y]\hat{D}\,|\xi\rangle &= (b^x b^y - b^y b^x)\hat{D}\,|\xi\rangle\,,\\
&= 2 b^x b^y * b^x b^y b^z c\,|\xi\rangle\,,\\
&= -2 b^z c\,|\xi\rangle\,,\\
&= 2 i \sigma^z\,|\xi\rangle && (3.9)
\end{aligned}$$

A multi-spin spin system is described to satisfy the constraint condition at each spin.

$$[D_i, H\{\sigma_i^\alpha\}] \ = 0 \tag{3.10}$$

In terms of the Majorana representation, $\mathcal{H}_K$ is expressed as,

$$\mathcal{H}_K = \frac{\mathrm{i}}{4}\sum_{i,j} \hat{A}_{ij} c_i c_j. \tag{3.11}$$

The i, j of the summation take all the sites, and we define them as follows,

$$\hat{A}_{ij} = K^\alpha \hat{u}_{ij}^\alpha / 2, \tag{3.12}$$

$$\hat{u}_{ij}^\alpha = \mathrm{i} b_i^\alpha b_j^\alpha. \tag{3.13}$$

The $\hat{A}_{ij}$ comes into existence at the bond $\langle ij \rangle_\alpha$,and otherwise $\hat{A}_{ij} = 0$. The $\hat{u}_{ij}^\alpha$ operator is called as Z_2 gauge fields, because of

$$(\hat{u}_{ij}^\alpha)^2 = 1, \tag{3.14}$$

$$u_{ij}^\alpha = 1, -1. \tag{3.15}$$

and, $\hat{u}_{jk} = -\hat{u}_{jk},\ \hat{u}_{jk}^\dagger = \hat{u}_{jk}$.

Next, we describe the commutation relation of these operators to detect the ground states of this model. The operators $\hat{u}_{ij}^\alpha$ commute with the Hamiltonian $\mathcal{H}_K$, and can be replaced by eigenvalues ± 1.

$$[\hat{u}^{\alpha}_{ij}, H] = 0, \tag{3.16}$$
$$[\hat{u}^{\alpha}_{ij}, \hat{u}^{\alpha}_{lm}] = 0 \tag{3.17}$$

Thus, it seems that the the collection of all $\hat{u}^{\alpha}_{ij}$ is good quantum number and can be written $\mathcal{H}_K = \frac{\mathrm{i}}{4}\sum_{i,j} A_{ij}c_i c_j$. The ground state appears to be determined by $\hat{u}^{\alpha}_{ij}$, thus we denote it by $|\tilde{\Psi}_u\rangle$[4]. However, the anticommutation relation between the gauge operator D_j and $\hat{u}^{\alpha}_{ij}$ is zero.

$$\begin{aligned} \{\hat{u}_{jk}, D_j\} &= (-ib^{\alpha}_k)\left\{b^{\alpha}_j, b^x_j b^y_j b^z_j c_j\right\} \\ &= 0 \end{aligned} \tag{3.18}$$

Thus, the gauge operator D_j changes the value of $\hat{u}^{\alpha}_{ij}$. Therefore we need to project the $|\tilde{\psi}_u\rangle$ to the physical subspace and describe the following state.

$$|\Psi_w\rangle = \prod_j \left(\frac{1+D_j}{2}\right)\left|\widetilde{\Psi}_u\right\rangle \tag{3.19}$$
$$D_j|\Psi_w\rangle = |\Psi_w\rangle \tag{3.20}$$

w is the equivalence calss of u under the gauge trasnformations. For the planar lattice w is characterized by numbers $w_p = \pm 1$ defined as products of u_{jk} around hexagons[4].

$$\hat{w}_p = \Pi_{(j,k)\in p}\, \hat{u}_{jk} \quad (j \in \text{ even sublattice}, k \in \text{ odd sublattice }) \tag{3.21}$$

The j site is the even sublattice(white sites), and the k is the odd sublat-

tice(black sites). To check, we perform the calculation.

$$\begin{aligned}
\hat{w}_p \left|\Psi_w\right\rangle &= \hat{u}^z_{21}\hat{u}^x_{23}\hat{u}^y_{43}\hat{u}^z_{45}\hat{u}^x_{65}\hat{u}^y_{61} \prod_{i=1,2,3,4,5,6}\left(\frac{1+D_j}{2}\right)\prod_{j\neq i}\left(\frac{1+D_j}{2}\right)\left|\widetilde{\Psi}_u\right\rangle \\
&= \prod_{j\neq i}\left(\frac{1+D_j}{2}\right) Z_1 Z2\cdots Z_6\left|\widetilde{\Psi}_u\right\rangle \\
Z_1 &= \hat{u}_{21}\hat{u}_{61}\frac{1+D_1}{2} \\
&= \frac{1+D_1}{2}\hat{u}_{12}\hat{u}_{61} \\
\hat{w}_p \left|\Psi_w\right\rangle &= \prod_{j}\left(\frac{1+D_j}{2}\right)\hat{u}^z_{21}\hat{u}^x_{23}\hat{u}^y_{43}\hat{u}^z_{45}\hat{u}^x_{65}\hat{u}^y_{61}\left|\widetilde{\Psi}_u\right\rangle \\
&= w_p \left|\Psi_w\right\rangle \qquad (3.22) \\
w_p &= u^z_{21}u^x_{23}u^y_{43}u^z_{45}u^x_{65}u^y_{61} = \pm 1 \qquad (3.23)
\end{aligned}$$

Moreover, using the Eq. (3.16), we can check $[\hat{w}_p, \mathcal{H}_k] = 0$ and $[\hat{w}_p, D_l] = 0$ by similar calculation. Also, between the different honeycomb plaquettes, the w operator is diffrent sector $[\hat{w}_{p_1}, \hat{w}_{p_2}] = 0$. Conclusively, we can define the eigen state. w_p is interpreted as the magnetic flux through the plaquette p. If $w_p = -1$, we say the plaquette carries a vortex, and this product is not gauge-invariant[4].

From the properties of the alternating matrix of the Hamiltonian $\mathcal{H}_k$, we can exactly seek the ground energy. We transformed the spin model $\mathcal{H}_K$ Eq. (3.1) to $\mathcal{H}_K = \frac{\mathrm{i}}{4}\sum_{i,j} A_{ij}c_i c_j$. A is real skew-symmetric matrix of size n =2m because of A_{ij} = -A_{ji} from Eq. (3.12),(3.13).

The definition of the skew-symmetric matrices is $A^{\mathsf{T}} = -A$. From the nature of the skew-symmetric matrices, the eigenvalue always pairs $\pm\lambda$ and is impossible to diagonalize by a real matrix as follows,$A = Q\Sigma Q^{\mathsf{T}}$ where is orthogonal and

$$\Sigma = \begin{bmatrix} 0 & \lambda_1 & & & \\ -\lambda_1 & 0 & & \mathbf{0} & \\ & & 0 & \lambda_2 & \\ & \mathbf{0} & -\lambda_2 & 0 & \\ & & & & \ddots \end{bmatrix} \qquad (3.24)$$

for real positive definite λ_k.We take the eigen vectors as the $A\mathbf{P}_i = -i\lambda_i\mathbf{P}_i$ and $A\overline{\mathbf{P}}_i = i\lambda_i\overline{\mathbf{P}}_i$,Thus, if we decide the $Q = [\mathrm{Im}(\mathbf{P}_1), \mathrm{Re}(\mathbf{P}_1), \mathrm{Im}(\mathbf{P}_2), \cdots, \mathrm{Re}(\mathbf{P}_n)]$, the A matrix can be block diagonalized.

The Kitaev matrix A_{ij} is n=2m dimensional skew-symmetric matrix. The coefficient of the $\frac{1}{4}$ is because of establishing the Lie algebra as follows by using $[c_ic_j, c_lc_k] = -\delta_{i,l}2c_jc_k - \delta_{i,k}2c_lc_j$ and $A_{jk} = -A_{kj}$,

$$[-i\mathcal{H}(A), -i\mathcal{H}(B)] = \frac{1}{16}\sum_{ijlk} A_{ij}B_{lm}[c_ic_j, c_lc_k], \tag{3.25}$$

$$= \frac{1}{4}\sum_{ijk} A_{ij}B_{jk}[c_ic_k] - \frac{1}{4}\sum_{ijk} B_{ij}A_{jk}[c_ic_k], \tag{3.26}$$

$$= -i\mathcal{H}([A, B]). \tag{3.27}$$

To find the ground state of the Hamiltonian Eq. (3.11), we reduce it to a canonical form using the block diagonalization [4],

$$\mathcal{H}(A) = \frac{i}{2}\sum_{k}^{m} E_k b_k^{'} b_k^{"} = \sum_{k}^{m} E_k(a\dagger_k a_k - \frac{1}{2}) \tag{3.28}$$

Here, the energy is $\mathrm{E}_k \geqq 0$ and $b_k^{'}$,$b_k^{"}$ are nomral Majorana modes, and $(a_k)^\dagger$ and a_k are the corrspoding creation and annihilation operators.

$$a_k^\dagger = \frac{1}{2}(b_k^{'} - ib_k^{"}), a_k = \frac{1}{2}(b_k^{'} + ib_k^{"}). \tag{3.29}$$

The normal Majorana modes $b_k^{'}$,$b_k^{"}$ are defined using the orthogonal matrix $\mathrm{Q}\in$ O(2m) of block diagonalization of the Kitaev matrix A_{ij}.

$$(b_1^{'}, b_1^{"}, b_2^{'}, b_2^{"}, .., b_m^{'}, b_m^{"}) = (c_1, c_2, \cdots c_{2m-1}, c_{2m})Q \tag{3.30}$$

These normal modes are the Majorana fermion as follows, $\lambda =', "$ and Q^λ is the column vector of the orthogonal matrix Q.

$$\{b_k^\lambda, b_m^\nu\} = \{\sum_l c_l Q_l^{2k-1+\lambda}, \sum_n c_n Q_n^{2m-1+\nu}\} = 2\delta_{2k-1+\lambda,2m-1+\nu} \tag{3.31}$$

The ground state is defined by satisfying the condition,

$$a_k\,|\psi\rangle = 0 \textbf{ for all k}. \tag{3.32}$$

The ground energy is,

$$E_0 = -\frac{1}{2}\sum_{k=1}^{m} E_k = -\frac{1}{4}\,\mathrm{Tr}\,|iA|. \tag{3.33}$$

And, we can derive the Majorana correlation function of the ground state $|\psi\rangle$. The B matrix is also real skew-symmetric and satisfies $B^2 = -1$.

$$B = -i\mathrm{sgn}(iA) = Q \begin{bmatrix} 0 & 1 & & & \\ -1 & 0 & & \mathbf{0} & \\ & & 0 & 1 & \\ & \mathbf{0} & -1 & 0 & \\ & & & & \ddots \end{bmatrix} Q^{\mathsf{T}} \tag{3.34}$$

Using this B matrix, we can transform the condition Eq. (3.32),

$$a_k\,|\psi\rangle = \frac{1}{2}(b_k^{'} + ib_k^{"})\,|\psi\rangle = 0, \tag{3.35}$$

$$\Rightarrow \sum_l P_{lk}c_l\,|\psi\rangle = 0,\ \ \hat{P}_{jk} = \frac{1}{2}(\delta_{jk} - iB_{jk}). \tag{3.36}$$

B corresponds to a pairing between Majorana modes.

The matrix P in Eq. (3.36) is called the spectral projector from the 2m-dimensional complex space to the m-dimensional subspace spanned by the eigenvectors of iA corresponding to negative eigenvalues ($B\mathbf{P}_i = -i\lambda_i\mathbf{P}_i$) [4]. Using this projection operator Eq.(3.36), we can find the Majorana correlation functions. Wick's formula is established in the second and fourth-order correlations below.

$$\langle\psi|\,c_jc_k\,|\psi\rangle \;=\; 2P_{kj} \tag{3.37}$$

$$\langle\psi|\,c_ic_jc_lc_m\,|\psi\rangle \;=\; 4P_{ij}P_{lm} - 4P_{li}P_{mj} + 4P_{mi}P_{lj} \tag{3.38}$$

3.1.1 The spectrum and the phase diagram

The previous section describes the ground state and how to find it. The global ground state does not change due to the signs fo of the Kitaev exchange interaction K_α because changes of the sign can make up for the changes of the corresponding variables u_{jk}. Moreover, even with the fixed u, the ground

state energy does not depend on signs [4]. For example, in the case of the changing from K_z to $-K_z$, we consider a change as corresponding u_{jk} for all z-bonds under satisfying the condition that the gauge-invariant quantities w_p are constant. To perform a gauge transformation to $u_{jk} = 1$, Kitaev defines the gauge transformation operator in the yellow region,Ω_z of Fig.3.2, and this operator changes the Majorana operators at sites $\Omega_z(c_l \longmapsto -c_l)$.

$$R_z = \prod_{j \in \Omega_z} \sigma_j^z \tag{3.39}$$

$$R_z \left|\psi\right\rangle = -\left|\psi\right\rangle, R_z c_l \left|\psi\right\rangle = -c_l \left|\psi\right\rangle \tag{3.40}$$

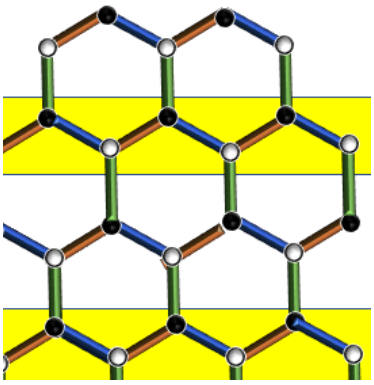


Figure 3.2: The yellow region,Ω_z

Above all, we can keep the sign of Kitaev exchange interactions when discussing the ground state energy and the excitation spectrum.

For $K^\alpha > 0$, in the ground state, we can put $\hat{u}_{ij}^\alpha \to 1$, and hence, $\hat{A}_{ij}^\alpha \to K^\alpha/2$. This choice of u_{jk} minimizes the ground state energy. It is shown that the energy is minimum when the vortex-free field configuration, $w_p = 1$ for all plaquettes p proving due to Lieb theorem [48] with the numerical result shown in Fig.3.3 [4]. Fig.3.3 is calculated in the case $K_\alpha = 1$, and the energy of the vortex-free phase $\mathrm{E}_0 \approx -1.5746$ per unit cell. In all vortex pattern cases, the energy is positive, and The figure can show that the more vortexes are added, the more energy is increased. Throughout this paper, we use this flux-free approximation $u_{jk} = 1$, where j belongs to the even sublattice(white site), and k belongs to the odd sublattice(black site). Because it is a good approximation for the low-temperature region we are

$E_{vortex} \approx 0.1536$ $\Delta E \approx -0.04$  $\Delta E \approx -0.07$ 

	Phase	Vortex density	Energy per vortex	$\Delta E \approx -0.07$	Phase	Vortex density	Energy
1		1/1	0.067	8		2/4	0.085
2		1/2	0.104	9		3/4	0.078
3		1/3	0.124	10		1/4	0.167
4		2/3	0.124	11		3/4	0.099
5		1/3	0.078	12		1/4	0.101
6		2/3	0.090	13		2/4	0.092
7		1/4	0.136	14		3/4	0.096

Figure 3.3: Vortices are shown in yellow.[4]

interested in. Then, Eq. (3.11) is reduced to the Hamiltonian of free massless Majorana fermions, which can be diagonalized in the momentum representation since the system holds a translational symmetry. We represent the site index j as (s, λ), where s refers to a unit cell and λ to a position type inside the cell. The Hamiltonian is written down to the momentum representation by substituting the Majorana Fourier transformation.

$$c_{\mathbf{q},\lambda} = \frac{1}{\sqrt{2N}} \sum_{\mathbf{R}} \mathrm{e}^{-\mathrm{i}(\mathbf{q},\mathbf{R_s}+\mathbf{r}_\lambda)} c_{\mathbf{R}\lambda}, \tag{3.41}$$

$$c_{\mathbf{R},\lambda} = \sqrt{\frac{2}{N}} \sum_{\mathbf{q}} \mathrm{e}^{\mathrm{i}(\mathbf{q},\mathbf{R}+\mathbf{r}_\lambda)} c_{\mathbf{q}\lambda}, \tag{3.42}$$

where N is the total number of the unit cells. The commutation relation of the Majorana operator of the momentum representation is,

$$c^\dagger_{\mathbf{q},\lambda} = c_{-\mathbf{q},\lambda}, \tag{3.43}$$

$$c_{\mathbf{p},\mu} c^\dagger_{\mathbf{q},\lambda} + c^\dagger_{\mathbf{q},\lambda} c_{\mathbf{p},\mu} = \delta_{\mathbf{pq}} \delta_{\mu\lambda}. \tag{3.44}$$

The Hamiltonian is,

$$\begin{aligned} H &= \frac{\mathbf{i}}{2}\sum_{s,\lambda,t,\mu} A_{(s\lambda),(t\mu)} c_\lambda c_{t\mu} \ (\ A_{(s\lambda),(t\mu)} := K_{\alpha_{(s\lambda),(t\mu)}} u_{(s\lambda),(t\mu)}/2), \\ &= \frac{i}{2N}\sum_{s,\lambda,t,\mu} A_{(s\lambda),(t\mu)} \sum_{q_1,q_2} \mathrm{e}^{\mathbf{i}\mathbf{q_1},\mathbf{s}+\lambda} \mathrm{e}^{\mathbf{i}\mathbf{q_2},\mathbf{t}+\mu} c_{\mathbf{q_1},\lambda} c_{\mathbf{q_2}\mu}, \\ &= \frac{i}{2N}\sum_{r,\lambda,t,\mu} A_{(r\lambda),(0\mu)} \sum_{q_1,q_2} \mathrm{e}^{\mathbf{i}\mathbf{q_1},\mathbf{r}+\mathbf{t}+\lambda} \mathrm{e}^{\mathbf{i}\mathbf{q_2},\mathbf{t}+\mu} c_{\mathbf{q_1},\lambda} c_{\mathbf{q_2}\mu}, \\ &= \frac{i}{2}\sum_{r,\lambda,\mu} A_{(r\lambda),(0\mu)} \sum_{q} \mathrm{e}^{-\mathrm{i}\mathbf{q},\mathbf{r}+\lambda-\mu} c_{-\mathbf{q},\lambda} c_{\mathbf{q}\mu}, \\ &= \frac{i}{2}\sum_{\mathbf{q},\lambda,\mu} A_{\lambda,\mu}(\mathbf{q}) c_{-\mathbf{q},\lambda} c_{\mathbf{q}\mu}. \end{aligned} \tag{3.45}$$

The spectrum $\epsilon(\mathbf{q})$ is obtained by $iA(\mathbf{q})$.

$$A_{\lambda\mu}(\mathbf{q}) = \sum_r \mathrm{e}^{-\mathrm{i}(\mathbf{q},\mathbf{r}+\lambda-\mu)} A_{r\lambda,0\mu} \tag{3.46}$$

Thus, the result is,

$$H = \frac{1}{2}\sum_{\mathbf{q}} \begin{pmatrix} c_{-\mathbf{q}_0} c_{-\mathbf{q}_1} \end{pmatrix} \begin{pmatrix} 0 & if(\mathbf{q}) \\ -if^*(\mathbf{q}) & 0 \end{pmatrix} \begin{pmatrix} c_{\mathbf{q}_0} \\ c_{\mathbf{q}_1} \end{pmatrix}, \tag{3.47}$$

$$\varepsilon(\mathbf{q}) = \pm|f(\mathbf{q})|, \tag{3.48}$$

$$f(\mathbf{q}) = \frac{1}{2}\left(K_x \mathrm{e}^{\mathrm{i}(\mathbf{q},\mathbf{n}_1)} + K_y \mathrm{e}^{\mathrm{i}(-\mathbf{q},\mathbf{n}_2)} + K_z\right). \tag{3.49}$$

The $\mathbf{n_1}, \mathbf{n_2}, \mathbf{n_3}$ are respectively,

$$\vec{n_1} = \begin{pmatrix} \frac{1}{2}, \frac{\sqrt{3}}{2} \end{pmatrix}, \tag{3.50}$$

$$\vec{n_2} = \begin{pmatrix} \frac{1}{2}, -\frac{\sqrt{3}}{2} \end{pmatrix}, \tag{3.51}$$

$$\vec{n_3} = -\vec{n_1} - \vec{n_2} = \begin{pmatrix} -1, 0 \end{pmatrix}. \tag{3.52}$$

This model has two phases, which are topologically trivial or non-trivial. Thus, The points $\epsilon(\mathbf{q}) = 0$ is essential, and the equation $f(\mathbf{q}) = 0$ has solutions when the conditions are satisfied as follows.

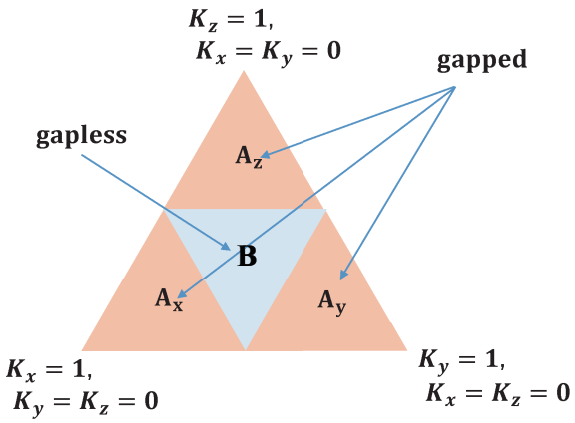


Figure 3.4: Phase diagram of the Kitaev model. The orange region is the gapped A-phase, while the blue region is the gapless B-phase.

$$|K_x| \leq |K_y| + |K_z|, |K_y| \leq |K_x| + |K_z|, |K_z| \leq |K_x| + |K_y| \tag{3.53}$$

There are two solutions, and this region is called B-phase, shown in Fig.3.4. In Fig.3.4 of this thesis , A-phase is a gapped toric code phase, while B-phase is a gapless phase. The gapped phase A_x,A_y,A_z are distinguished algebraically, and the continuous phase transition from A phase to another phase is not allowed [4]. In the case of $K_x = K_y = K_y$, the zero points in the gapless phase are given by,

$$\mathbf{q}_0 = \frac{1}{3}\mathbf{q}_1 + \frac{2}{3}\mathbf{q}_2, \tag{3.54}$$

$$-\mathbf{q}_0 = \frac{2}{3}\mathbf{q}_1 + \frac{1}{3}\mathbf{q}_2, \tag{3.55}$$

where the system is the $\mathbf{q}_{1,2}$ is the reciprocal lattice vector of the parallelogram, and the reciprocal lattice belongs to a torus. The basis is defined as,

$$\mathbf{a_1} = \mathbf{n_1}, \mathbf{a_2} = -\mathbf{n_2}. \tag{3.56}$$

When $|K_x|$ and $|K_y|$ decrease under $|K_z|$ constant until $|K_x| + |K_y| = |K_z|$ is established, zeros $\mathbf{q}_0$,$-\mathbf{q}_0$ come close and combine and disappear in the

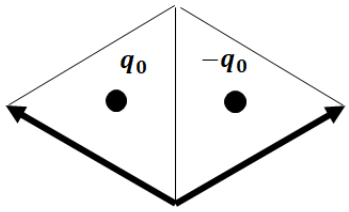


Figure 3.5: Zeros.

region of the parallelogram in Fig.3.5. Since the two zero points come close and become one, by Nielsen-Ninomiya theorem [49], the Chern number is canceled, and the phase becomes topologically trivial.

At the zero points, the spectrum of the B phase has become linear, like the Dirac band.

$$\epsilon(\mathbf{q}) \approx \pm\frac{\sqrt{3}}{2}|K|\sqrt{(\delta q_x)^2 + (\delta q_y)^2} \tag{3.57}$$

$$\delta q_x = q_x - q_{0x}, \delta q_x = q_y - q_{0y} \tag{3.58}$$

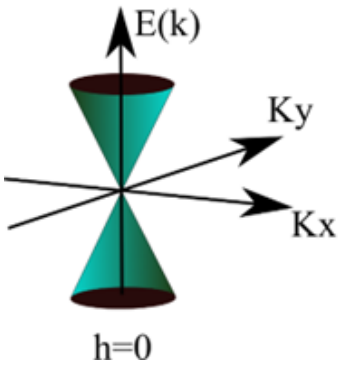


Figure 3.6: The spectrum of the Dirac like.

3.1.2 Properties of the A-phase

In the A-phase, the system functions as the toric code [9]. The toric code is an Abelian anyon model which protects the quantum information from errors. To accomplish the universal quantum computation, we need to employ non-topological operations, such as spin measurements [50, 51]

First, we show the case of A_z phase $|K_x| + |K_y| < |K_z|$, and the the result of perturbation therory at the $|K_x|, |K_y| << |K_z|$. The Hamiltonian is $\mathcal{H} = \mathcal{H}_0 + V$. The $\mathcal{H}_0$ is the non-perturbation term, and V is the perturbation.

$$\mathcal{H}_0 = -K_z \sum_{\langle jk \rangle_z} \sigma_j^z \sigma_k^z, \tag{3.59}$$

$$V = -\sum_{\alpha=x,y} K_\alpha \sigma_j^\alpha \sigma_k^\alpha. \tag{3.60}$$

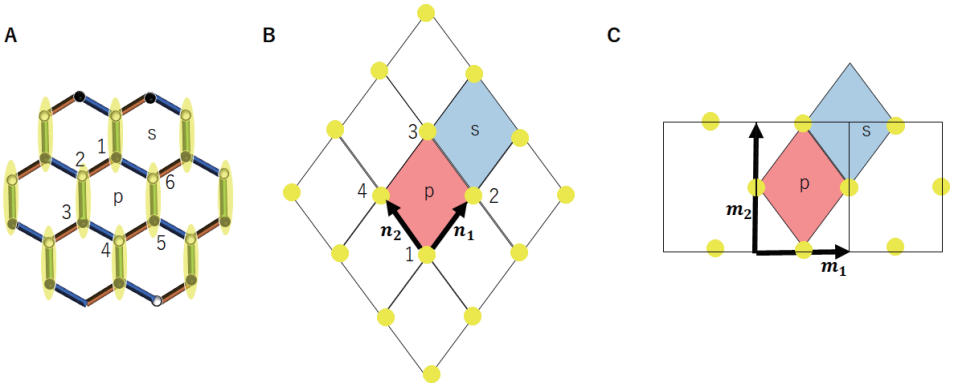


Figure 3.7: Reducton of the model. Strong links in the original model (A) become effective spins (B), which are associated with the links of a new lattice (c) [4]

Here, we consider only the case of $K_z > 0$ because of the analogy. The Z-bond spin pairs are aligned up and up or down and down; however, the direction is not fixed at every bond. Thus, the initiating state of the $K_x = K_y = 0$ degenerates. This ground energy is $E_0 = -NK_z$, where N is the number of unit cells, and we consider the Z-bond spin pair as the effective spin and the effective Hamiltonian in Fig.3.7(B). This effective Hamiltonian acts in the space of effective spins. In Kitaev'paper[4], using the general Green function formalism, the effective Hamiltonian is defined as,

$$\mathcal{H}_{eff} = E_0 + \Sigma(E_0) \tag{3.61}$$
$$\Sigma(E) = \gamma^{\dagger}(V + VG_0^{'}(E)V + VG_0^{'}(E)VG_0^{'}(E)V...)\gamma \tag{3.62}$$

γ is the projection onto the ground subspace of $\mathcal{H}_0$, and the eigenvector is $|m\rangle = |mm\rangle$, where $m =\uparrow$ or $\downarrow$. As a result, first-order term $\mathcal{H}^1$ and third-order term $\mathcal{H}^3$ is vanished. We show the other term,

$$\mathcal{H}_{eff}^{(2)} = -N\frac{{K_x}^2 + {K_y}^2}{4K_z}, \tag{3.63}$$
$$\mathcal{H}_{eff}^{(4)} = -\frac{K_x^2 K_y^2}{16K_z^3}\sum_p Q_p \tag{3.64}$$
$$Q_p = \sigma^y_{left(p)}\sigma^y_{right(p)}\sigma^z_{up(p)}\sigma^z_{down(p)} \tag{3.65}$$

Here, we briefly describe the method of perturbation. In the case of that $\sigma_2^x\sigma_3^y$ in Fig.3.7(a), the effective spin becomes $\sigma^y_{eff_4}$ in Fig.3.7(b),

$$\langle m^{'}|\,\sigma_x\sigma_y\,|m\rangle = [\sigma^y_{eff}]_{m'm} \tag{3.66}$$

Using this, the second-order term is allowed in the case only that other V returns to the original state because $\sigma_i^{x,y}\sigma_j^{x,y}$ flips the two spin. The intermediate energy $E_m = -(N-2)K_z + 2K_z$. The Q operator of the four-order term is the set of the effective spin. Due to counting the patterns where the spin operators $\sigma^\alpha\sigma^\alpha$ acts in the rhombus lattice of Fig.3.7(b), we get the coefficient,

$$\frac{1}{16} = \frac{-1}{128} * 8 + \frac{1}{64} * 8 \tag{3.67}$$

Here, we used Eq. (3.66) and $\sigma^y\sigma^x = -i\sigma^z$. The result of the case of $K_z < 0$ is the same, the effective Hamiltonian of A-phase is,

$$\mathcal{H}_{eff} = -K_{eff}\left(\sum_{\text{vertices}} Q_s + \sum_{\text{plaquetts}} Q_p\right), \tag{3.68}$$
$$K_{eff} = \frac{K_x^2 K_y^2}{16|K_z|^3},\ Q_p = \sigma^y_{left(p)}\sigma^y_{right(p)}\sigma^z_{up(p)}\sigma^z_{down(p)} \tag{3.69}$$

Constructing a new lattice in Fig.3.7(c) and performing a unitary transformation, the Hamiltonian can be written as follows,

$$U = \Pi_{\text{horizontallinks}} X_j \Pi_{\text{verticallinks}} Y_k, \tag{3.70}$$

$$\mathcal{H}'_{eff} = U\mathcal{H}_{eff}U^{\dagger} = -K_{eff}\left(\sum_{\text{vertices}} A_s + \sum_{\text{plaquetts}} B_p\right) \tag{3.71}$$

where $A_s = \Pi_{\text{vertices}}\sigma_j^x$, $B_p = \Pi_{\text{plaquettes}}\sigma_k^z$. This unitary transformation breaks the translational symmetry of the Kitaev model [4], and thus, A_z phase and the toric code [9] are the unitary equivalence.

3.1.3 Gapped B-phase in the magnetic field

In the B-phase, when a magnetic field $\vec{h} = (h_x, h_y, h_z)$ satisfying $h_x h_y h_z \neq 0$ is applied to the system, the Zeeman interaction,

$$\mathcal{H}_2 = -\sum_i (h_x S_i^x + h_y S_i^y + h_z S_i^z) \tag{3.72}$$

generates a mass gap for Majorana fermions in the bulk due to the time-reversal symmetry(TRS). The system exhibits a chiral spin liquid state with a chiral Majorana edge state, where the Majorana fermion itinerants along with the edge of the system in Fig.3.8. The edge state is known to be

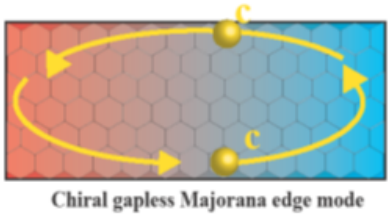


Figure 3.8:

described by the Ising conformal field theory (CFT) [4]. The mass term is obtained by a perturbative calculation up to the third order in h_α, which leads to three-spin interaction terms. We show the perturbation theory of the Kitaev model in the B-phase.

3.1.4 Flip of Z2 gauge fields due to the operation of spin operators

Here, we consider effects of the operation of spin operators on the eigenstate of flux operators, $\hat{w}$ Eq. (3.19), using the following relations:

$$[\sigma^z, D] = [ib^z c, b^x b^y b^z c] = 0. \tag{3.73}$$

As a result,

$$\sigma_j^z |\Psi_w\rangle = \Pi_k \frac{1+D_k}{2} |\phi\rangle , \tag{3.74}$$

$$|\phi\rangle := \sigma_j{}^z |\Psi_u\rangle . \tag{3.75}$$

where $|\Psi_w\rangle$ and $|\Psi_u\rangle$ are, respectively, the eigenstates of flux operators, and that of Z_2 gauge fields $\hat{u}$. We also define a state $|\phi\rangle$ that is an excited state with a flipped Z_2 gauge field. Note that the following relation hold:

$$\begin{aligned} \left[\sigma_i{}^\alpha, \hat{u}_{kl}^\beta\right] &= \left[ib_i{}^\alpha c_i, ib_k{}^\beta b_l{}^\beta\right] \\ &= -2\delta_{\alpha\beta}\delta_{ik} b_l{}^\alpha c_i + 2\delta_{\alpha\beta}\delta_{il} b_k{}^\alpha c_i. \end{aligned} \tag{3.76}$$

Using this relations, one can see that $|\phi\rangle$ is actually a state with a flipped eigenvalue of $\hat{u}^z$:

$$\begin{aligned} \hat{\mathbf{u}}_{jk}^z |\phi\rangle &= \hat{\mathbf{u}}_{jk}^z \sigma_j{}^z |\Psi_u\rangle \\ &= -\sigma_j{}^z \hat{\mathbf{u}}_{jk}^z |\Psi_u\rangle \\ &= (-u_{jk}^z) |\phi\rangle . \end{aligned} \tag{3.77}$$

This shows that the eigenvalue of the Z_2 gauge field for the $|\phi\rangle$ state is opposite to that of the $|\Psi_u\rangle$ state. The flip of the Z_2 gauge field also occurs in the case that the spin operator σ^z acts on the other site of $\langle jk\rangle_z$,

$$\left|\phi'\right\rangle := \sigma_k{}^z |\Psi_u\rangle , \tag{3.78}$$

$$\begin{aligned} \hat{\mathbf{u}}_{jk}^z \left|\phi'\right\rangle &= \hat{\mathbf{u}}_{jk}^z \sigma_k{}^z |\Psi_u\rangle \\ &= -\sigma_k{}^z \hat{\mathbf{u}}_{jk}^z |\Psi_u\rangle \\ &= (-u_{jk}^z) \left|\phi'\right\rangle . \end{aligned} \tag{3.79}$$

Using the perturbation theory, we can look up the effective Hamiltonian acting on the vortex-free sector.

$$\Sigma(E) = \Pi_0(V + VG_0^{'}(E)V + VG_0^{'}(E)VG_0^{'}(E)V...)\Pi_0 \tag{3.80}$$

The first-order $\mathcal{H}^1_{eff}$ vanishes trivially, and the second-order $\mathcal{H}^2_{eff}$ remains; however, it preserves the TRS does not give the mass term. Thus we consider the third-order term.

$$H^{(3)}_{eff} = \Pi_0(VG_0^{'}(E)VG_0^{'}(E)V)\Pi_0,$$

where Π_0 is the project onto the vortex-free sector, and $G_0^{'}$ is the unperturbed Freen function with the vortex-free sector excluded. We assume that all intermediate states have energy $\Delta E \sim |K|$ above the ground state. Then $G_0^{'}$ can be replaced by,

$$G_0^{'}(E) = \frac{1}{E - H_0} \sim -\frac{1 - \Pi_0}{|K|}. \tag{3.81}$$

The third effective Hamiltonian is,

$$\mathcal{H}^{(3)} = -\Delta \sum_{i,j,k} S^x_i S^y_j S^z_k, \tag{3.82}$$

$$\Delta \sim \frac{h_x h_y h_z}{K^2}, \tag{3.83}$$

where $\langle ij \rangle_\alpha$, $\langle jk \rangle_\beta$ with $\alpha \neq \beta$, and we assume $K = K_x = K_y = K_z$ here for simplicity in the derivation of Δ. The summation tales the spin triples reflected the perturbation process.

For example, in Fig.3.9, the (a) is the vortex-free sector. The white shows the vortex-free sector $w_p = 1$. The (b) shows the intermediate state that the spin operator σ^z_1 acts at the "1" site. The yellow region shows the vortex $w_p = -1$. The red line shows the Z_2 spin flip $u_{ij} = -1$. The energy difference between the vortex-free sector and this intermediate state is $\Delta E \approx 0.27|K|$. The (c) shows the intermediate state that the spin operator σ^x_2 acts at the "2" site. The (d) shows the intermediate state that the spin operator σ^y_3 acts at the "3" site, and the final state becomes the vortex-free sector. On the other hand, we can consider the case that acts the spin operator σ^z_1,σ^x_4,σ^y_3, however, this corresponds to a four-fermion term, and therefore the spectrum does not directly change.

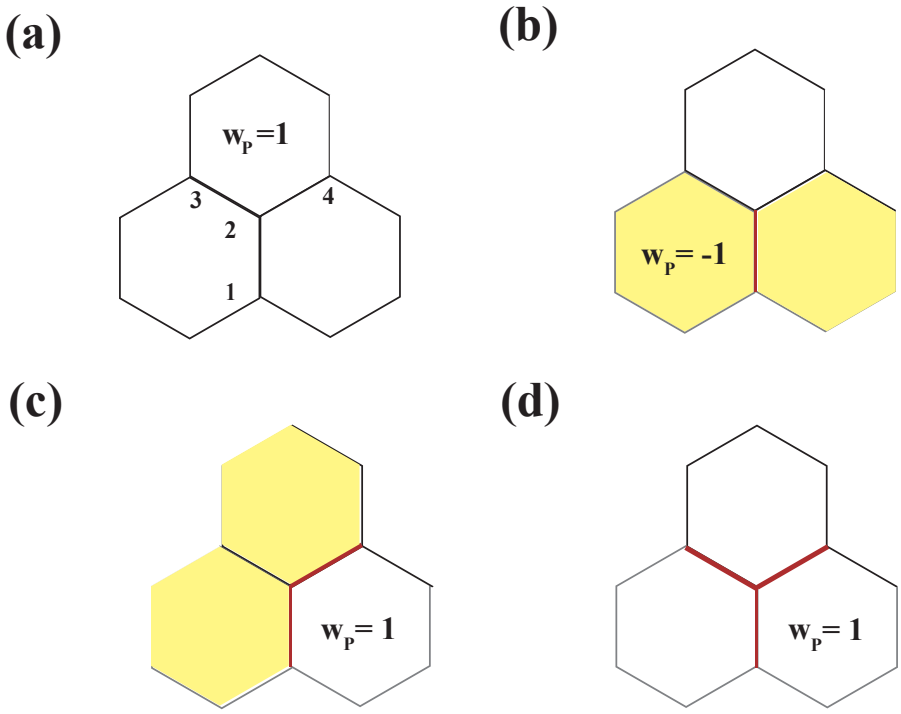


Figure 3.9: The intermediate state of the perturbation process.

In terms of Majorana fields, $\mathcal{H}^{(3)}$ is written as,

$$\begin{aligned} H^{(3)} &= -\frac{\Delta}{8}\sum_{j,k,l}\sigma_j^\alpha\sigma_l^\beta\sigma_k^\gamma D_j, \\ &= \frac{\Delta}{8}\mathbf{i}\sum_{\substack{\langle\mathbf{i},\mathbf{j}\rangle_\alpha \\ \langle\mathbf{j},\mathbf{k}\rangle_\gamma}} b_i^\alpha c_i b_j^\alpha b_j^\gamma b_k^\gamma c_k, \\ &= \frac{\Delta}{8}\mathbf{i}\sum_{\substack{\langle\mathbf{i},\mathbf{j}\rangle_\alpha \\ \langle\mathbf{j},\mathbf{k}\rangle_\gamma}} \hat{u}_{ij}^\alpha \hat{u}_{kj}^\gamma c_k c_i, \\ &= \mathrm{i}\frac{\Delta}{8}\sum_{i,m}\sum_{p=1,2,3}(-1)^m c_{i+\boldsymbol{n}_p}c_i. \end{aligned} \tag{3.84}$$

This effective Hamiltonian is a next-nearest-neighbor hopping term. The $\mathbf{n}_p$ is the direction of the hopping,

$$\vec{n_1} = \left(\ \tfrac{1}{2}, \tfrac{\sqrt{3}}{2}\ \right), \tag{3.85}$$

$$\vec{n_2} = \left(\ \tfrac{1}{2}, -\tfrac{\sqrt{3}}{2}\ \right), \tag{3.86}$$

$$\vec{n_3} = -\vec{n_1} - \vec{n_2} = \left(\ -1, 0\ \right), \tag{3.87}$$

and m=0 if the site i is on the even site(white site) of the honeycomb lattice, and m=1 if i is on the odd site(black site). The spectrum is given by,

$$H = \frac{1}{2}\sum_{\mathbf{q}}\left(\ c_{\mathbf{q}_1}^\dagger c_{\mathbf{q}_0}^\dagger\ \right)\begin{pmatrix}\Delta_q & if(q)\\ -if^*(q) & -\Delta_q\end{pmatrix}\begin{pmatrix}c_{q_1}\\ c_{q_0}\end{pmatrix}, \tag{3.88}$$

$$\Delta(\mathbf{q}) = 4\Delta\left(\sin(\mathbf{q},\mathbf{n}_1) + \sin(\mathbf{q},-\mathbf{n}_2) + \sin(\mathbf{q},\mathbf{n}_2-\mathbf{n}_1)\right), \tag{3.89}$$

$$\varepsilon(\mathbf{q}) = \pm\sqrt{|f(\mathbf{q})|^2 + \Delta(\mathbf{q})^2}. \tag{3.90}$$

This term yields the Majorana mass gap $\Delta_{Majorana} \sim \Delta$ in Fig3.10.

$$\Delta = \Delta(\mathbf{q}_0) = -\Delta(-\mathbf{q}_0) = 6\sqrt{3}\Delta \sim \Delta \tag{3.91}$$

It is noted that the mass gap term also arises from the perturbation in the non-Kitaev interaction Γ' [52, 53]. We stress, here, that in the vortex-free spin liquid state, the first-order corrections with respect to the Zeeman term

Eq. (3.72) vanish, and the gauge-field Majorana fermions b_j^α can be completely eliminated in the effective low-energy Hamiltonian in the bulk, i.e. the system can be described only in terms of matter Majorana fermions c_j. However, the situation drastically changes at open edges as described below, which is a key factor of dissipationless spin currents at the edges.

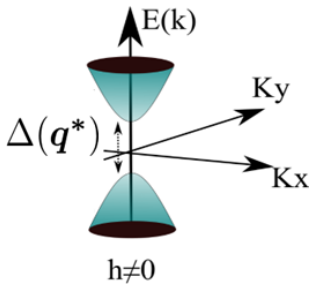


Figure 3.10: The gapped B-phase.

Next, we consider the Chern number of the 2D system, the Chern number is topological invariant and determines the edge mode chirality. We use the projection operator Eq. (3.36) in the momentum space,

$$\tilde{P}(q) = \frac{1}{2}(1 - \mathrm{sgn}(i\tilde{A}(q))) \tag{3.92}$$

$$= \frac{1}{2}\begin{bmatrix} 1 - \frac{\Delta}{\epsilon} & -i\frac{f(q)}{\epsilon} \\ i\frac{f(q)}{\epsilon} & 1 + \frac{\Delta}{\epsilon} \end{bmatrix} \tag{3.93}$$

The Chern number is defined as follows [4].

$$\nu = \frac{1}{2\pi i}\int \mathrm{Tr}\left(\tilde{P}d\tilde{P} \wedge d\tilde{P}\right) \tag{3.94}$$

$$= \frac{1}{2\pi i}\int \mathrm{Tr}\left(\tilde{P}(\frac{\partial\tilde{P}}{\partial q_x}\frac{\partial\tilde{P}}{\partial q_y} - \frac{\partial\tilde{P}}{\partial q_y}\frac{\partial\tilde{P}}{\partial q_x})\right)dq_x dq_y \tag{3.95}$$

$$= \frac{1}{2\pi i}\int \sum_{n,k=1,2} \tilde{P}_{nk}\hat{A}_{kn}dq_x dq_y \tag{3.96}$$

$$\hat{A}_{kn} = \sum_l \left[\frac{\partial\tilde{P}_{kl}}{\partial q_x}\frac{\partial\tilde{P}_{ln}}{\partial q_y} - \frac{\partial\tilde{P}_{kl}}{\partial q_x}\frac{\partial\tilde{P}_{ln}}{\partial q_y}\right] \tag{3.97}$$

The Chern number is always an integer. In this case, the Chern number is $\nu = \pm 1$ Moreover, the Chern number is zero in the Abelian phases A_α.

3.1.5 Thermal Hall effect by Majorana edge states.

A nonzero Chern number means that the system has gapless edge modes. There are Left moving mode and right moving one, and the relation is written,

$$\nu = \nu_{left-movers} - \nu_{right-movers}. \tag{3.98}$$

Usually, these modes cancel each other without special symmetry. Nonzero modes show the chirality. Chiral edge modes carry the energy; however, the chemical potential of this model is zero due to symmetry. Thus, we consider the energy current as the thermal current. We can measure this thermal transport in the experiment in the temperature region much smaller than the Majorana energy gap in the bulk$k_bT \ll \Delta_{Majorana}$ because the bulk excitation does not occur in this region. The energy current along the edge in the left direction is given by,

$$I = \frac{\pi}{12} C_- T^2. \tag{3.99}$$

c_- is a real number and depends on the bulk state, not the edge condition. We show the coefficient due to the simple calculation. The Majorana hamiltonian changes the form due to $\epsilon(-q) = -\epsilon(q)$,

$$\mathcal{H} = \frac{1}{2}\sum_q \epsilon(q) a_{-q} a_q = \sum_{q:\epsilon(q)>0} \epsilon(q) a_{-q} a_q \tag{3.100}$$

The energy current is given by,

$$I_1 = \int_{\epsilon(q)>0} n(q)\epsilon(q)v(q)\frac{dq}{2\pi} = \frac{\pi}{24}T^2 \tag{3.101}$$

The group velocity of the mode is $v(q) = \frac{d\epsilon}{dq}$, and n(q) is the Fermi distribution function. Due to considering the opposite direction propagation, we give $I = \frac{\pi}{24}\nu T^2$. In the quantum thermal Hall effect, according to the research of the chiral p-wave superconductivity [54, 55], the thermal Hall conductivity is quantized at the low-temperature region ($k_{\mathrm{B}}T \ll E_g$) from the

result of the bulk calculation. We will describe the experience of the quantized thermal Hall effect in more detail in the later chapter, the quantized thermal Hall conductivity is observed as follows.

$$\frac{\kappa_{xy}^{2D}}{T} = \frac{\pi {k_B}^2}{12} C_1(0) \tag{3.102}$$

$$C_1(0) = 1 \tag{3.103}$$

This equation means that when the thermal excitation is smaller than the bulk gap, the thermal conductivity is quantized, $C_1(0)$ is the Chern number.

3.1.6 Thermal conductivity from the bulk state.

In this section, we review previous studies on thermal transport in more detail based on Nasu, and Motome [29]. To understand the nature of the itinerant Majorana fermion, they investigate the thermal transport of the two-dimensional Kitaev model and both longitudinal and transverse thermal conductivities in the magnetic field using the linear response theory and the quantum Monte Carlo simulations[29]. Here, we briefly describe the derivation of thermal conductivity. First, we introduce the energy polarization operator using the Hamiltonian Eq. (3.11).

$$\mathbf{P}_E = \sum_{ij} \frac{\mathbf{r}_i + \mathbf{r}_j}{2} \widetilde{\mathcal{H}}_{ij} \tag{3.104}$$

Using the Eq. (3.27) and (3.42), the energy current operator is written down as follows,

$$\mathbf{J}_E = \frac{d\mathcal{P}_E}{dt} = \frac{i}{\hbar}[\widetilde{\mathcal{H}}, \mathbf{P}_E] \tag{3.105}$$

$$= \frac{1}{4} \sum_k [\mathbf{v}_k \mathcal{H}_k + \mathcal{H}_k \mathbf{v}_k]_{ss'} c^\dagger_{k,s} c_{k,s'} \tag{3.106}$$

$$v_{\mathbf{k}ss'} = \frac{1}{\hbar} \frac{\partial \mathcal{H}_{\mathbf{k}ss'}}{\partial \mathbf{k}} \tag{3.107}$$

where $v_{kss'}$ is the group velocity. The chemical potential is zero, and the energy current J_E is equivalent to the heat current J_Q. The longitudinal component $\kappa^{\mu\mu}$ is calculated from the Kubo formula.

$$\kappa^{\mu\mu}_{kubo}(\omega) = \frac{-2\pi\hbar}{TV}\sum_{\mathbf{k}nn'}|J^{\mu}_{Q\mathbf{k}nn'}|^2\frac{f(E_{\mathbf{k}n'})-f(E_{\mathbf{k}n})}{E_{\mathbf{k}n'}-E_{\mathbf{k}n'}}\delta(\hbar\omega+E_{\mathbf{k}n'}-E_{\mathbf{k}n}) \tag{3.108}$$

On the other hand, in the case of the transverse component $\kappa^{\mu\nu}$, we also need to consider the contribution of the gravitational magnetization [54, 56]. As a result, the zero-frequency component is as follows,

$$\kappa^{xy} = \frac{\pi T}{12}\frac{4\pi {k_B}^2}{V\hbar}\sum_{\mathbf{k}n}\int_{E_{\mathbf{k}n}}^{\infty} g(E)dE\Lambda(E), \tag{3.109}$$

$$\Lambda(E) = \sum_{n'\neq n} Im\frac{[{U_{\mathbf{k}}}^{\dagger}\partial\mathcal{H}_{\mathbf{k}}/\partial k_x U_{\mathbf{k}}]_{nn'}[{U_{\mathbf{k}}}^{\dagger}\partial\mathcal{H}_{\mathbf{k}}/\partial k_y U_{\mathbf{k}}]_{n'n}}{(E_{\mathbf{k}n}-E_{\mathbf{k}n'})^2} \tag{3.110}$$

$$g(E) = \frac{(\beta E)^2}{\pi^2/3}\left(-\frac{df(E)}{dE}\right) \tag{3.111}$$

They show that the longitudinal component of zero-(nonzero-)frequency $\kappa^{xx} = \lim_{\omega\to 0}\kappa^{xx}(\omega)$ has a broad peak around the higher- (lower-)T peak of the specific heat in the absence of the magnetic field in Fig.3.11(a). The specific heat of the Kitev model shows the two peaks depending on the temperature in black dots of Fig.3.11(a) reflecting the thermal fractionalization [20]. The first peak at T^* comes from the release of half of ln2 entropy related to the localized Z_2 fluxes W_p. On the other hand, the second peak at T^{**} comes from the rest half of the itinerant Majorana fermions [29]. Since the itinerant Majorana fermions carry the heat, they release their entropy.

In an applied magnetic field, the longitudinal componentκ^{xx} is unchanged. However, the transverse componentκ^{xy} in Fig.3.12(c)(d) shows the nonmonotonic temperature dependence and approaches the quantized conductivity at $T\to 0$. They report that this nonmonotonicity originates from the thermal excitation of the Z_2 fluxes from the ground state [29].

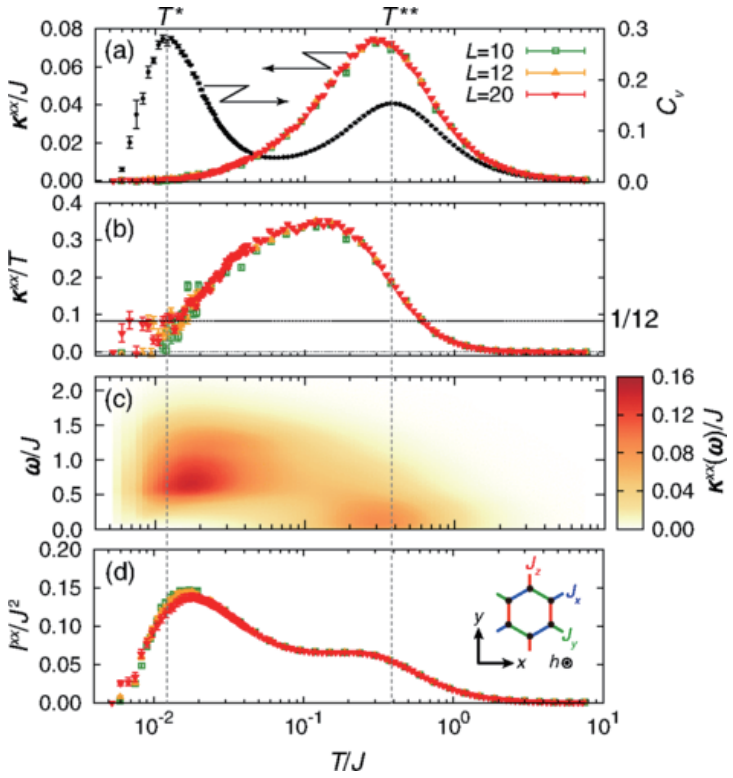


Figure 3.11: The temperature dependence of the longitudinal thermal conductivity.[29]

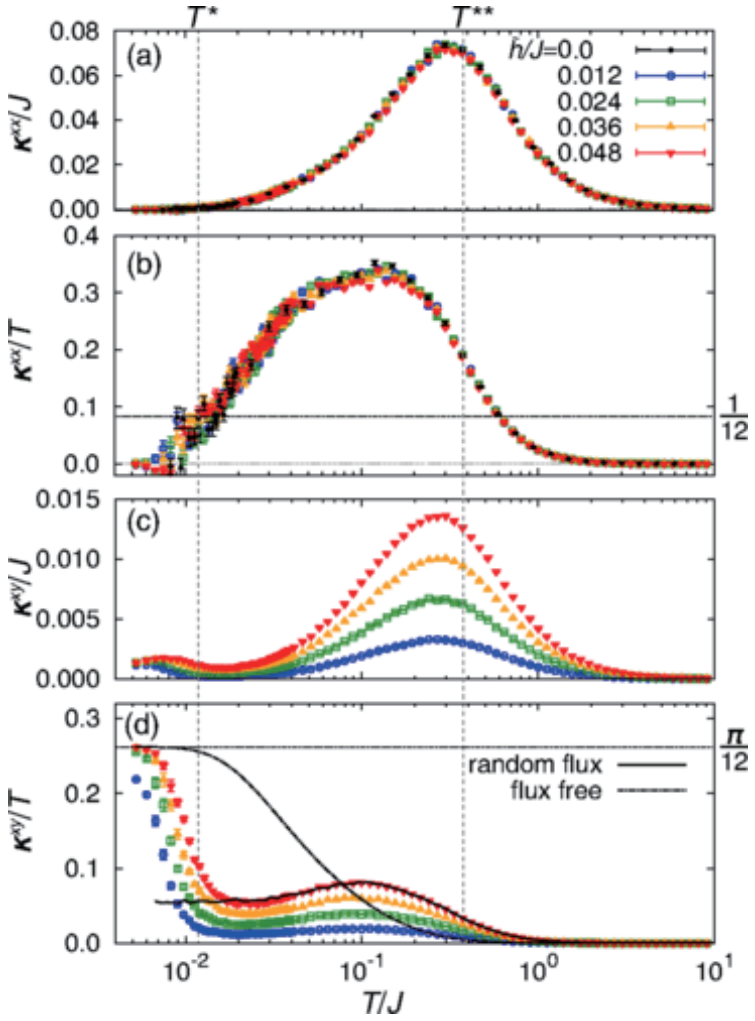


Figure 3.12: The temperature dependence of the thermal conductivity in the magnetic field.$\tilde{h} \sim \frac{h^3}{\Delta^2}$[29]

3.1.7 Spin correlation function

For any combination of the x,y, and z directions, we can show that the long-range order disappears at the ground state $|g\rangle$. For example, the following holds for about two points i, j at least the next nearest neighbor away.

$$\langle g|\sigma_i^\alpha \sigma_j^\beta|g\rangle = 0 \tag{3.112}$$

This is because $\sigma_i^\alpha |g\rangle$ and $\sigma_j^\beta |g\rangle$ are orthgonal to each other due to different eigenstate. Also, the higher-order spin correlation function shows no long-range order, which coincides with the nature of the quantum spin liquid state. In general, G. Baskaran et al. report the time-dependent spin correlation function of the Kitaev model[10, 57].

$$\langle g|\sigma_i^\alpha(t)\sigma_j^\beta|g\rangle = g_{\langle ij\rangle_\alpha}(t)\delta_{\alpha\beta} \tag{3.113}$$

This show that the Kitaev model only has the nearest neighbor spin correlation. For example, the equal time 2-spin correlation function for the bond$\langle ij\rangle_z$ is given by the analytic expression:

$$\langle \sigma_i^z \sigma_j^z\rangle = S^{zz}_{\langle ij\rangle_z}(0) = \frac{\sqrt{3}}{16\pi^2}\int_{Bz} cos\theta(k_1,k_2)dk_1dk_2, \tag{3.114}$$

where $cos\theta(k_1,k_2) = \frac{\epsilon_k}{E_k}$, $E_k = \sqrt{(\epsilon_k^2+\Delta_k^2)}$, in the Brillouin zone.$\epsilon = 2(J_x cosk_1 + J_y cosk_2 + J_z)$,$\Delta_k = 2(J_x sink_1 + J_y sink_2)$,$k_1 = \mathbf{k}\cdot\mathbf{n_1}$,$k_2 = \mathbf{k}\cdot\mathbf{n_2}$, and $\mathbf{n_{1,2}} = \frac{\sqrt{3}}{2}\mathbf{e_y} \pm \frac{1}{2}\mathbf{e_x}$ are unit vectors along x and y type bonds. At the poit, $J_x = J_y = J_z$, we get $S^{zz}_{\langle ij\rangle_\alpha}(0) = 0.52$.

3.2 Mott insulator with strong spin-orbit coupling

We explained the essential nature of the Kitaev model. This is the theoretical model. Next, we explain how to realize the Kitaev Hamiltonian in the candidate materials. This chapter aims to derive the effective Hamiltonian in the Kitaev magnet and combine the theoretical model with the actual materials. The origin of the effective Hamiltonian is the spin-orbit coupling and the electron correlation. According to the first-principles calculation ab initio, it is found that non-Kitaev interactions with non-negligible magnitude

compared to Kitaev interactions and Zeeman energies emerge [58, 59]. At the last of this chapter, we introduce the influence of non-Kitaev interactions in Kitaev magnetic materials.

3.2.1 The effective Hamiltonian of the Kitaev magnets

After a while from Kitaev's proposal, G. Jackeli and G. Khaliulin showed that the effective Hamiltonian in Mott insulators with strong spin-orbit coupling realizes the Kitaev model [60].

We consider an MX_6 octahedron in which transition metal ion M is surrounded by an ion X such as oxygen. Under this cubic symmetry crystal field, the d-orbitals of the transition metal ion split into t_{2g} and e_g orbitals in Fig.3.13 The t_{2g} orbital is six degenerate, and the e_g orbital is four degenerate, including the spin. When there are five electrons in the d-orbitals (e.g. Ir^{4+}) and the energy split between t_{2g}-e_g is sufficiently large, the lower spin state, which all d-electrons occupy the lower energy t_{2g}, realized. The t_{2g} orbital has the effective orbital angular momentum $l_{eff} = -1$. Considering the spin-orbit coupling, the effective total angular momentum $j_{eff} = s - l_{eff}$ is a good quantum number, and we can describe the ground state using the total angular momentum $(j_{eff})_z$. The operator s is considered a hole spin with pseudo-spin $s = 1/2$ for the one remaining t_{2g} orbital. Here t_{2g} orbital devides into the four degenerate $j_{eff} = 3/2$ state and two degenerate $j_{eff} = 1/2$ state. Therefore, the low energy state $j_{eff} = 3/2$ are all occupied, and the higher energy state $j_{eff} = 3/2$ are half-filling. The Mott insulator is realized when the Coulomb repulsion force is considered in this situation.

These two states of $j_{eff} = 1/2$ are Kramers doublets connected by a time-reversal symmetry operation. This means that they can be considered as the pseudo-spin $\tilde{s} = 1/2$.

$$\left| j_{eff} = \pm\frac{1}{2} \right\rangle = -\frac{1}{\sqrt{3}} \left| l^z = 0, s^z = \pm\frac{1}{2} \right\rangle + \frac{\sqrt{2}}{\sqrt{3}} \left| l^z = \mp 1, s^z = \mp\frac{1}{2} \right\rangle \quad (3.115)$$

We show Eq. (3.115) states in Fig.3.13 and express the eigenstates of the effective orbital angular momentum using the original d-orbitals basis[61],

$$\begin{aligned} \left| l^z_{eff} = 0 \right\rangle &= |d_{xy}\rangle \\ \left| l^z_{eff} = \pm 1 \right\rangle &= -\frac{i\,|d_{zx}\rangle \mp |d_{xy}\rangle}{\sqrt{2}} \end{aligned} \quad (3.116)$$

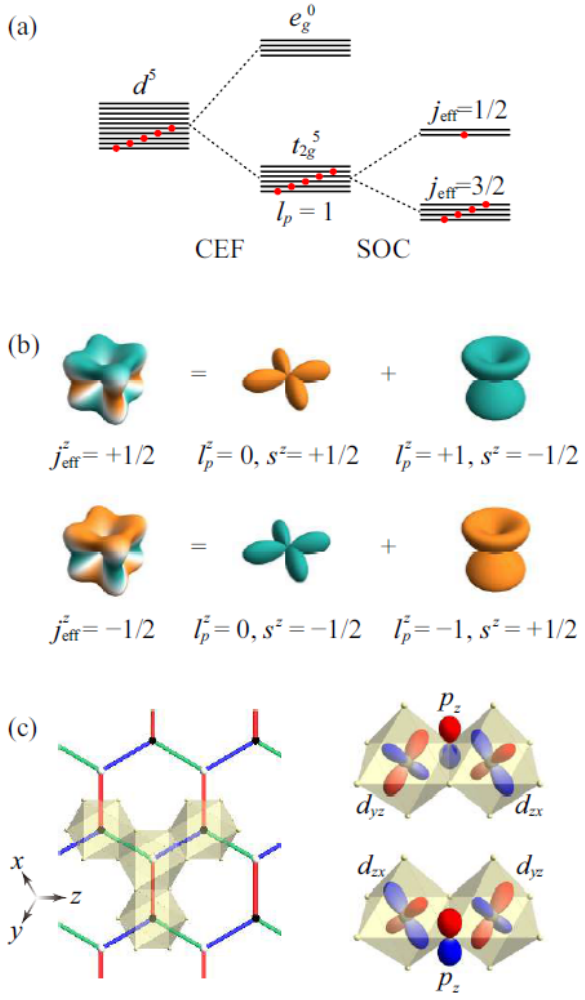


Figure 3.13: (a) the splitting of the energy levels of d-orbitals. (b) the schematic diagram of the wave function of the $j_{eff} = \pm 1/2$ state. (c) The honeycomb lattice structure consisting of MX_6 octahedra sharing an edge and the conceptual diagram of the d-p-d transition in the neighboring octahedra [61].

In this half-filling state, the perturbation of the electron hopping between M ions yields the effective exchange interaction acting on these pseudo-spins. This is similar to the fact that in the strongly correlated limit of the one-band Hubbard model, the second-order perturbation of the electron hopping gives a Heisenberg-type exchange interaction. The characteristic of this Mott insulator is the appearance of anisotropic exchange interactions, which depend on the spin component and the bond direction. This is due to the spatial anisotropy in 3.13. We consider that MX_6 octahedron in Fig.3.13 with shared edges. Considering the spatial anisotropic wave function of the t_{2g} orbitals, there are d-p-d orbitals processes via p-orbitals of the X ions as the electron hopping between neighboring M ions. This second perturbation gives the anisotropic exchange Ising type interactions due to the vanishing of the isotropic Heisenberg type interactions by the cancellation between the different perturbation processes. This cancellation is considered the quantum interference effect through orbital anisotropy.

$$\mathcal{H}_{ij}^{\gamma} = -KS_i^{\gamma}S_j^{\gamma} \tag{3.117}$$

This result means the realization of the Ising interaction with a Z-component. With the above idea, we can also describe the x and y components, and in the honeycomb systems with MX_6 octahedra sharing an edge, the Kitaev model is realized. This ion X is specifically Ir^{4+},Ru^{3+}, etc. The abode situation is idealized, and in actual materials, due to the natural transitions between d-orbitals and octahedral distortions, not only Kitaev interactions but also other types of interactions, called non-Kitaev interactions, appear. We introduce the derivation in detail below according to the theoretical proposal of [62].

As mentioned above, the effective Hamiltonian is given by the perturbation of the transition metal's overlap of the d-orbitals wave functions. Considering the case of the hole spin $\left|\tilde{\uparrow}\right\rangle$ $\left|\tilde{\downarrow}\right\rangle$ of the Eq. (3.115) at each transition metal site(see Fig.3.14), the perturbation calculation is performed using this basis. We define the t_{2g} electron operator.This operator means that the electrons are transferred to the d-orbitals.

$$d_1^{\dagger} = ({d_{1,yz}}^{\dagger}, {d_{1,zx}}^{\dagger}, {d_{1,xy}}^{\dagger}) \tag{3.118}$$

$$d_2^{\dagger} = ({d_{2,yz}}^{\dagger}, {d_{2,zx}}^{\dagger}, {d_{2,xy}}^{\dagger}) \tag{3.119}$$

Here, as a bond Hamiltonianm which is treated as a perturbation,

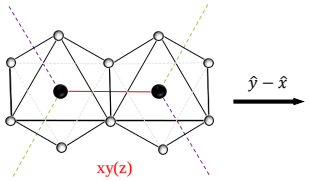


Figure 3.14: xy(z)bond [62].

$$V := T + T^{\dagger} := {d_1}^{\dagger} T_{12} d_2 + d_2^{\dagger} T_{21} d_1 \tag{3.120}$$

$$T_{12} = {T_{12}}^{\dagger} = T_{12}^{*} \tag{3.121}$$

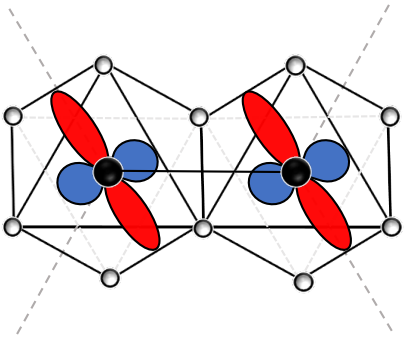
T_{12} is limited by the symmetry restriction of the ruthenium Ru and the oxygen O as follows.

$$T_{12} = \begin{pmatrix} t_1 & t_2 & 0 \\ t_2 & t_1 & 0 \\ 0 & 0 & t_3 \end{pmatrix} \tag{3.122}$$

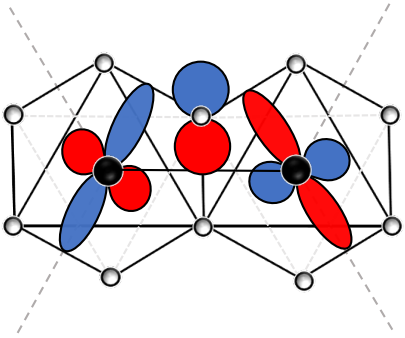
In addition, we add a term for trigonal distortion. For example, the hopping terms between xz-xy and yz-xy orbitals are as follows.

$$T_{12} = \begin{pmatrix} t_1 & t_2 & t_4 \\ t_2 & t_1 & t_4 \\ t_4 & t_4 & t_3 \end{pmatrix} \tag{3.123}$$

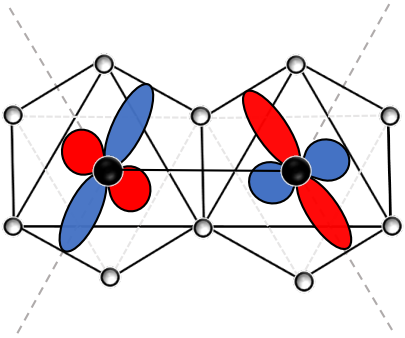
The t_i defined by the overlap integral of the wave function is represented in Fig.3.15.



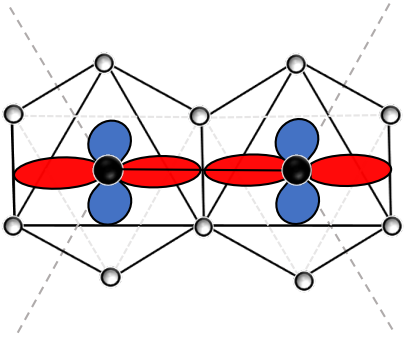
(a) Ir-Ir overlap for t_1



(b) Ir-O-Ir overlap for t_2



(c) Ir-Ir overlap for t_2



(d) Ir-Ir overlap for t_3

Figure 3.15: Schematic diagram of the types of contributions due to the overlap of the d-orbitals in the xy(x)bond [62]. (a) interference between d_{yz} orbitals. (b) interference between d_{zx} and d_{yz} orbitals via p_z orbitals of the oxygen. (c) interference effect that, unlike (b), does not involve oxygen. (d) interference effect between d_{xy} orbitals.

Here, we consider the case of $U, J_H \gg \lambda \gg t$ because it is a Mott insulator. We also use the two-atom Kanamori Hamiltonian as the non-perturbative Hamiltonian.

$$\begin{aligned} H_0 = H_1 + H_2 &= \frac{U - 3J_H}{2}[(N_1 - 5)^2 + (N_2 - 5)^2] - 2J_H({S_1}^2 + {S_2}^2) \\ &- \frac{J_H}{2}({L_1}^2 + {L_2}^2) \end{aligned} \tag{3.124}$$

For simplicity, we assume $d^5 \to d^1$, and the Hamiltonina is,

$$\begin{aligned} H_0 = H_1 + H_2 &= \frac{U - 3J_H}{2}[(N_1 - 1)^2 + (N_2 - 1)^2] - 2J_H({S_1}^2 + {S_2}^2) \\ &- \frac{J_H}{2}({L_1}^2 + {L_2}^2). \end{aligned} \tag{3.125}$$

In the following, we first derive one Γ term for the off-diagonal exchange interaction, one of the non-Kitaev interactions. We add perturbation $V = T + T^\dagger$ as the resultant orbital angular momentum $j_{eff} = \frac{1}{2}$. The perturbation energy is as follows,

$$\begin{aligned} E_{eff} &= \sum_{n \neq 0} \frac{\langle\alpha| T + T^\dagger |n\rangle \langle n| T + T^\dagger |\alpha\rangle}{E_0 - E_n} \\ &= -\sum_{n \neq 0} \frac{\langle\alpha| T |n\rangle \langle n| T^\dagger |\alpha\rangle}{E_n - E_0} + \frac{\langle\alpha| T^\dagger |n\rangle \langle n| T |\alpha\rangle}{E_n - E_0} \\ &= -\sum_{\beta} \sum_{n \neq 0} \left(\frac{\langle\alpha| T |n\rangle \langle n| T^\dagger |\beta\rangle}{E_n - E_0} + \frac{\langle\alpha| T^\dagger |n\rangle \langle n| T |\beta\rangle}{E_n - E_0} \right) \langle\beta|\alpha\rangle . \end{aligned} \tag{3.126}$$

α,β are $j_{eff} = \frac{1}{2}$, and the ground states,$\left|\frac{1}{2}, \frac{1}{2}\right\rangle$ $\left|\frac{1}{2}, -\frac{1}{2}\right\rangle$ $\left|-\frac{1}{2}, \frac{1}{2}\right\rangle$ $\left|-\frac{1}{2}, -\frac{1}{2}\right\rangle$ are four degenerate. Here we express $|j_{eff,1}, j_{eff,2}\rangle$. Thus, the effective Hamiltonian is,

$$H_{eff} = -\sum_{\alpha\beta} \sum_{n \neq 0} \left(\frac{\langle\alpha| T |n\rangle \langle n| T^\dagger |\beta\rangle}{E_n - E_0} + \frac{\langle\alpha| T^\dagger |n\rangle \langle n| T |\beta\rangle}{E_n - E_0} \right) |\alpha\rangle \langle\beta| . \tag{3.127}$$

The elements are written down in concrete terms.

$$
\begin{aligned}
V &:= T = T_1 + T_2 && (3.128)\\
T_1 &= \sum_{\sigma} t_1[(d_1^{\dagger})_{xz\sigma}(d_2)_{xz\sigma} + (d_1^{\dagger})_{yz\sigma}(d_2)_{yz\sigma})] + t_3(d_1^{\dagger})_{xy\sigma}(d_2)_{xy\sigma}\\
T_2 &= \sum_{\sigma} t_2[(d_1^{\dagger})_{xz\sigma}(d_2)_{yz\sigma} + (d_1^{\dagger})_{yz\sigma}(d_2)_{xz\sigma})] + t_4[(d_1^{\dagger})_{yz\sigma}(d_2)_{xy\sigma}\\
&+ (d_1^{\dagger})_{zx\sigma}(d_2)_{xy\sigma} + (d_1^{\dagger})_{xy\sigma}(d_2)_{yz\sigma} + (d_1^{\dagger})_{xy\sigma}(d_2)_{zx\sigma}] && (3.129)
\end{aligned}
$$

In the following, the Γ term is derived. Thus we assume $t_4 = 0$. Denoting the ground states as $\alpha = 1, 2$ as the number of sites(the sign is different from the definition of (3.115)) [62].

$$
\begin{aligned}
\left|+\frac{1}{2}\right\rangle_{\alpha} &= \frac{1}{\sqrt{3}}\left[|xy\rangle_1 |\uparrow\rangle_1 + (i|xz\rangle_1 + |yz\rangle_1)|\downarrow\rangle_1\right] && (3.130)\\
&= \sqrt{\frac{1}{3}}\left(d^{\dagger}_{a,yz,\downarrow} + id^{\dagger}_{a,xz,\downarrow} + d^{\dagger}_{a,xy,\uparrow}\right)|0\rangle_a\\
&= \left[\sqrt{\frac{2}{3}}d^{\dagger}_{a,+\downarrow} - i\sqrt{\frac{1}{3}}d^{\dagger}_{a,0,\uparrow}\right]|0\rangle_a && (3.131)
\end{aligned}
$$

$$
\begin{aligned}
\left|-\frac{1}{2}\right\rangle_{\alpha} &= \frac{1}{\sqrt{3}}\left[|xy\rangle_1 |\downarrow\rangle_1 + (i|xz\rangle_1 - |yz\rangle_1)|\uparrow\rangle_1\right] && (3.132)\\
&= \sqrt{\frac{1}{3}}\left(d^{\dagger}_{a,yz,\uparrow} - id^{\dagger}_{a,xz,\uparrow} - d^{\dagger}_{a,xy,\downarrow}\right)^{\dagger}|0\rangle_a\\
&= -\left[\sqrt{\frac{2}{3}}d^{\dagger}_{a,-\uparrow} + i\sqrt{\frac{1}{3}}d^{\dagger}_{a,0,\downarrow}\right]|0\rangle_a && (3.133)
\end{aligned}
$$

The resultant orbital angular momentum l_{eff} is defined only for t_2g orbits in 5d-orbits, and the equation in the third line of each basis uses the following.

$$
\begin{aligned}
d^{\dagger}_{a,+,\sigma} &= \sqrt{\frac{1}{2}}\left(d^{\dagger}_{a,yz,\sigma} + id^{\dagger}_{a,xz,\sigma}\right) && (3.134)\\
d^{\dagger}_{a,0,\sigma} &= id^{\dagger}_{a,xy,\sigma} && (3.135)\\
d^{\dagger}_{a,-,\sigma} &= \sqrt{\frac{1}{2}}\left(d^{\dagger}_{a,yz,\sigma} - id^{\dagger}_{a,xz,\sigma}\right) && (3.136)
\end{aligned}
$$

The ground state of the non-perturbative Hamiltonian are ${}^2P$ and six degenerate states($L=1, S=\frac{1}{2}$), with electron number $N=1$ and energy $E_0=-\frac{5}{2}J_H$. However, $N_2=0, N_1=2$ states need to be considered, since T causes electrons to move to neighboring sites. The states taken in each case are determined by the angular momentum coupling.

$$
\begin{aligned}
N &= 0 \to S=0, L=0 \to {}^1S && (3.137)\\
N &= 2 \to l_1=1 s_1=\frac{1}{2}, l_2=1, s_2=\frac{1}{2} \to {}^1S, {}^3P, {}^1D && (3.138)
\end{aligned}
$$

Thus, the transition energy into the intermediate state is,

$$
\begin{aligned}
E_2({}^1S)+E_0({}^1S)-2E_1\left({}^2P\right) &= U+2J_H, && (3.139)\\
E_2\left({}^3P\right)+E_0\left({}^1S\right)-2E_1\left({}^2P\right) &= U-3J_H, && (3.140)\\
E_2\left({}^1D\right)+E_0\left({}^1S\right)-2E_1\left({}^2P\right) &= U-J_H. && (3.141)
\end{aligned}
$$

The matrix element is,

$$
\begin{aligned}
T_1\left|+\frac{1}{2}\right\rangle_1\left|+\frac{1}{2}\right\rangle_2 &= \left(\frac{t_1-t_3}{3}\right)\left(d^\dagger_{1,yz,\downarrow}+id^\dagger_{1,xz,\downarrow}\right)d^\dagger_{1,xy,\uparrow}|0\rangle_1|0\rangle_2,\\
&= -i\left(\frac{t_1-t_3}{3}\right)[|+\downarrow,0\uparrow\rangle_1-|0\uparrow,+\downarrow\rangle_1]|0\rangle_2,\\
&= -i\left(\frac{t_1-t_3}{3}\right)\left[\left|{}^3P,+1,0\right\rangle_1-\left|{}^1D,+1,0\right\rangle_1\right]|0\rangle_2, && (3.142)\\
T_2\left|+\frac{1}{2}\right\rangle_1\left|+\frac{1}{2}\right\rangle_2 &= \frac{t_2}{3}\left[2d^\dagger_{1,xz,\downarrow}d^\dagger_{2,yz,\downarrow}+i\left(d^\dagger_{1,yz,\downarrow}\right)d^\dagger_{1,xy,\uparrow}\right]|0\rangle_1|0\rangle_2,\\
&= \frac{t_2}{3}[-2i(|+\downarrow,-\downarrow\rangle-|-\downarrow,+\downarrow\rangle)+(|-\downarrow,0\uparrow\rangle-|0,\uparrow,-\downarrow\rangle)]|0\rangle_2,\\
&= \frac{t_2}{3}\left[-2\sqrt{2}i\left|{}^3P,0,-1\right\rangle_1-\left|{}^3P,-1,0\right\rangle_1-\left|{}^1D,-1,0\right\rangle_1\right]|0\rangle_2. && (3.143)
\end{aligned}
$$

The multiplet is determined by the fermion parity of the wave function and is denoted as $\left|{}^{2S+1}L,M_L,M_S\right\rangle_a$,$(a=1,2)$. As an example, we show the matrix elements that transition from the ground state.

$$
\begin{aligned}
& \left|^3P,+1,0\right\rangle_1 - \left|^1D,+1,0\right\rangle_1 \\
= \;& |L=1,Lz=1\rangle_1 \frac{1}{\sqrt{2}}(|\uparrow\downarrow\rangle_1 + |\downarrow\uparrow\rangle_1) - |L=2,Lz=1\rangle_1 \frac{1}{\sqrt{2}}(|\uparrow\downarrow\rangle_1 - |\downarrow\uparrow\rangle_1) \\
= \;& \frac{1}{\sqrt{2}}(-|l=1,lz=0\rangle_1 |1,1\rangle_1 + |1,1\rangle_1 |1,0\rangle_1)\frac{1}{\sqrt{2}}(|\uparrow\downarrow\rangle_1 + |\downarrow\uparrow\rangle_1) \\
- \;& \frac{1}{\sqrt{2}}(|1,0\rangle_1 |1,1\rangle_1 + |1,1\rangle_1 |1,0\rangle_1)\frac{1}{\sqrt{2}}(|\uparrow\downarrow\rangle_1 - |\downarrow\uparrow\rangle_1) \\
= \;& -|0\uparrow,+\downarrow\rangle_1 + |+\downarrow,0\uparrow\rangle_1
\end{aligned} \tag{3.144}
$$

The $\left|^{2S+1}L,M_L,M_S\right\rangle$ state is defined under time-reversal symmetry with sign $(-1)^{L+S+M_L+M_S}$. Using a similar approach, the matrix elements in another basis are obtained as follows.

$$
T_1 \left|-\frac{1}{2}\right\rangle_1 \left|-\frac{1}{2}\right\rangle_2 = i\left(\frac{t_1-t_3}{3}\right)\left[\left|^3P,-1,0\right\rangle_1 - \left|^1D,-1,0\right\rangle_1\right]|0\rangle_2 \tag{3.145}
$$

$$
T_2 \left|-\frac{1}{2}\right\rangle_1 \left|-\frac{1}{2}\right\rangle_2 = -\frac{t_2}{3}\left[-2\sqrt{2}i\left|^3P,0,+1\right\rangle_1 + \left|^3P,+1,0\right\rangle_1 + \left|^1D,+1,0\right\rangle_1\right]|0\rangle_2 \tag{3.146}
$$

Here, the coefficient of the off-diagonal exchange interaction Γ term is defined [62],

$$
\Gamma := 2i\left\langle -\frac{1}{2},-\frac{1}{2}\right| \mathbf{H_{eff}} \left|\frac{+\mathbf{1}}{\mathbf{2}},\frac{+\mathbf{1}}{\mathbf{2}}\right\rangle, \tag{3.147}
$$

$$
\begin{aligned}
&= 2i\big[-4i * \frac{t_2(t_1-t_3)}{9}\big[\frac{1}{U-3J_H} - \frac{1}{U-J_H}\big]\big] \\
&= \frac{16J_H}{9}\big[\frac{t_2\,(t_1-t_3)}{(U-3J_H)(U-J_H)}\big]
\end{aligned} \tag{3.148}
$$

The diagonal terms are obtained similarly. Finally, the effective Hamiltonian is,

$$
\begin{aligned}
H_{\text{eff}} \;\sim\;& K S_1^z S_2^z + J\vec{S}_1\cdot\vec{S}_2 + \Gamma\left(S_1^x S_2^y + S_1^y S_2^x\right) \\
+\;& \Gamma'\left(S_1^x S_2^z + S_1^z S_2^x + S_1^y S_2^z + S_1^z S_2^y\right)
\end{aligned} \tag{3.149}
$$

The first term is the Kitaev Hamiltonian, and the second and subsequent terms are called the non-Kitaev interactions. The second term is the Heisenberg interaction, and the third and fourth are called non-diagonal exchange interactions. By recomputing the band Hamiltonian with $t_4 \neq 0$, we can also derive the Γ' term for the non-diagonal exchange interaction[62].

$$\Gamma = \frac{8J_H}{9}\left[\frac{3t_4^2 + 2t_2\left(t_1 - t_3\right)}{\left(U - 3J_H\right)\left(U - J_H\right)}\right] \tag{3.150}$$

$$\Gamma' = -\frac{8J_H}{9}\left[\frac{t_4\left(t_1 - t_3 - 3t_2\right)}{\left(U - 3J_H\right)\left(U - J_H\right)}\right] \tag{3.151}$$

There are also studies that specifically obtained these parameters by ab initio calculations [58], which are referred to in Table 3.16.

	$d_{\mathrm{Ru-Cl}}^{\mathrm{avg}}$ (Å)	$d_{\mathrm{Ru-Ru}}$	t_1	t_2	t_3 (eV)	t_4	J	K	Γ (meV)	Γ'
Case 0 structure: old $P3_112$ structure (from Ref. [3], $a = a_0$, $b = b_0$)										
NN	2.45	3.44	+0.066	+0.114	−0.229	−0.010	−3.50	+4.60	+6.42	−0.04
Case I structure: $a = 0.981a_0$, $b = 0.986b_0$ (structure optimized with SOC)										
NN-Z	2.34	3.40	+0.058	+0.177	−0.154	−0.022	−2.67	−4.52	+7.27	−0.67
NN-X/Y		3.38	+0.060	+0.165	−0.160	−0.018	−2.81	−3.07	+6.99	−0.47
Case II structure: $a = a_0$, $b = b_0$ (structure optimized with SOC and lattice constants fixed)										
NN-Z	2.36	3.44	+0.044	+0.178	−0.109	−0.019	−1.49	−6.71	+5.28	−0.69
NN-X/Y		3.44	+0.042	+0.176	−0.107	−0.030	−1.55	−6.47	+5.24	−1.08
Case III structure: $a = 1.011a_0$, $b = 1.006b_0$ (structure optimized with SOC, U_{eff}, and zigzag order)										
NN-Z	2.36	3.47	+0.036	+0.191	−0.062	−0.024	−0.74	−9.34	+3.71	−1.04
NN-X/Y		3.47	+0.037	+0.182	−0.075	−0.026	−1.09	−7.64	+4.38	−0.87

Figure 3.16: Parameters [58] of α-$RuCl_3$. There is the case that the lattice lengths are changed. It is noteworthy that the Kitaev interaction K, the Heisenberg interaction J, and the off-diagonal exchange interaction Γ are comparable in size, while the off-diagonal exchange interaction Γ' is smaller by a tenth order of magnitude.

Chapter 4

Non-Kitaev interaction

Here we briefly describe effects of non-Kitaev interactions on the itinerant Majorana fermions in the Kitaev spin liquid[45, 52, 53]. We have derived the effective Hamiltonian terms, taking the non-Kitaev terms and the magnetic field as the perturbation terms. As a result, we have acquired two kinds of many-Majorana interactions. One is the two-Majorana interactions that enhance the Majorana gap in the chiral spin liquid [52] or change the Majorana spectral and the number of the Dirac points [53]. We argue that the former can explain the Quantum thermal Hall effect experiments. The latter can induce the topological phase transition by changing the Chern number from ± 1 to ± 2. The other is four-Majorana interactions which trigger a nematic phase transition of Majorana bonds, changing the Chern number from ± 1 to zero. This phase is the toric code A-phase, and we argue that this explains the topological nematic transition observed in the heat capacity measurements of α-$RuCl_3$ [63].

First, we show the details of the perturbation calculation induced by non-Kitaev interactions. In this calculation, we need to evaluate the matrix elements of the perturbation terms for the eigenstates of Z_2 vortices. First, we show the kinds of the two-Majorana interactions about the $\Gamma^{'}$ term and the magnetic field. As a result, we found that the $\Gamma^{'}$ term works on the Majorana fermions in the Kitaev spin liquid as like the magnetic field. Next, we show the four-Majorana interactions about the Y-shaped interaction induced by Γ' term, second, the Zigzag-shaped interaction and Armchair-shaped interaction caused by Γ term and Heisenberg term.

We start with the following Hamiltonian for candidate materials of the

Kitaev magnet on a honeycomb lattice such as α-$RuCl_3$ and Na_2IrO_3,

$$\mathcal{H}_{J_H} = J_H \sum_{\langle ij \rangle} \boldsymbol{S}_i \cdot \boldsymbol{S}_j, \tag{4.1}$$

$$\mathcal{H}_J = -J \sum_{\langle ij \rangle_\alpha} S_i^\alpha S_j^\alpha, \tag{4.2}$$

$$\mathcal{H}_\Gamma = \Gamma \sum_{\substack{\langle ij \rangle_\alpha \\ \beta,\gamma \neq \alpha}} [S_i^\beta S_j^\gamma + S_i^\gamma S_j^\beta], \tag{4.3}$$

$$\mathcal{H}_{\Gamma'} = \Gamma' \sum_{\substack{\langle ij \rangle_\alpha \\ \beta \neq \alpha}} [S_i^\alpha S_j^\beta + S_i^\beta S_j^\alpha], \tag{4.4}$$

where S_i^α is an $\alpha = x, y, z$ component of an $s = 1/2$ spin operator at a site i. $\mathcal{H}_{J_H}$ is the Heisenberg exchange interaction between the nearest neighbor sites, and $\mathcal{H}_J$ is the Kitaev interaction. Here, $\langle ij \rangle_\alpha$ denotes that the i-site and the j-site are the nearest-neighbor sites connected via an α-bond on the honeycomb lattice.

We derive the perturbation term using the same method as Kitaev's paper[4], putting $V' = \mathcal{H}_{zeem} + \mathcal{H}_\Gamma + \mathcal{H}_{\Gamma'} + \mathcal{H}_{J_H}$, where $\mathcal{H}_{\Gamma'}$ is the non-Kitaev interaction term in which all terms $\Gamma' S_i^\alpha S_j^\beta$ acting on $\langle ij \rangle_\alpha$ sites are eliminated, we carry out the perturbative calculation for V'.

First, we describe the two-Majorana interaction of the second-order perturbation term. We consider the process as like Fig.4.1. (a) is the vortex-free initial state. (b) is the intermediate state which $\Gamma' \sigma_2^y \sigma_4^x$ acts on the vortex-free initial state. (c) is the final state in the vortex-free state which $h^z \sigma_1^z$ acts on the intermediate state.

As a result, the second-order perturbation term is,

$$H_{\Gamma'} = -\frac{i\Gamma'}{4|J|} \sum_{\substack{\mathbf{m=0,1} \\ \mathbf{p=1,2,3}}} \sum_{\substack{\langle \mathbf{i,j} \rangle_\alpha \\ \langle \mathbf{j,k} \rangle_\beta \\ \mathbf{i=k+n_p}}} (h_i^\alpha + h_k^\beta)(-1)^m c_i c_k. \tag{4.5}$$

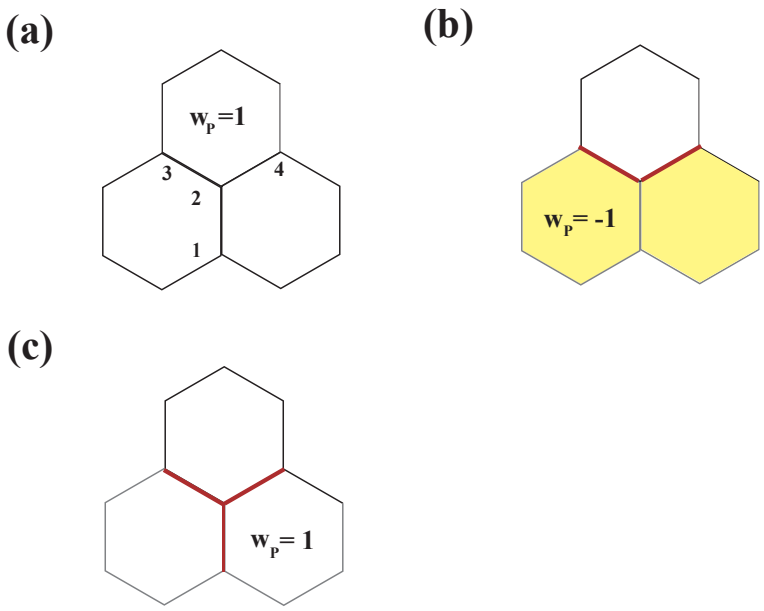


Figure 4.1:

This effective Hamiltonian is a next-nearest-neighbor hopping term. The $\mathbf{n}_p$ is the direction of the hopping Eq. (3.50)-Eq. (3.52) and m=0 if the site i is on the even site(white site) of the honeycomb lattice, and m=1 if i is on the odd site(black site).

$$\Delta(\boldsymbol{k}) = \Delta_0(\boldsymbol{k}) + \Delta_1(\boldsymbol{k}), \tag{4.6}$$

$$\Delta_0(\boldsymbol{k}) = \frac{4h^x h^y h^z}{K^2}[\sin(\boldsymbol{k}\cdot\boldsymbol{n}_1) + \sin(\boldsymbol{k}\cdot\boldsymbol{n}_2) + \sin(\boldsymbol{k}\cdot\boldsymbol{n}_3)], \tag{4.7}$$

$$\begin{aligned}\Delta_1(\boldsymbol{k}) = & -\frac{\Gamma'}{|K|}[(h^x + h^z)\sin(\boldsymbol{k}\cdot\boldsymbol{n}_1) \\ & +(h^y + h^z)\sin(\boldsymbol{k}\cdot\boldsymbol{n}_2) + (h^x + h^y)\sin(\boldsymbol{k}\cdot\boldsymbol{n}_3)].\end{aligned} \tag{4.8}$$

When the off-diagonal exchange is negative, the absolute value of the Majorana gap is enhanced. According to the parameter of the α-$RuCl_3$ in Fig.3.16, this effect exists and helps to understand the stability of the quantum thermal Hall effect [1].

Next, we examine nonzero matrix elements of the second-order perturbation terms about the $\Gamma^{'}$ term. To be concrete, we here focus on the two

cases of the hopping term. One is the case of Fig.4.2. (a) is the vortex-free initial state, and (b) is the intermediate state which the $\Gamma^{'}$ term $\Gamma^{'}\sigma_1^x\sigma_2^y$ acts on the vortex-free initial state. (c) is the final state which the $\Gamma^{'}$ term $\Gamma^{'}\sigma_4^x\sigma_3^y$ acts. Similarly, we can show that all the hopping processes $\mathbf{N}_1$ -$\mathbf{N}_6$ shown in Fig.4.4 by the second-order perturbations.

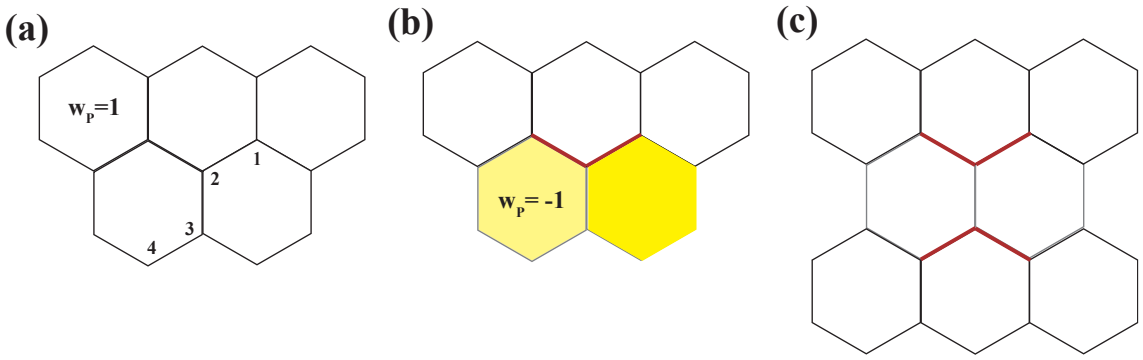


Figure 4.2:

The other is the case of Fig.4.3. (a) is the vortex-free initial state, and (b) is the intermediate state which the $\Gamma^{'}$ term $\Gamma^{'}\sigma_1^y\sigma_2^z$ acts on the vortex-free initial state. (c) is the final state which the $\Gamma^{'}$ term $\Gamma^{'}\sigma_3^y\sigma_4^z$ acts. Similarly, we can show that all the hopping processes $\mathbf{N}_7$ -$\mathbf{N}_9$ shown in Fig.4.4. by the second-order perturbations.

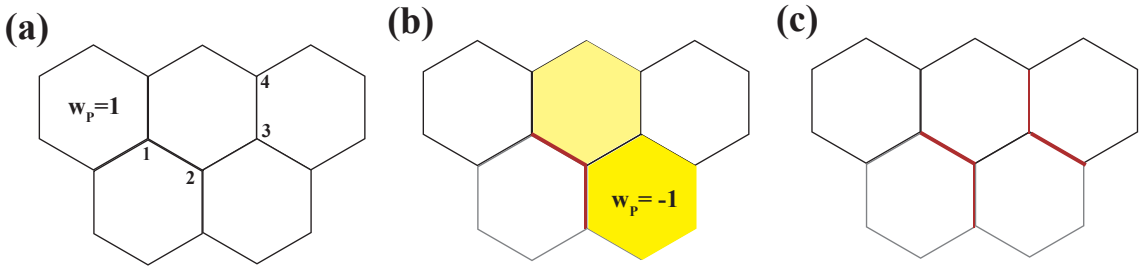


Figure 4.3:

As a result, the perturbation terms generate the third nearest-neighbor hopping terms $\mathbf{N}_1$ -$\mathbf{N}_6$ shown in Fig.4.4.

$$\mathcal{H}^{(2)}_{eff} = -\frac{i\Gamma'^2}{16|K|}\sum_{\mathbf{i}}\Bigg[\sum_{\substack{\mathbf{P=1::6}\\ \mathbf{m=0,1}}}(-1)^m c_{(i+N_P(-1)^{m-1})}c_i + 2\sum_{\substack{\mathbf{P=7,8,9}\\ \mathbf{m=0,1}}}(-1)^{m-1}c_{(i+N_P(-1)^{m-1})}c_i\Bigg] \tag{4.9}$$

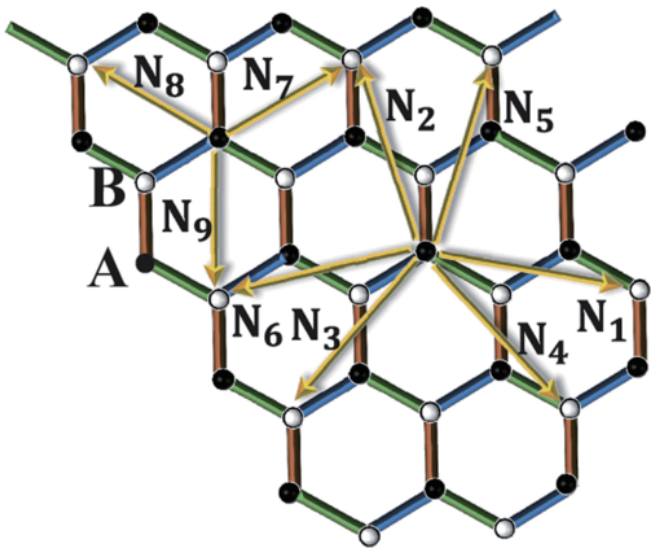


Figure 4.4: [52]

These terms changes the Eq. (3.49) to,

$$f(q) = \frac{\Gamma'^2}{4|K|}\sum_{\mathbf{P=1:6}} e^{-i\vec{q}\cdot\vec{N_P}} - \frac{\Gamma'^2}{2|K|}\sum_{\mathbf{P=7,8,9}} e^{-i\vec{q}\cdot\vec{N_P}} + \frac{K}{2}\left[1 + e^{i\vec{q}\cdot\vec{n_1}} + e^{-i\vec{q}\cdot\vec{n_2}}\right], \tag{4.10}$$

Due to changing the number of the Dirac points, the topological phase transition is induced, shown by the Chern number phase diagram in Fig.4.5. The phase with the Chern number equal to ± 2 is the Abelian topological phase and can be detected by the measurement of the quantized thermal Hall conductivity.

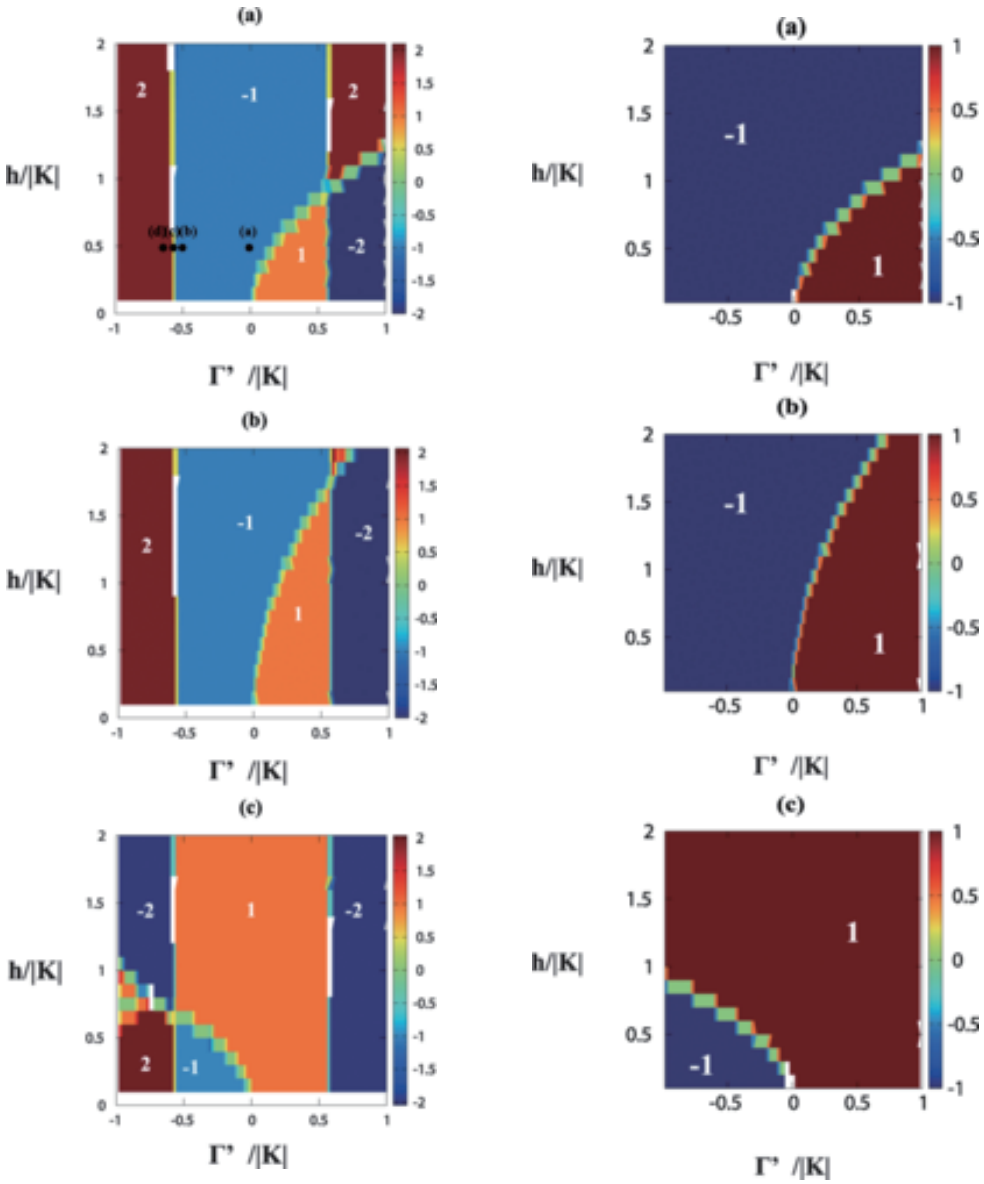


Figure 4.5: [52]

Finally, we derive the four-Majorana interaction. First, we consider the Y-shaped interaction, the third-order perturbation term from Γ'term. To be concrete, we show an example of the perturbation processes in FIG.4.6. In this example of the third order perturbations in Γ', the operations of $\Gamma'\sigma_1^z\sigma_2^x$ and $\Gamma'\sigma_2^x\sigma_3^y$ and $h_x\sigma_4^x$ on the vortex-free ground state generate the final state, the vortex-free ground state. The third-order perturbation is given by,

$$\begin{aligned}\mathcal{H}^{(3)}_{Y-shaped} &= \Pi_0 V' G'_0(E) V' G'_0(E) V' \Pi_0, \\ &= \frac{\Gamma'^2}{32|J|^2} \sum_{\substack{\alpha=x,y,z \\ \beta\neq\alpha \\ \gamma\neq\beta,\alpha}} \sum_{\substack{\langle ij\rangle_\alpha \\ \langle jl\rangle_\gamma \\ \langle jk\rangle_\beta}} \Pi_0 \sigma_i^\alpha \sigma_l^\gamma \sigma_k^\beta (h_\beta + h_\gamma) \Pi_0, \end{aligned} \tag{4.11}$$

where $\alpha, \beta, \gamma = x, y, z$, Π_0 is a projection to the vortex-free spin liquid state. To analyze this term more precisely, we use the fact that in the Majorana fermion representation of the Kitaev spin liquid state, gauge Majorana fields b_i^α should be paired on the α-bond connecting two sites i and j to form Z_2 gauge fields $\hat{u}_{ij}^\alpha = \mathrm{i} b_i^\alpha b_j^\alpha$, since the Kitaev spin liquid state is expressed by the eigen state of the Z_2 gauge fields. Then in the case of $\alpha = x$, eq.(4.11) is recast into,

$$\mathcal{H}^{(3)}_{Y-shaped} = \Pi_0 \left[\sum_{\substack{\langle ij\rangle_x \\ \langle jl\rangle_y \\ \langle jk\rangle_z}} (-\tfrac{\Gamma'^2(h_y+h_z)}{32\Delta_Y\Delta_Z}) [c_i c_l c_k c_j \hat{u}_{ij}^x \hat{u}_{lj}^y \hat{u}_{kj}^z \right] \Pi_0,$$

where Δ_y, Δ_z are the energy gap of the excited state. This shows the Y-shaped interaction of the four-Majorana interaction in the site $\langle ijkl\rangle$ in FIG.4.6(e).

Second, we consider the armchair-shaped interaction, which is the third order perturbation term from Γ term with the same method as the Y-shaped interaction. To be concrete, we show an example of the perturbation processes in FIG.4.7. In this example of the third order perturbations in Γ, the operations of $\Gamma\sigma_1^x\sigma_2^y$ and $h_y\sigma_3^y$ and $h_x\sigma_4^x$ on the vortex-free ground state generate the final state, the vortex-free ground state. Thus, these perturbation processes are allowed within the ground state sector. The third order

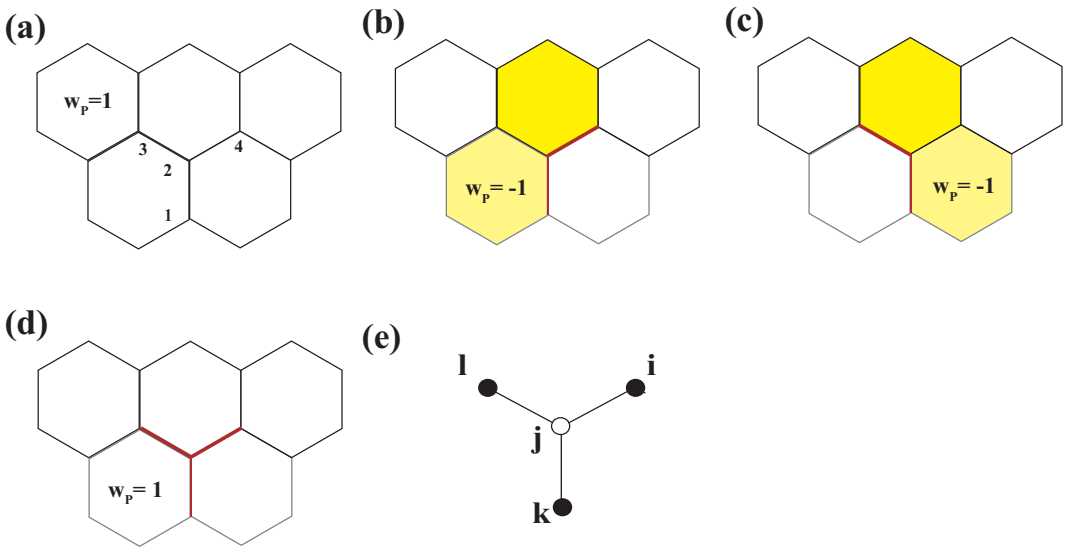


Figure 4.6: The operation of $\Gamma'\sigma_2^x\sigma_1^z$ on the vortex-free ground state(shown in (a))flips the Z_2 gauge fields on the bonds denoted by red color shown in (b), and generates two visons (yellow hexagons). The operation of $\Gamma'\sigma_2^x\sigma_3^y$ on the state shown in (b) results in the excited state with two visons as shown in (c). The operation of $h_x\sigma_4^x$ on the state shown in(c) results in the ground state, the vortex-free state(d).[45]

perturbation is given by,

$$\begin{aligned}\mathcal{H}^{(3)}_{Arm-shaped} &= \Pi_0 V' G_0'(E) V' G_0'(E) V' \Pi_0, \\ &= \frac{\Gamma}{16|J|^2} \sum_{\substack{\alpha=x,y,z \\ \beta\neq\alpha \\ \gamma\neq\beta,\alpha}} \sum_{\substack{\langle kl\rangle_\alpha \\ \langle jk\rangle_\beta \\ \langle jl\rangle_\gamma}} \Pi_0 h_\beta h_\gamma \sigma_i^\beta \sigma_j^\gamma \sigma_k^\beta \sigma_l^\gamma \Pi_0, \end{aligned} \tag{4.12}$$

Then eq.(4.12) is recast into,

$$\mathcal{H}^{(3)}_{Arm-shaped} = \Pi_0 \left[\sum_{\substack{\langle kl\rangle_\alpha \\ \langle ik\rangle_\beta \\ \langle jl\rangle_\gamma}} (-\tfrac{\Gamma h_\beta h_\gamma}{16\Delta_W \Delta_{W'}}) [c_i c_k c_l c_j \hat{u}^\beta_{ik} \hat{u}^\gamma_{lj}] \right] \Pi_0,$$

where $\Delta_W, \Delta_{W'}$ are the energy gap of the excited state. This shows the armchair-shaped interaction of the four-Majorana interaction in the site $\langle ijkl\rangle$ in FIG.4.8(e).

Finally, we consider the zigzag-shaped interaction, which is the third order perturbation term from Heisenberg term with the same method as the Y-shaped interaction. To be concrete, we show an example of the perturbation processes in FIG.4.8. In this example of the third order perturbations in J_H, the operations of $J_H \sigma_1^x \sigma_2^x$ and $h_x \sigma_3^x$ and $h_x \sigma_4^x$ on the vortex-free ground state generate the final state, the vortex-free ground state. Thus, these perturbation processes are allowed within the ground state sector. The third order perturbation is given by,

$$\begin{aligned}\mathcal{H}^{(3)}_{Zigzag-shaped} &= \Pi_0 V' G_0'(E) V' G_0'(E) V' \Pi_0, \\ &= \frac{\Gamma}{16|J|^2} \sum_{\substack{\alpha=x,y,z \\ \beta\neq\alpha}} \sum_{\substack{\langle ij\rangle_\alpha \\ \langle ik\rangle_\beta \\ \langle lj\rangle_\beta}} \Pi_0 {h_\beta}^2 \sigma_k^\beta J_H \sigma_i^\beta \sigma_j^\beta \sigma_l^\beta \Pi_0, \end{aligned} \tag{4.13}$$

Then eq.(4.13) is recast into,

$$\mathcal{H}^{(3)}_{Zig-shaped} = \Pi_0 \left[\sum_{\substack{\langle ij\rangle_\alpha \\ \langle ik\rangle_\beta \\ \langle jl\rangle_\beta}} (-\tfrac{J_H {h_\beta}^2}{16\Delta_\chi \Delta_{\chi'}}) [c_k c_i c_j c_l \hat{u}^\beta_{ki} \hat{u}^\beta_{jl}] \right] \Pi_0,$$

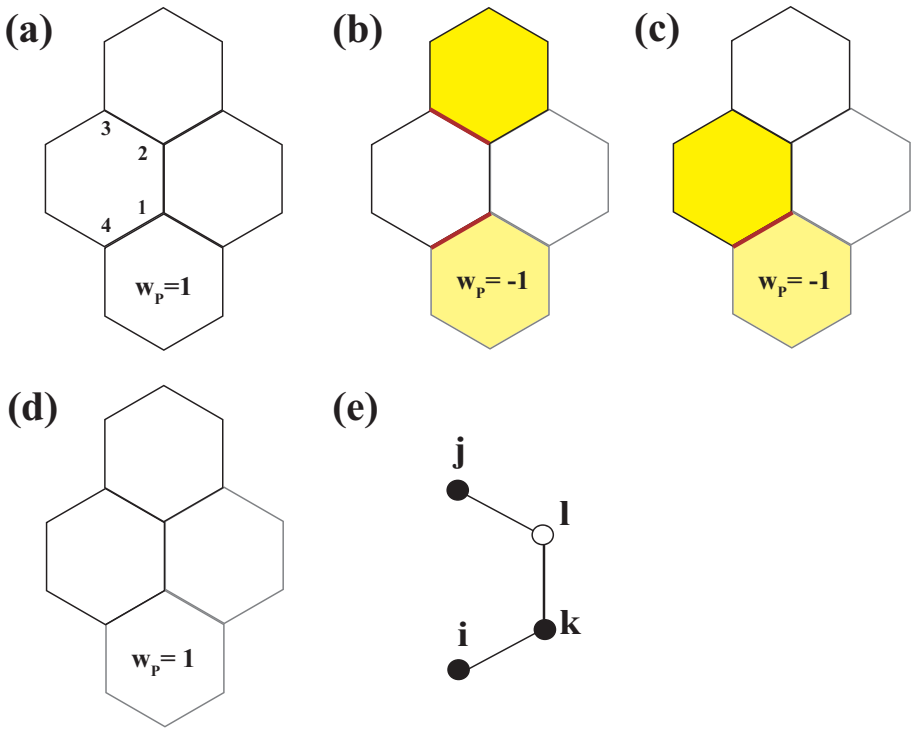


Figure 4.7: The operation of $\Gamma\sigma_1^x\sigma_2^y$ on the vortex-free ground state (shown in (a)) flips the Z_2 gauge fields on the bonds denoted by red color shown in (b), and generates two visons. The operation of $h_y\sigma_3^y$ on the state shown in (b) results in the excited state with two visons as shown in (c). The operation of $h_x\sigma_4^x$ on the state shown in(c) results in the ground state, the vortex-free state(d). [45]

where $\Delta_\chi, \Delta_{\chi'}$ are the energy gap of the excited state. This shows the zigzag-shaped interaction of the four-Majorana interaction in the site $\langle ijkl \rangle$ in FIG.4.8(e).

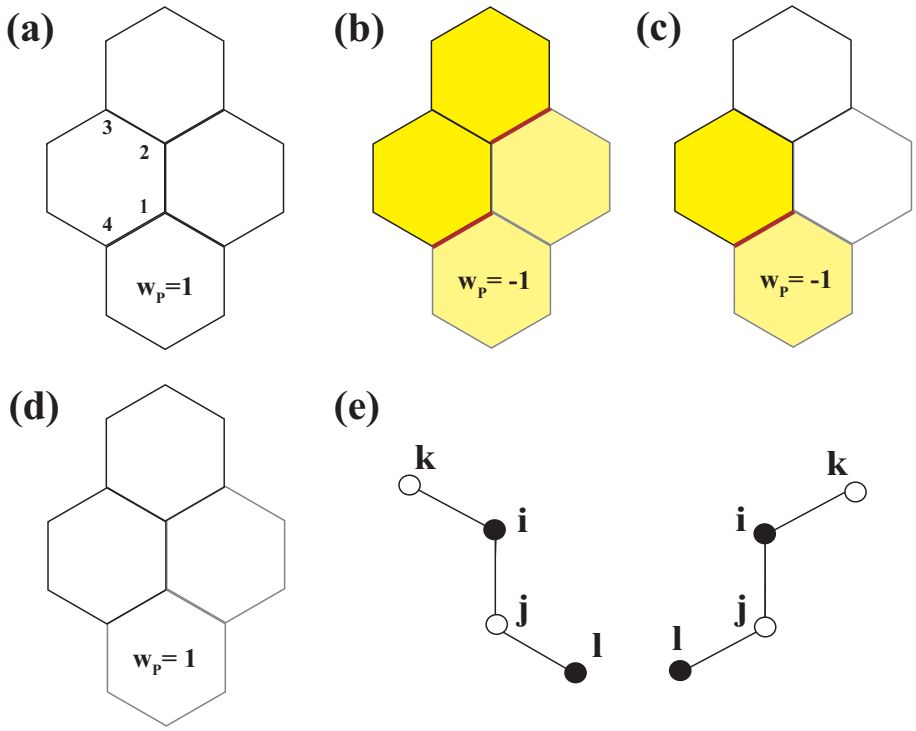


Figure 4.8: The operation of $J_H \sigma_1^x \sigma_2^x$ on the vortex-free ground state (shown in (a)) flips the Z_2 gauge fields on the bonds denoted by red color shown in (b), and generates four visons. The operation of $h_x \sigma_3^x$ on the state shown in (b) results in the excited state with two visons as shown in (c). The operation of $h_x \sigma_4^x$ on the state shown in(c) results in the ground state, the vortex-free state(d).[45]

Non-Kitaev interactions, such as off-diagonal exchange interactions, generate these four-Majorana interactions Eq. (4.13),Eq. (4.11),Eq. (4.12) and give rise to the topological nematic phase transition from the chiral spin liquid to the toric code A-phase [45].

Chapter 5

Experimental studies on α-$RuCl_3$

As shown in the previous chapter, G. Jackeli and G. Khaliulin proposed real candidates for Kitaev materials. In this chapter, we review previous experimental studies on real candidates for Kitaev materials, focusing on α-$RuCl_3$, which is the most promising material for the Kitaev spin liquid. This section will focus on experiments that are probable to become evidence of the Majorana fermions in α-$RuCl_3$.

5.1 Quantum thermal Hall effect

The Kitaev spin liquid may be potentially realized in 2D honeycomb materials such as α-$RuCl_3$ [4, 10, 11, 12, 13, 14, 15, 16, 17, 18, 19, 20, 21, 22, 23, 24, 25, 26, 27, 28, 29, 30, 31, 32, 33, 34, 35, 36, 37, 38, 39, 40, 41, 42, 43, 44, 45]. The observation of the half-quantized thermal Hall effect for α-$RuCl_3$, which is a signature of chiral Majorana fermions, has been reported [1].

The topological phase in the two-dimensional thermal Hall effect is characterized by the topological invariant[1]. The thermal Hall conductivity is quantized as $\frac{\kappa_{xy}^{2D}}{T} = \frac{\pi}{12}\frac{k_B^2}{\hbar}$. They report the results as a powerful manifestation of Majorana particles. The Kitaev interaction is $J_K/k_B \approx 80$K. According to Fig.5.1(c), the topological phase is the red region, and the plateau behavior of $\frac{\kappa_{xy}^{2D}}{T}$ can be seen in the field range of 4.5T $<\mu_0 H_\perp <$4.8-5.0T for $\theta = 60°$ and 6.8T $<\mu_0 H_\perp <$7.2-7.4T for $\theta = 45°$ in Fig.5.2(a)-(c) and Fig.5.2(e)-(g).

Next, Fig.5.3 shows the temperature dependence of the $\frac{\kappa_{xy}^{2D}}{T}$ adding the

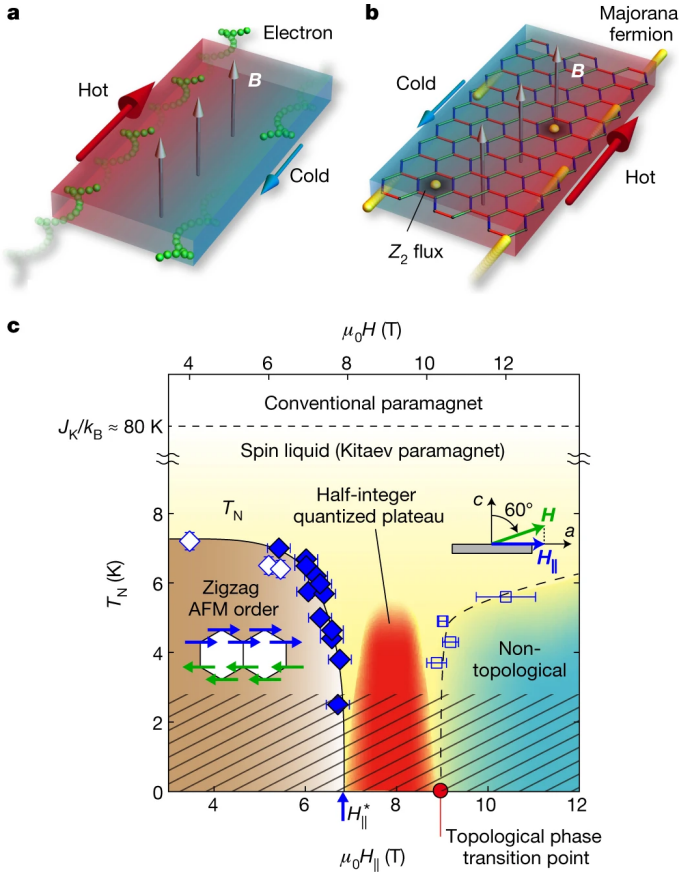


Figure 5.1: (a)is the schematic illustration of the integer quantum Hall state of a 2D electron gas, (b) is the schematic illustration of a Kitaev spin liquid state, (c) is the phase diagram of α-$RuCl_3$ in a magnetic field.[1]

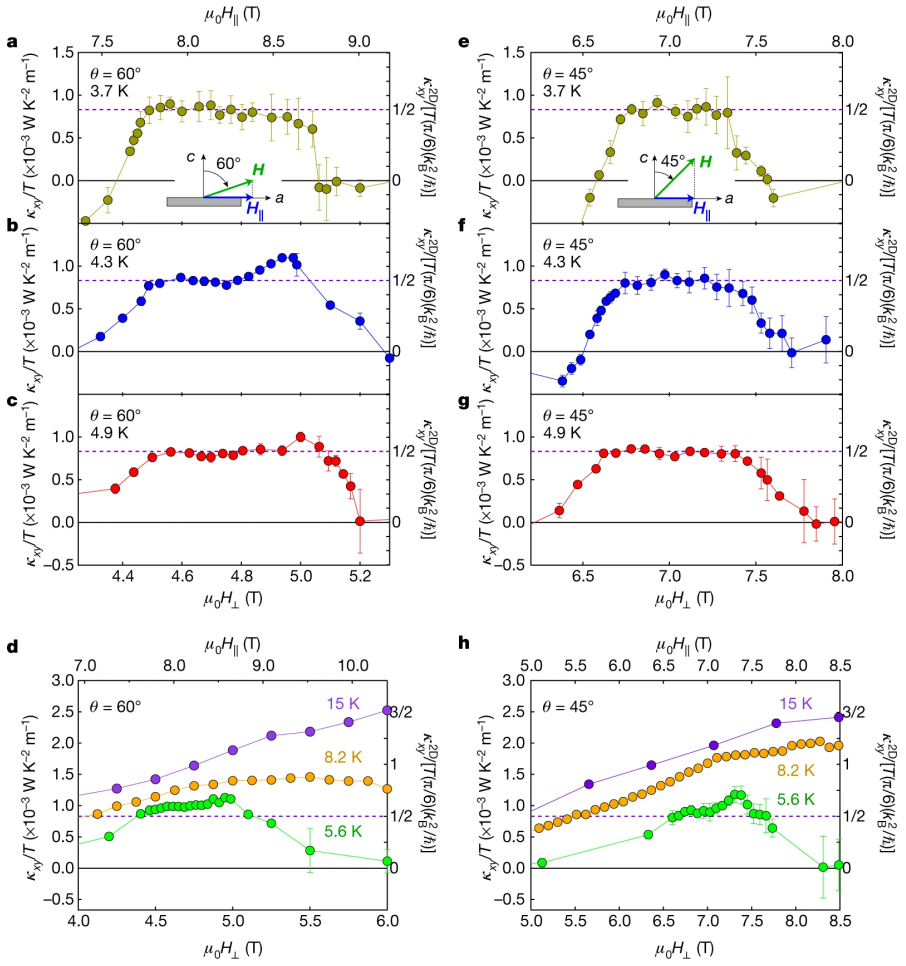


Figure 5.2: Thermal Hall conductivity $\frac{\kappa_{xy}}{T}$ in a field at $\theta = 60°$(a-d) and 45°(e-h).[1]

magnetic field where the plateau can be observed. The quantized thermal Hall conductivity can be observed below 5.5K. In the higher region, $\frac{\kappa_{xy}^{2D}}{T}$ rapidly increases with the temperature.

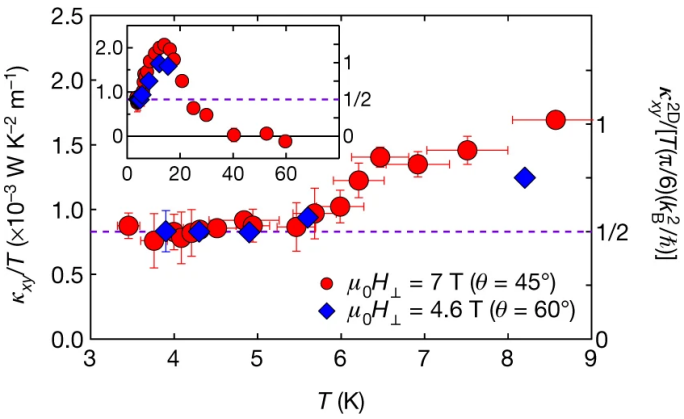


Figure 5.3: The temperature dependence [1].

Further experimental observations which support the half quantization of the thermal Hall effect in α-$RuCl_3$ are accumulating [1, 2, 3]. In particular, it has been reported that this quantized thermal Hall effect has a sample dependence associated with the longitudinal thermal conductivity κ_{xx} [2]. This κ_{xx} dependence may imply a scattering effect on the field-induced gap protecting the chiral edge currently[2]. They report that They report that a better-quality sample suppresses magnetic scattering effects, which is essential in realizing the quantized thermal Hall effect. Fig.5.4(e) shows the temperature dependence of κ^{xx} at zero fields and the difference in the qualities of the sample. They report that κ^{xx} measurements depend on the sample quality because κ^{xx} is decided by the difference in the mean free path of the heat carriers [2].

As shown in Fig.5.5(a), $\frac{\kappa_{xy}}{T}$ of sample A shows the flat for $\mu_0 H_{||}$ ~9T at lower temperatures. However, the magnitudes of $\frac{\kappa_{xy}}{T}$ of samples B and C are much smaller, as shown in Fig.5.5(b). They report the sample, which shows the smaller value of κ_{xx} cannot be observed in the quantized thermal Hall effect. They conclude that suppression of the magnetic field-dependent scattering contributes to the realization of the quantized thermal Hall effect.

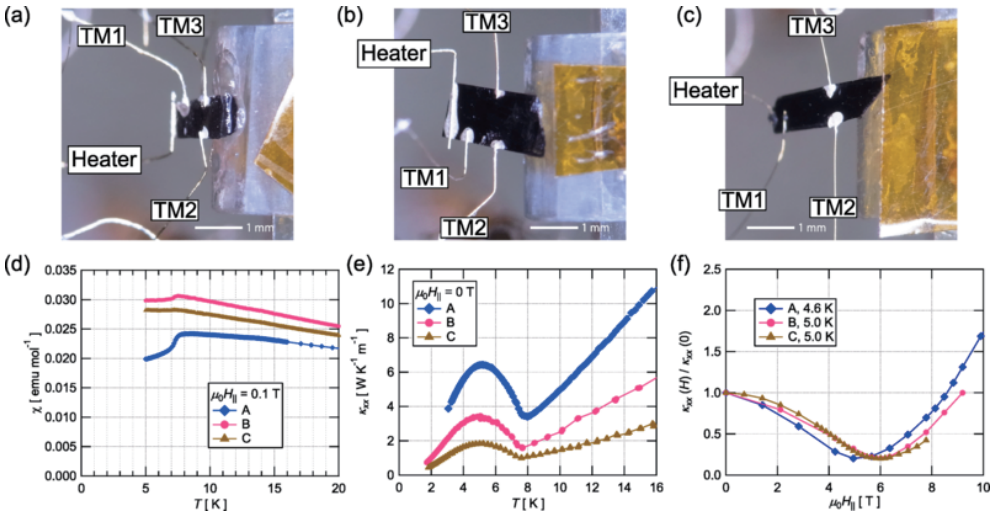


Figure 5.4: (a)-(c) Setup pictures of the samples. (d) The temperature depends on the magnetic susceptibility at 0.1T applied along the a-axis. (e) The temperature depends on the longitudinal thermal conductivity κ^{xx} at zero fields. (f) The field dependence of κ^{xx} at 4.6K(sample A) and 5.0K(samples B and C).[2]

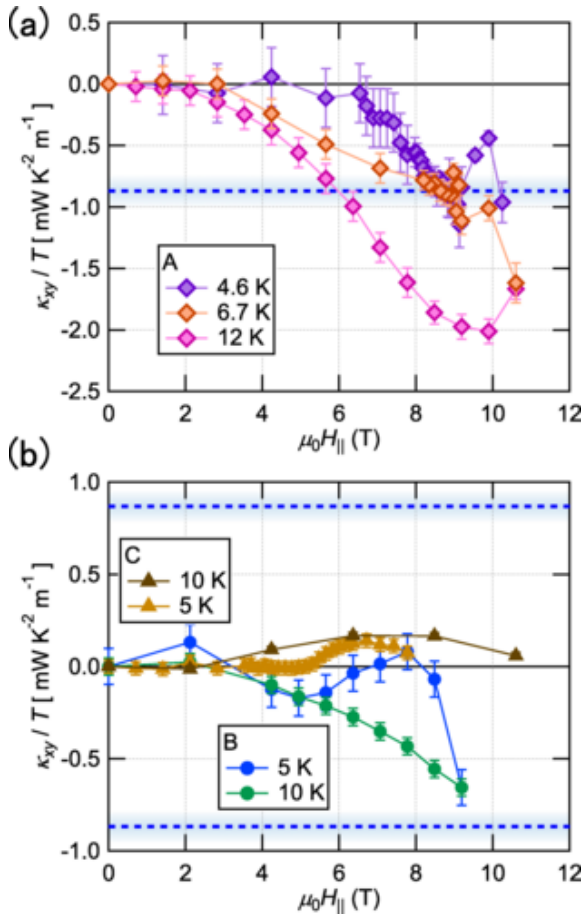


Figure 5.5: The field dependence of the thermal Hall conductivity divided by the temperature $\frac{\kappa_{xy}}{T}$ of (a) sample A and (b) samples B and C. The dotted lines show the value corresponding to the half-integer quantized thermal Hall effect.[2]

Furthermore, from the point of view of the edge theory, there is the argument that the coupling of phonons to the edge mode is a necessary condition for the observation of the quantized thermal Hall effect since the coupling of the phonons to the chiral spin liquid gives a Berry phase to the acoustic phonons, and a tiny correction to the quantized thermal Hall effect arises. This changes the phonos' equations of motion, allowing their trajectories to bend and carry heat in the perpendicular direction [35, 36].

As seen above problem, no consent for the observation of the Majorana fermion has been given by researchers. Therefore, it is still an important issue to confirm the existence of Majorana fermions from different and more direct approaches.

5.2 Specific heat

Next, we explain experimental studies on the specific heat that may exhibit the signature of the Majorana fermion obtained by quantum Monte Carlo (QMC) simulations [20] and experiment [63]. According to the results obtained by QMC, in the absence of the magnetic field, the specific heat shows the peak at two temperature points [20]. The specific heat is defined as,

$$C_v = \frac{1}{N^2 T}\left(\left\langle E_f^2\right\rangle - \left\langle E_f\right\rangle^2 - \left\langle \partial E_f/\partial\beta\right\rangle\right). \tag{5.1}$$

Fig.5.6(a)-(d) shows the specific heat versus temperature obtained by QMC and α is the paramter for the anisotropy of the Kitaev interaction $K_x = K_y = \frac{\alpha}{3}$ and $K_z = 1 - \frac{2\alpha}{3}$. (a) is the gapless B-phase, (d) is the gapped A-phase, and (c) is the phase boundary.(See Fig.3.4.) Since the entropy is released continuously on two levels and the flux density $W = \frac{2}{N}\sum_p \langle W_p\rangle$ is decreasing with lowering temperature as shown in Fig.5.6(e)-(h), the high-T crossover is due to the itinerant Majorana fermions. The low-T crossover is due to the thermal fluctuations of fluxes of the localized Majorana fermions. Thus, one can observe the thermal fractionalization from the paramagnetic spin to the Majorana in the specific heat [20].

We introduce the experimental results observing two peaks of specific heat without a magnetic field. Fig.5.7 shows the temperature dependence of the magnetic specific heat C_{mag}/T and the magnetic entropy S_{mag} at zero magnetic fields. The specific heat shows a broad peak at 85 K and a sharp peak at $T_N \simeq$15K, where the magnetic phase transition occurs. [61, 64] The

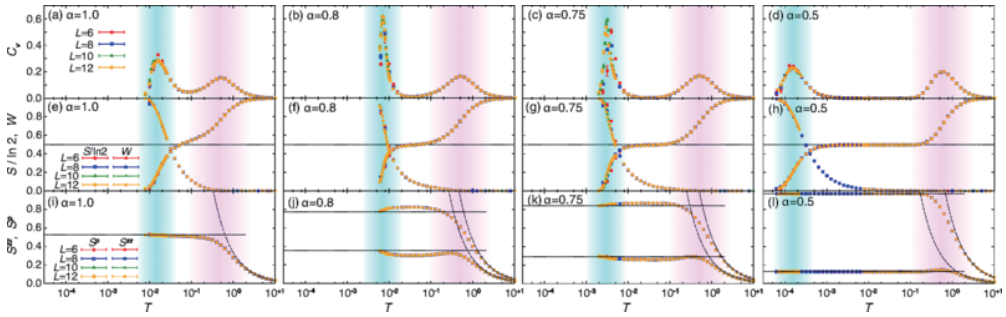


Figure 5.6: The specific heat in the absence of the magnetic field [20].

entropy of the high-T peak is consistent with the above theory. However, the contribution of the Z_2 flux in the low-T peak is hidden due to magnetic ordering emerging. This is because non-Kitaev interactions dominate in without the magnetic field [61, 62]. On the other hand, in a magnetic field, the magnetic order is suppressed. [65, 66, 67]

Significantly, the magnetic field angle dependence has recently been reported [63]. In the high-field paramagnetic phase, the specific heat shows the different behaviors between gapped B-phase excitations for $\mathbf{H}||\mathbf{a}$ and gapless B-phase excitations for $\mathbf{H}||\mathbf{b}$ in Fig.5.8. They argue that these differences are characteristic of itinerant Majorana fermions in the Kitaev spin liquid. However, it still needs to provide direct evidence of the Majorana fermions.

5.3 Inelastic neutron scattering

Inelastic neutron scattering or nuclear magnetic resonance are suitable for investigating spin dynamics. Here, we review inelastic neutron scattering with focus. The scattering intensity is proportional to the dynamic spin structure factor. Fig.5.9 shows the dynamical spin structure factor calculation in the ground state of the Kitaev spin liquid without a magnetic field [15, 68]. Here, the spin dynamical spin structure factor and the sum of the diagonal components are given by

$$S^{\mu\nu}(\mathbf{q},\omega) = \frac{1}{N}\sum_{\mathbf{R_i},\mathbf{R_j}}\int_{-\infty}^{\infty}\frac{dt}{2\pi}\left\langle S_i^{\mu}(t)S_j^{\nu}\right\rangle e^{i(\omega t-\mathbf{q}\cdot(\mathbf{R_i}-\mathbf{R_j}))}, \tag{5.2}$$

$$S(\mathbf{q},\omega) = S^{xx}(\mathbf{q},\omega)+S^{yy}(\mathbf{q},\omega)+S^{zz}(\mathbf{q},\omega), \tag{5.3}$$

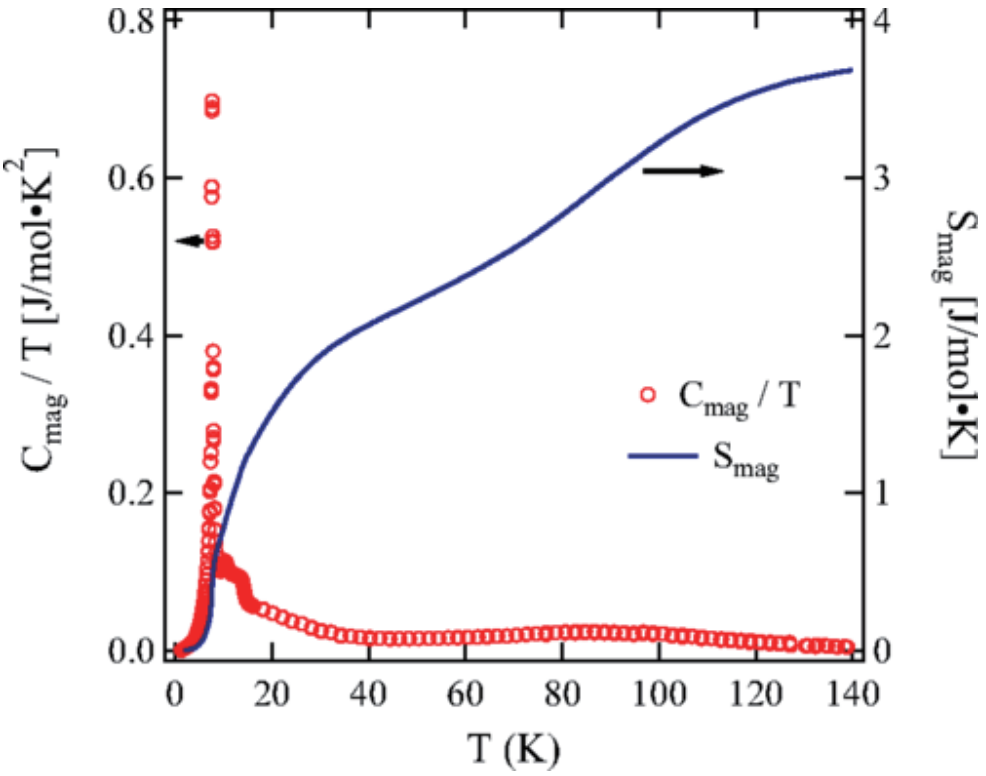


Figure 5.7: Temperature dependence of C_{mag}/T in α-$RuCl_3$ measured at zero magnetic field. The solid curve represents the magnetic entropy Smag. [64].

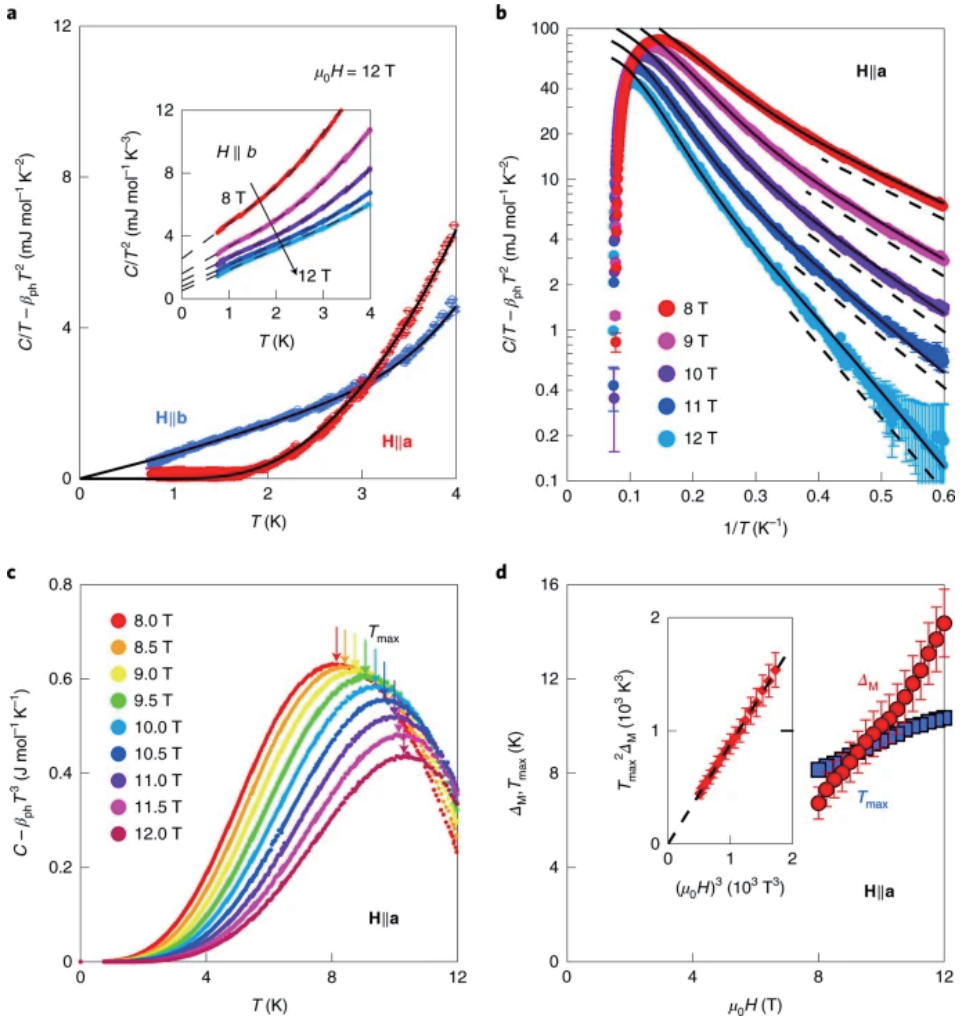


Figure 5.8: **a** is temperature dependence of $C/T - \beta_{ph}T^2$ for **H**//**a**(red) and **H**//**b**(blue) at 12T. **b** is the arrhenius plot $C/T - \beta_{ph}T^2$ for **H**//**a** at several fields. **c** is the temperature dependence of $C - \beta_{ph}T^3$ for for **H**//**a** at several fields. **d** is field dependence of Majorana gap Δ_M and the peak temperature T_{max} for **H**//**a**.[63]

where the i, j are the lattice site positions and $\mathbf{R}_i, \mathbf{R}_j$ are the the position vector.

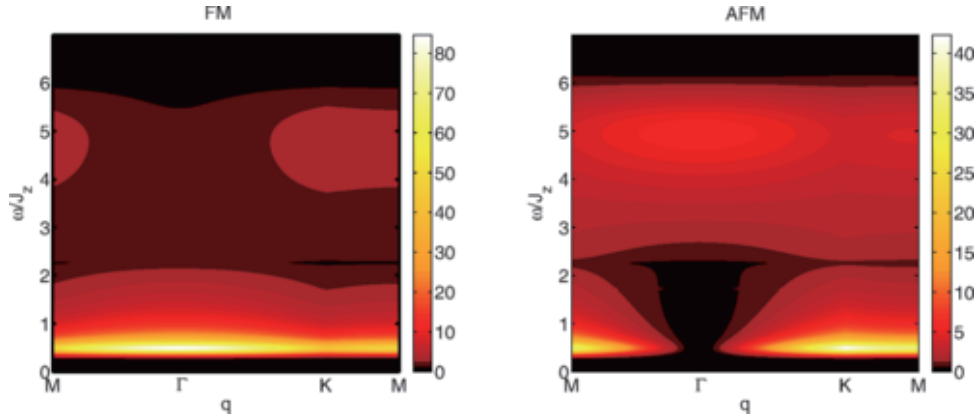


Figure 5.9: The dynamic structure factor $S^{aa}(\vec{q}, \omega)$ for the ferromagnetic Kitaev interaction(left) and antiferromagnetic Kitaev interaction(right) at the isotropic point, as a function of $\vec{q}$ and ω on the cut $M - \Gamma - K - M$ through the Brillouin zone[68].

Both results show the weak dependence on the wave vector $\mathbf{q}$, reflecting the short spin correlations. Also, in the low-energy region $\omega \sim 0.4J_z$, the intensity vanishes under the strong peak due to opening the gap in the flux excitations. The spin-flip excitation is accompanied by the Majorana fermions excitation and the Z_2 flux excitation (see the chapter 3). Thus, Fig.5.9 reflects the fractional excitation of the Z_2 fluxes. In the high-energy region $\omega \sim 6J_z$, the intensity disappears due to the contribution of the itinerant Majorana fermions.

In the experiment of α-$RuCl_3$ [23], we can observe the strong response different from the spin wave excitations of the magnetic ordering phase below the low-temperature magnetic ordering transition T_N shown in Fig.5.10. Also, in the high-energy region, the incoherent response behaves similarly to the theory behavior at $T = 0$.

5.4 Raman scattering

The Raman scattering experiments provide the spin density information from the photon emitted by the light scattering effect and is helpful in investigating

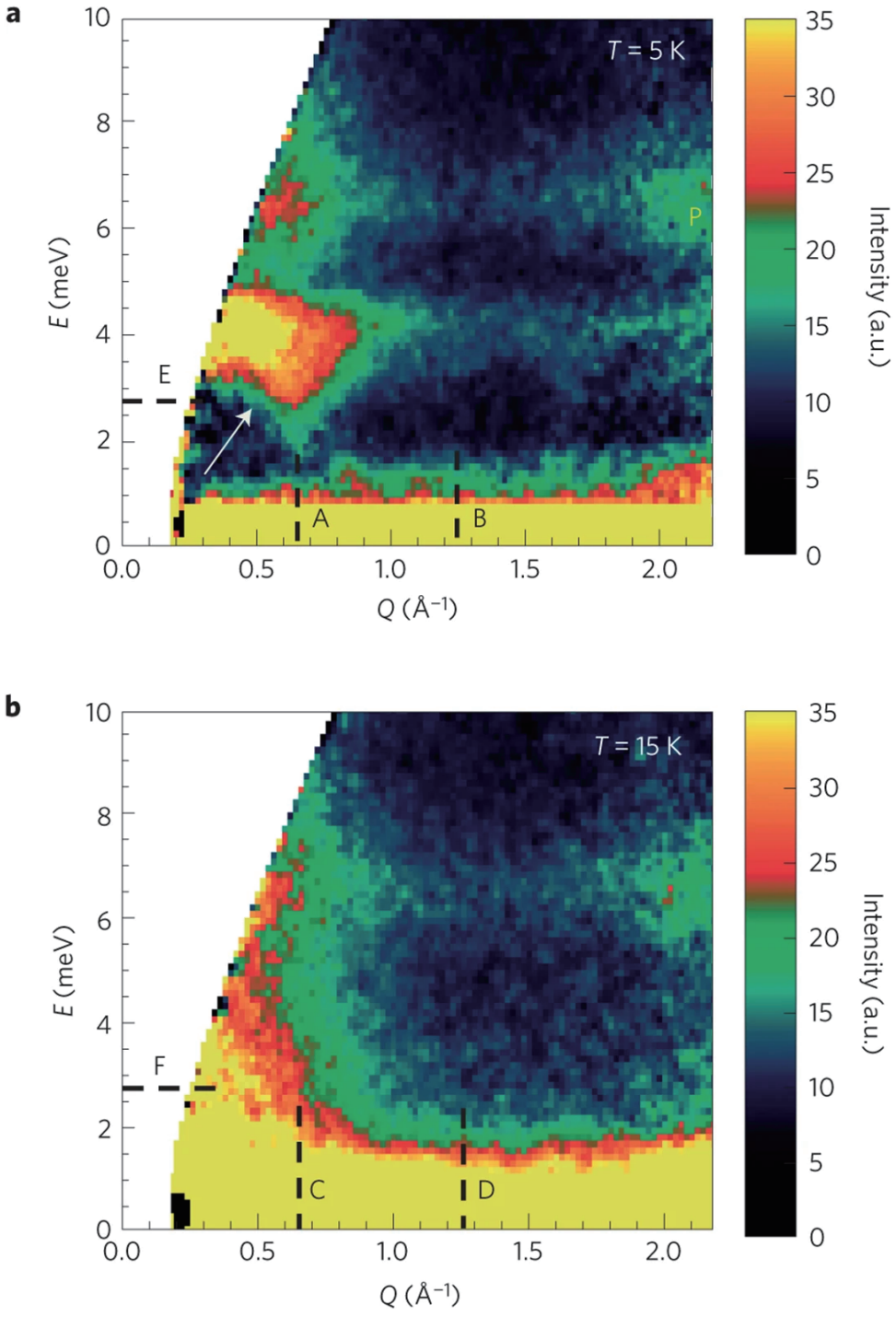


Figure 5.10: Collective magnetic modes measured with inelastic neutron scattering for a powder sample of α-$RuCl_3$ using 25 meV incident neutrons [23]. a shows T=5K below the low-temperature magnetic ordering transition T_N and b shows T =15K

magnetic excitations. The Raman response intensity is given by [69]

$$I(\omega) = \frac{1}{N}\int_{-\infty}^{\infty} dt \left\langle \hat{R}(t)\hat{R}(0)\right\rangle e^{i\omega t}, \tag{5.4}$$

$$\hat{R} = \sum_{\langle ij\rangle_a} (\hat{\epsilon}_{in}\cdot \mathbf{d}_a)(\hat{\epsilon}_{out}\cdot \mathbf{d}_a)(K_K \hat{S}_i^a \hat{S}_j^a + K_H \hat{\mathbf{S}}_i \hat{\mathbf{S}}_j), \tag{5.5}$$

where $\mathbf{d}_a$ are lattice vectors, and $\hat{\epsilon}$ are polarization vectors of the photons. Fig.5.11 shows the calculated Raman scattering intensity from the ground state of Kitaev spin liquid[69]. The weak polarisation-dependent response in the figure is related to the flux or itinerant Majorana. The sharp peak of $\mathbf{I}_{\mathrm{H}}^{[0]}$ at the four flux gaps $\Delta_F = 0.446 J_K$ indicates flux excitation from a gapless QSL[70].

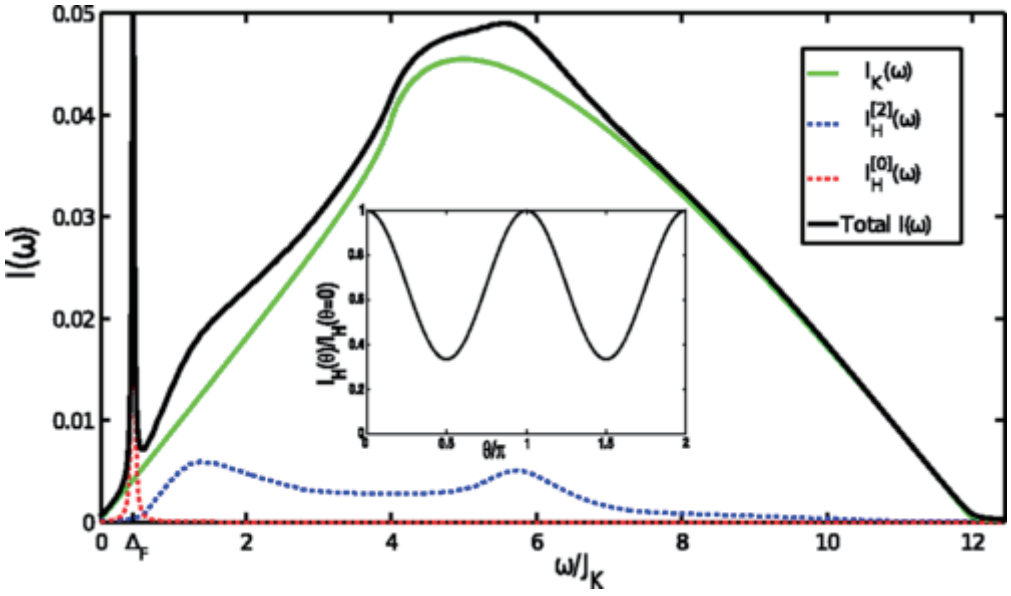


Figure 5.11: The Raman response $I(\omega)$ and compontes [69]. $I_K(\omega)$ is the Kitaev contribution which shows the fermion density of states. $I_H^{[0]}(\omega)$ and $I_H^{[2]}(\omega)$ are the zero and two-particle responses of the Heisenberg contribution.

Fig. shows the measurements of magnetic light scattering in α-$RuCl_3$ at T=5K and a broad continuum contribution in the blue region. This behavior is consistent with the theoretical prediction at T=0K [69] and not

conventional two-magnon scattering or structural disorder [70]. These results suggest the unusual magnetic excitations similar to Majorana fermion in the quantum spin liquid. However, it is still under debate whether the Raman scattering experiments provide evidences of Majorana fermions.

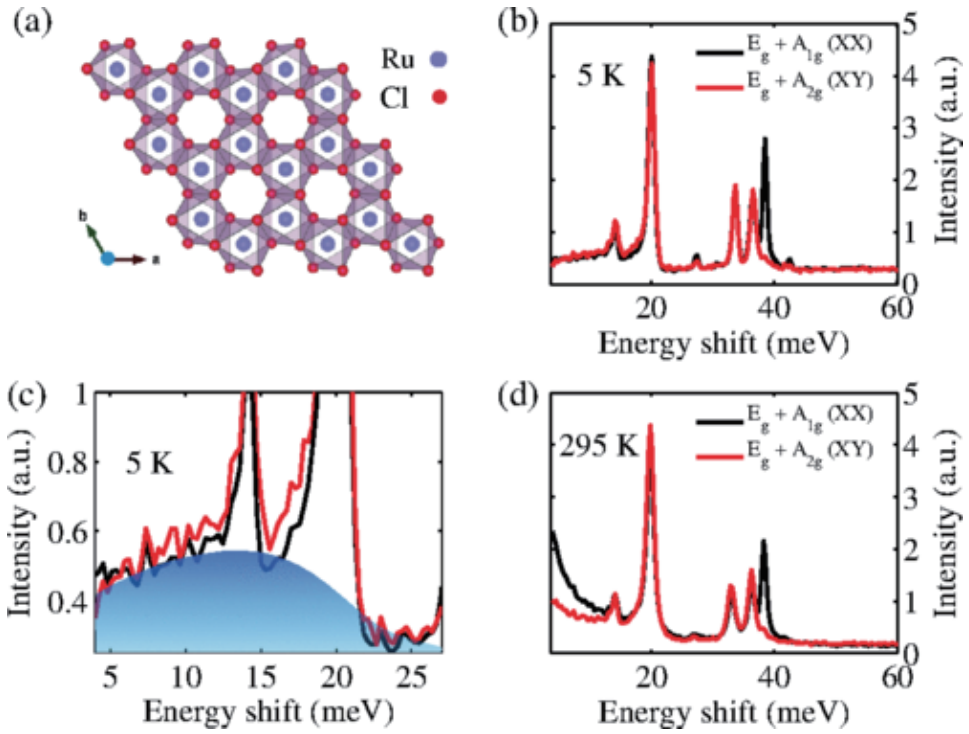


Figure 5.12: Structure and polarization Raman response of α-$RuCl_3$. (a) Lattice structure (b) 5K Raman intensity. (c)Low energy detail(d) 295K Raman intensity. [70].

Chapter 6

Edge spin Seebeck effect

In this chapter, we propose the universal scaling of the Drude weight of the edge spin Seebeck effect of the Kitaev model as definitive evidence of the existence of Majorana fermions. The spin Seebeck effect is a phenomenon in which temperature difference imposed on opposite sides of a sample produces the flow of a spin current. In the Kitaev spin liquid, spins are fractionalized into Majorana fermions, and it has an extremely short spin correlation length close to a lattice constant in the bulk. Despite this feature, it is found that a dissipationless spin current flow at the edge of the system, which leads to the spin Seebeck effect. We here use the temperature dependence of the Drude weight of this edge spin Seebeck effect as the signature of the Majorana edge mode. This signature is expected to be more general and stable than the thermal Hall effect. This is because it does not require quantitatively precise measurements like the half-quantized thermal Hall effect, and the qualitative temperature dependence is not expected to be affected even if it is disturbed by other degrees of freedom, such as phonons. Furthermore, this proposal is also useful for the application to spintronics devices. The Kitaev spin liquid state remains stable down to the atomic scale and enables the generation of a spin current without dissipation due to the existence of a chiral Majorana edge mode. The spin current may be detected via the measurement of the surface magnetization generated by the spin accumulation or the inverse spin Hall effect. This makes it possible to fabricate a highly integrated device with substantial efficiency to generate a spin current, paving the way to *Kitaev spintronics*.

6.1 Model set-up

The model set-up of this thesis for the edge spin Zeebeck effect is illustrated in Fig. 6.1. We consider an open boundary condition for the y-direction and a periodic boundary condition for the x-direction. The unit cell of the system is shown in Fig. 6.2. We label unit cells as $l = 1, \ldots, L_x$, where L_x is the number of unit cells, from left to right. For this configuration, the gauge-field Majorana fermions included in the top and bottom spins at open edges, $b^z_{l,1}$ and $b^z_{l,N}$, can not form the Z_2 gauge fields [71, 72, 73, 74]. Thus, the perturbative calculations within the vortex-free sector described in the previous section are not applicable to these sites.

We assume that there are total N sites in the unit cell. Within the vortex-free sector, the Hamiltonian of the system of this thesis under an applied magnetic field with $h_x h_y h_z \neq 0$ is expressed as,

$$\begin{aligned}
\mathcal{H} &= \mathcal{H}_K + \mathcal{H}^{(3)} - \sum_l (h_z S^z_{l,1} + h_z S^z_{l,N}), && (6.1)\\
&=: \frac{1}{2} \sum_{(l,m),(l',n)} c_{l,m} A_{(l,m)(l',n)} c_{l',n}, && (6.2)\\
\mathcal{H}_K &= -\sum_{\langle ij \rangle_\alpha} K_\alpha S^\alpha_i S^\alpha_j, && (6.3)\\
\mathcal{H}^{(3)} &= -\Delta \sum_{i,j,k} S^x_i S^y_j S^z_k, && (6.4)\\
\Delta &\sim \frac{h_x h_y h_z}{K^2}, && (6.5)
\end{aligned}$$

where $\mathcal{H}_K$ is the Hamiltonian of the Kitaev model, $\mathcal{H}^{(3)}$ is the mass term generated by third order perturbations in the magnetic field, and the last term in the first line is the Zeeman term for edge spins. $\langle ij \rangle_\alpha$, $\langle jk \rangle_\beta$ with $\alpha \neq \beta$, and we assume $K = K_x = K_y = K_z$ here for simplicity in the derivation of Δ. Although the first-order term in the magnetic field is suppressed in the bulk of the spin liquid state, the edge Zeeman term is not negligible, as described below. In the second line of Eq. (6.2), l and l' label the indices of the unit cell, while m and n label the sites inside the unit cell. A key idea of the derivation of the Majorana Hamiltonian Eq. (6.2) is to identify the gauge-field Majorana operators $b^z_{l,1}$ and $b^z_{l,N}$ with new matter Majorana operators $c_{l,0}$ and $c_{l,N+1}$, respectively, and m (and n) runs from 0 to $N+1$. This enables

us to treat the edge Zeeman term exactly. We write the coordinate of the (l, m) site as $\boldsymbol{r}_{l,m} = (x_{l,m}, y_{l,m})$. We use the Fourier transformation of $c_{l,m}$ only in the x-direction; $c_{l,m} \to c_{k_x,m}$ Then, the Bloch Hamiltonian can be written as,

$$\mathcal{H} = \frac{1}{2}\sum_{k_x,m,n} c^\dagger_{k_x,m}\mathcal{H}_{k_x,m,n}c_{k_x,n}, \tag{6.6}$$

$$\mathcal{H}_{k_x,m,n} := 2\sum_{l,l'} e^{-\mathrm{i}k_x(x_{l,m}-x_{l',n})}A_{(l,m)(l',n)}. \tag{6.7}$$

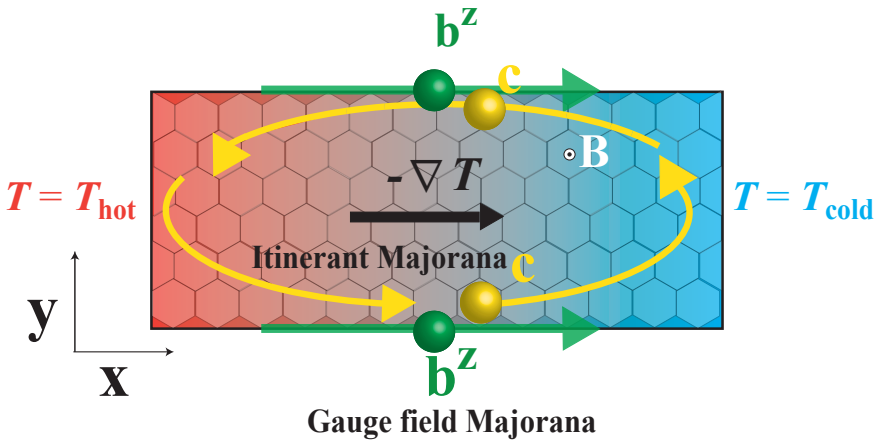


Figure 6.1: Experimental set-up of the spin Seebeck effect.[75]

6.2 Definition of energy current and spin current

To evaluate the spin Seebeck coefficient, we introduce the energy polarization operator as,

$$\boldsymbol{P}_E = \frac{1}{2}\sum_{(l,m)(l',n)} \frac{\boldsymbol{r}_{l,m}+\boldsymbol{r}_{l',n}}{2} c_{l,m}A_{(l,m)(l',n)}c_{l',n}, \tag{6.8}$$

where $A_{(l,m)(l',n)}$ is defined in Eq. (6.2). We introduce the energy current operator as $\boldsymbol{J}_E = \mathrm{i}[\mathcal{H}, \boldsymbol{P}_E]$. Note that since the chemical potential is always zero in the Kitaev system, $\boldsymbol{J}_E$ is equal to the thermal current operator.

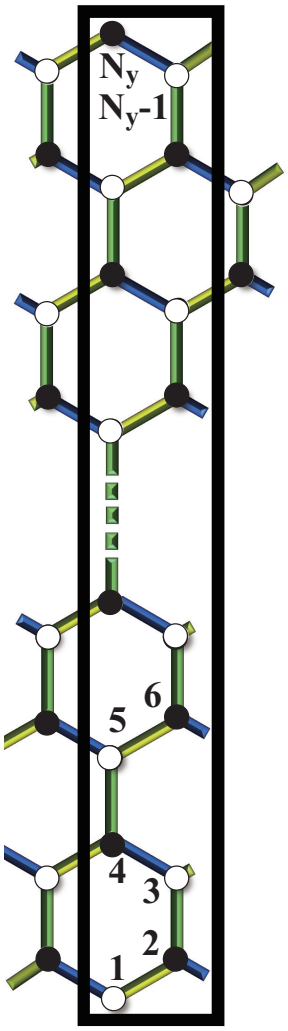


Figure 6.2: Unit cell of the system with open edges in the y direction.[75]

We emphasize that although it is impossible to express the spin and spin current operators in the bulk only in terms of c-operators, the spin operator at the edge can be still written solely in terms of matter Majorana fermions, because we redefined $b^z_{l,1}$ and $b^z_{l,N}$ as $c_{l,0}$ and $c_{l,N+1}$, respectively. The total S^z at the edge, $S^{\rm edge}_z = \sum_l \left[S^z_{l,1} + S^z_{l,N}\right]$, can be written in terms of a skew symmetric matrix $B_{(l,m)(l',n)}$,

$$S^{\rm edge}_z =: \frac{1}{2} \sum_{(l,m),(l',n)} c_{l,m} B_{(l,m)(l',n)} c_{l',n}. \tag{6.9}$$

We define the spin current operator using this B matrix as,

$$J^x_s := \frac{1}{4} \sum_{k_x,m,n} \left[v_{k_x} S^z_{k_x} + S^z_{k_x} v_{k_x}\right]_{mn} c^\dagger_{k_x,m} c_{k_x,n}, \tag{6.10}$$

$$[S^z_{k_x}]_{m,n} := \sum_{l,l'} 2e^{-{\rm i}k_x(x_{l,m}-x_{l',n})} B_{(l,m)(l',n)}, \tag{6.11}$$

where $v_{k_x} = \frac{\partial \mathcal{H}_{k_x}}{\partial k_x}$. There is an ambiguity in the definition of the spin current when spins are not conserved. Thus, we simply employ a conventional definition relevant to experimental detection, using the anticommutation of the group velocity v_{k_x} and the edge spin $S^z_{k_x}$.

6.3 Edge spin Seebeck effect

6.3.1 Kubo formula

The spin Seebeck effect is characterized by the Kubo correlation function $\kappa^{xx}_{\rm Kubo}$ for the spin current and the energy current as $\langle J^x_s \rangle_{\nabla T} / L_x = -\kappa^{xx}_{\rm Kubo} \nabla_x T$. We note that the longitudinal component is obtained directly from the Kubo formula, whereas the transverse component needs a contribution from the

gravitational magnetization additionally [29, 54, 76]. We obtain,

$$\kappa^{xx}_{\rm Kubo}(T,\omega) = 2\pi D(T)\delta(\omega)+\kappa^{reg}(T,\omega), \tag{6.12}$$

$$D(T) = -\frac{1}{TL_x}\sum_{k_x,u,v,E_{k_x,u}=E_{k_x,v}} J^E_{k_x,u,v}J^s_{k_x,v,u}f'(E_{k_x,u}), \tag{6.13}$$

$$\kappa^{reg}(T,\omega) = -\frac{2\pi}{TL_x}\sum_{k_x,u,v,E_{k_x,u}\neq E_{k_x,v}} J^E_{k_x,u,v}J^s_{k_x,v,u} \times \delta(\omega+E_{k_x,v}-E_{k_x,u})\frac{f(E_{k_x,v})-f(E_{k_x,u})}{E_{k_x,v}-E_{k_x,u}}, \tag{6.14}$$

where the $D(T)$ is the Drude weight and $\kappa^{reg}(T,\omega)$ is the regular part of $\kappa^{xx}_{\rm Kubo}(T,\omega)$, $E_{k_x,u}$ is an eigenvalue of the Bloch Hamiltonian, and $f(E)$ is the Fermi distribution function. $J^s_{k_x,u,v}$ and $J^E_{k_x,v,u}$ are, respectively, spin and energy currents.

6.3.2 Derivation of the conductivity

Here, we show the detail of the derivation of the spin Seebeck conductivity Eq. (6.12)-(6.14)in the main text. We first diagonalize the Hamiltonian, whose labels run from 0 to $N+1$ because the unit cell additionally includes gauge-field Majorana fermions on the boundaries.

$$\vec{c}_{k_x} = (c_{k_x,0},c_{k_x,1},\ldots,c_{k_x,N},c_{k_x,N+1})^T, \tag{6.15}$$

$$\mathcal{H} = \frac{1}{2}\sum_{k_x}\vec{c}^{\dagger}_{k_x}\mathcal{H}_{k_x}\vec{c}_{k_x}, \tag{6.16}$$

$$\mathcal{H}_{k_x,m,n} := 2\sum_{l,l'} e^{-{\rm i}k_x(x_{lm}-x_{l'n})}A_{(l,m)(l,n)}. \tag{6.17}$$

Due to the particle-hole symmetry, all eigenvalues appear in pair with opposite signs and the same absolute value. Thus, we label positive eigenvalues $E_{k_x,n}$ $(n=1,2,\ldots,\frac{N}{2},\frac{N}{2}+1)$, and negative ones $E_{k_x,-n}$ $(=-E_{k_x,n})$. The Bloch Hamiltonian is diagonalized as,

$$U^{\dagger}_{k_x}\mathcal{H}_{k_x}U_{k_x} = {\rm diag}(E_{k_x,-\frac{N}{2}-1},E_{k_x,-\frac{N}{2}},\ldots,E_{k_x,-1},E_{k_x,1}, \ldots,E_{k_x,\frac{N}{2}},E_{k_x,\frac{N}{2}+1}), \tag{6.18}$$

with a unitary matrix U_{k_x}. We introduce a fermionic operator f to diagonalize the Hamiltonian as,

$$\vec{f}^{\dagger}_{k_x} = \vec{c}^{\dagger}_{k_x} U_{k_x}, \ \vec{f}_{k_x} = U^{\dagger}_{k_x} \vec{c}_{k_x} \tag{6.19}$$

Thus, the Hamiltonian can be recast into,

$$\mathcal{H} = \frac{1}{2} \sum_{k_x} \vec{c}^{\dagger}_{k_x} U_{k_x} U^{\dagger}_{k_x} \mathcal{H}_k U_{k_x} U^{\dagger}_{k_x} \vec{c}_{k_x}, \tag{6.20}$$

$$= \frac{1}{2} \sum_{k_x} E_{k_x,n} f^{\dagger}_{k_x,n} f_{k_x,n}, \tag{6.21}$$

Next, we define an energy current operator for the honeycomb Kitaev model. We first introduce an energy polarization operator as,

$$P^x_E = \frac{1}{2} \sum_{(m,l)(n,l')} \frac{x_{m,l} + x_{n,l'}}{2} c_{m,l} A_{(m,l)(n,l')} c_{n,l'} \tag{6.22}$$

$$\tag{6.23}$$

Then, we define an energy current as,

$$J^x_E = \mathrm{i}[\mathcal{H}, P^x_E]. \tag{6.24}$$

We introduce a group velocity as,

$$v_{k_x,m,n} = \frac{\partial \mathcal{H}_{k_x,m,n}}{\partial k_x} \tag{6.25}$$

$$= (-2\mathrm{i}) \sum_{l,l'} (x_{l,m} - x_{l',n}) A_{(l,m)(l',n)} e^{-\mathrm{i}k_x (x_{l,m} - x_{l',n})}, \tag{6.26}$$

Then, the energy current is written as,

$$J^x_E = \frac{1}{4} \sum_{k_x,m,n} c^{\dagger}_{k_x,m} [v_{k_x} \mathcal{H}_{k_x} + \mathcal{H}_{k_x} v_{k_x}]_{m,n} c_{k_x,n}. \tag{6.27}$$

Using fermionic operators given by Eq. (6.19), we can rewrite the energy current as,

$$J^x_E = \sum_{k_x,u,v} J^E_{k_x,u,v} f^{\dagger}_{u,k_x} f_{v,k_x}, \tag{6.28}$$

$$J^E_{k_x,u,v} = \frac{1}{4} (E_{u,k_x} + E_{v,k_x}) \left[U^{\dagger}_{k_x} \frac{\partial \mathcal{H}_{k_x}}{\partial k_x} U_{k_x} \right]_{u,v}. \tag{6.29}$$

Similarly, we can rewrite the spin current operator as,

$$J_s^x = \sum_{k_x,u,v} J^s_{k_x,u,v} f^\dagger_{u,k_x} f_{v,k_x}, \tag{6.30}$$

$$J^s_{k_x,u,v} = \frac{1}{4}\left[U^\dagger_{k_x}\left(\frac{\partial \mathcal{H}_{k_x}}{\partial k_x} S^z_{k_x} + S^z_{k_x}\frac{\partial \mathcal{H}_{k_x}}{\partial k_x}\right) U_{k_x}\right]_{u,v}. \tag{6.31}$$

Finally, the spin Seebeck conductivity $\kappa^{\mu\nu}$ (μ, $\nu = x$, y) is defined by,

$$\langle J_s^\mu \rangle_{\nabla T}/L_x = -\kappa^{\mu\nu}\nabla_\nu T, \tag{6.32}$$

where L_x is the number of unit cells and $\langle O\rangle_{\nabla T}$ is the expectation value of O in the presence of a thermal gradient ∇T. We here focus on the longitudinal component. The longitudinal conductivity can be evaluated from the Kubo formula,

$$\kappa^{xx}_{\rm Kubo}(\omega) = \frac{1}{TL_x}\int_0^\infty {\rm d}t\ e^{{\rm i}(\omega+{\rm i}\delta)t}\int_0^\beta {\rm d}\lambda \langle J^x_E(-{\rm i}\lambda) J^x_s(t)\rangle, \tag{6.33}$$

where $J^x_\alpha(t) = e^{i\mathcal{H}t}J^x_\alpha e^{-i\mathcal{H}t}$ ($\alpha = s$, E) and $\beta = 1/T$ is the inverse temperature. Using Eq. (6.28)-(6.31), the Wick's theorem, and $E_{k_x,n} = E_{-k_x,n}$ derived from the inversion symmetry, $\kappa^{xx}(\omega)$ can be recast into Eq. (6.12)-(6.14).

Here, we have used $J^E_{-k_x,-u,-v} = -J^E_{k_x,v,u}$ because $v_{-k_x} = -v_{k_x}$. $D(T)$ is the Drude weight of the spin Seebeck conductivity, which characterizes the ballistic transport at $\omega = 0$. $f'(E)$ means the derivative of the Fermi distribution $f(E) = 1/(e^{\beta E}+1)$.

6.3.3 Ballistic edge transport

By using the Kubo formula obtained in the previous section, we calculate the spin Seebeck conductivity $\kappa^{xx}_{\rm Kubo}$. We, here, present the numerical results for the Drude weight and the regular part of $\kappa^{xx}_{\rm Kubo}(T,\omega)$ in the dc limit, *i.e.* $\omega \to 0$. We note that the regular part and the Drude Weight are always negative in the definition of the spin current of this thesis.

To confirm whether the existence of edge states affects the spin Seebeck effect or not, we first perform the calculation for both the A-phase and the B-phase of the Kitaev model as shown in Fig. 6.3-Fig. 6.6. The parameters for Fig. 6.3 and Fig. 6.5 are $K_x = 1$, $K_y = K_z = 0.1$, $\Delta = 0$, $h_z = 0.1$,

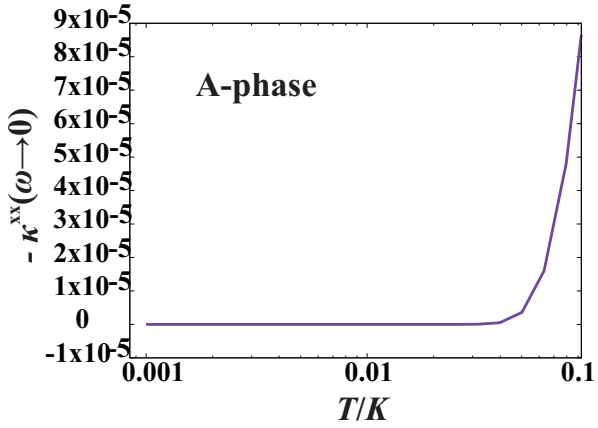


Figure 6.3: Plots of κ^{reg} and $D(T)$ versus T. κ^{reg} for the A-phase. The parameters for the A-phase are $(K_x, K_y, K_z, h_z, \Delta, N, L_x) = (1.0, 0.1, 0.1, 0.1, 0, 80, 1000)$. The parameters for the B-phase are $(K_x, K_y, K_z, h_z, \Delta, N, L_x) = (1.0, 1.0, 1.0, 0.1, 0.01, 80, 1000)$[75].

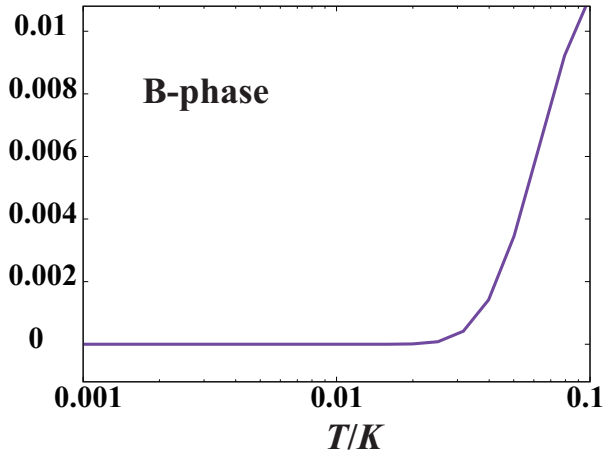


Figure 6.4: Plots of κ^{reg} and $D(T)$ versus T. κ^{reg} for the B-phase. The parameters for the A-phase are $(K_x, K_y, K_z, h_z, \Delta, N, L_x) = (1.0, 0.1, 0.1, 0.1, 0, 80, 1000)$. The parameters for the B-phase are $(K_x, K_y, K_z, h_z, \Delta, N, L_x) = (1.0, 1.0, 1.0, 0.1, 0.01, 80, 1000)$[75].

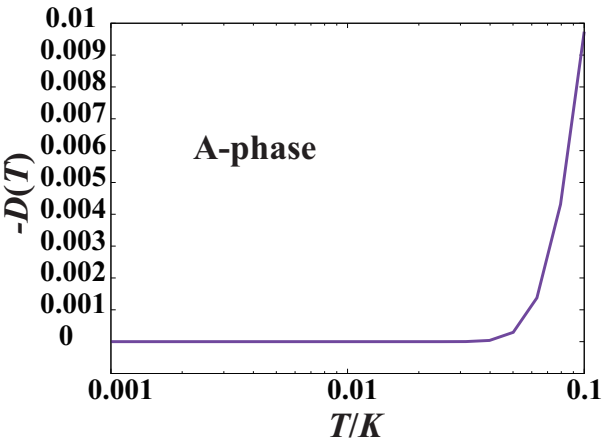


Figure 6.5: Plots of κ^{reg} and $D(T)$ versus T. $D(T)$ for the A-phase. The parameters for the A-phase are $(K_x, K_y, K_z, h_z, \Delta, N, L_x) = (1.0, 0.1, 0.1, 0.1, 0, 80, 1000)$. The parameters for the B-phase are $(K_x, K_y, K_z, h_z, \Delta, N, L_x) = (1.0, 1.0, 1.0, 0.1, 0.01, 80, 1000)$[75].

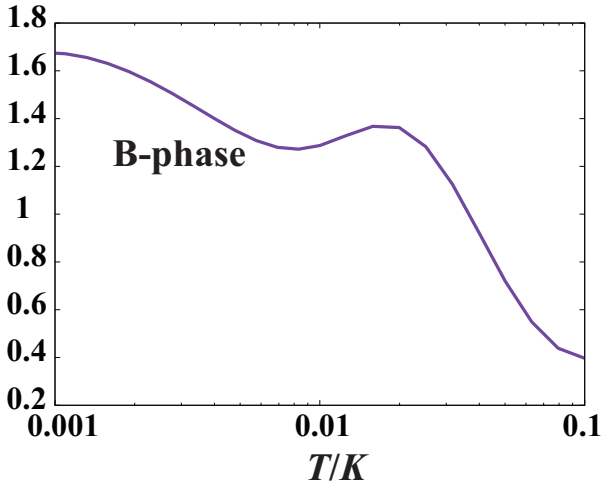


Figure 6.6: Plots of κ^{reg} and $D(T)$ versus T. $D(T)$ for the B-phase. The parameters for the A-phase are $(K_x, K_y, K_z, h_z, \Delta, N, L_x) = (1.0, 0.1, 0.1, 0.1, 0, 80, 1000)$. The parameters for the B-phase are $(K_x, K_y, K_z, h_z, \Delta, N, L_x) = (1.0, 1.0, 1.0, 0.1, 0.01, 80, 1000)$[75].

$N = 80$, and $L_x = 1000$, which correspond to the gapped A-phase. The parameters for Fig. 6.4 and Fig. 6.6 are $K_X = K_y = K_z = 1$, $\Delta = 0.01$, $h_z = 0.1$, $N = 80$, and $L_x = 1000$, which correspond to the gapped B-phase with a chiral edge mode. It is cautioned that the calculations are valid only for low temperature regions below 0.01 K, where the effective Hamiltonian is applicable. We show the results in high temperature regions above 0.01 K just for examining the contributions of the bulk gapful excitations to the regular part of the conductivity. As shown in Figs. 6.3-Fig. 6.4, κ^{reg} has only the bulk contribution. By comparing Fig. 6.5 and Fig. 6.6 we can easily see that there is an edge contribution only in the B-phase. The fact that the contribution of the chiral edge mode appears in the Drude weight means that the transport via the edge mode is protected from backscatterings, resulting in the generation of ballistic spin current at the edge.

An important feature of the Drude weight arising from chiral Majorana edge contributions is the universal temperature scaling at low temperatures. In Fig. 6.7-Fig. 6.8, we show the temperature dependence of the Drude weight divided by the temperature $D(T)/T$ at low temperature with $h_z = 0.1, 1.0$. In the case of Fig. 6.7, the parameters are set to $K_x = K_y = K_z = 1$, $\Delta = 0.05$, $N = 80$, and $L_x = 1000$. In the case of Fig. 6.7, the data are fitted by the fitting function shown in the solid line in the region from $T = 2.0 \times 10^{-6}$ to $T = 2.0 \times 10^{-5}$. We use the fitting function $g(T) = a + bT^c$, and the result is that $a = 3258.68(2)$, $b = -7.321(3) \times 10^{10}$, $c = 2.08(2)$. In the case of Fig. 6.8, the data are fitted by the fitting function shown in the solid line in the region from $T = 10^{-4}$ to $T = 10^{-3}$. The result is that $a = 327.027(3)$, $b = -1.9(2) \times 10^6$, $c = 2.02(2)$. This result shows nearly T^2 correction to $D(T)/T$ at low temperature. We stress that this temperature dependence is robust against any perturbations due to disorder or phonons, because it arises from the chiral character of the Majorana edge states with no backscatterings. This signature can be utilized for a clear-cut experimental detection of the Majorana edge states.

6.4 Conformal field theory description

To see the property of the dissipationless transport in more details, we further investigate the Drude weight from a different perspective. This transport problem of the chiral edge mode is essentially one-dimensional (1D), and conformal field theory (CFT) is known to be a powerful tool to investigate

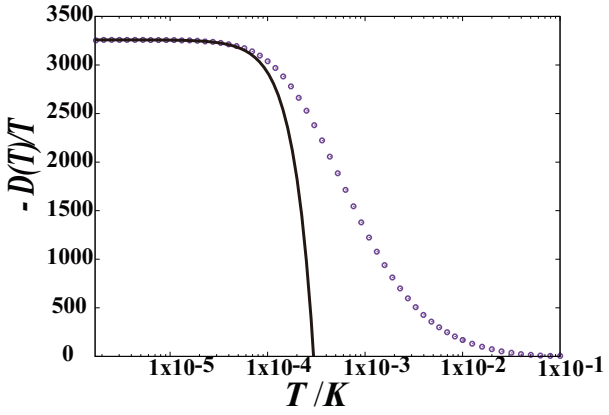


Figure 6.7: Logarithmic plot of $D(T)/T$ versus T/K. For the parameter set $(h_z, \Delta, N, L_x) = (0.1, 0.05, 80, 1000)$. White circles are the numerically calculated data, and the black line is the line fitting between $T = 2.0 \times 10^{-6}$ and $T = 2.0 \times 10^{-5}$[75].

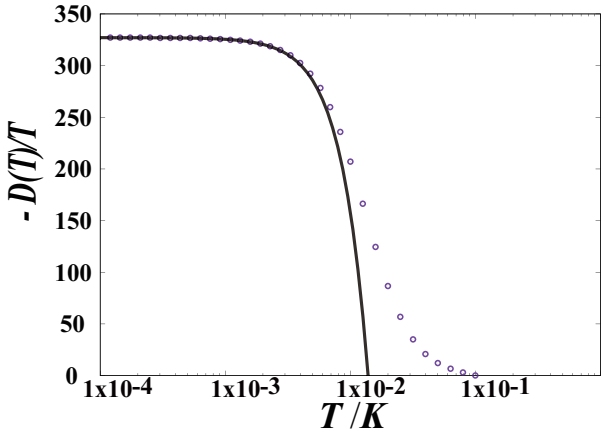


Figure 6.8: Logarithmic plot of $D(T)/T$ versus T/K. $(h_z, \Delta, N, L_x) = (1.0, 0.05, 80, 1000)$. The black line is the line fitting between $T = 10^{-4}$ and $T = 10^{-3}$[75].

such a 1D system.

Before going into the CFT description, we show band structures (with gauge-field Majorana fermions at the edge) in Fig. 6.9-Fig. 6.11. In Fig. 6.9-Fig. 6.11, we change the magnetic field in the z-direction from $h_z = 0.01$ to $h_z = 1.0$. The magnetic field h_z determines the coupling between matter Majorana fermions and gauge-field Majorana fermions. In the small coupling region shown in Fig. 6.9, the cross point where the edge state passes zero energy is not well-defined because the energy band of the edge state becomes flat. However, as we increase the coupling strength, the edge state becomes dispersive as shown in Fig. 6.10-Fig. 6.11. In other words, the unique flat band of the zigzag edge with $h_z = 0$ becomes chiral due to the mixing with gauge-field Majorana fermions, so that we can expect that CFT is applicable in the large-field region. Thus, we investigate the temperature dependence of the Drude weight in the region where h_z is large enough, and compare the results with the CFT prediction. The Drude weight behaver at low temperature shown in Fig. 6.7-Fig. 6.8 is consistent with the Ising CFT when the magnetic field becomes large enough [77, 78]. From the prediction of CFT, the correction of $D(T)$ from the T-linear contribution always begins from T^2. It is known that the leading irrelevant operator of the chiral Ising CFT is the energy-momentum tensor to the second power [77], which leads to the T^2 correction to $D(T)/T$.

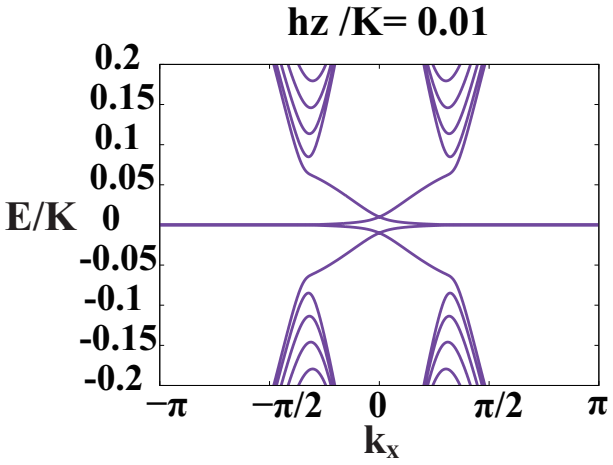


Figure 6.9: Majorana band structures in a magnetic field. For the parameter set $(h_z, \Delta, N, L_x) = (0.01, 0.05, 80, 1000)$[75].

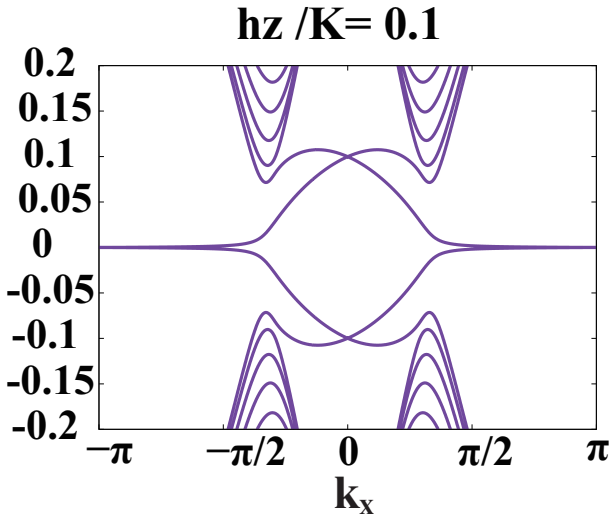


Figure 6.10: Majorana band structures in a magnetic field. For the parameter set $(h_z, \Delta, N, L_x) = (0.1, 0.05, 80, 1000)$[75].

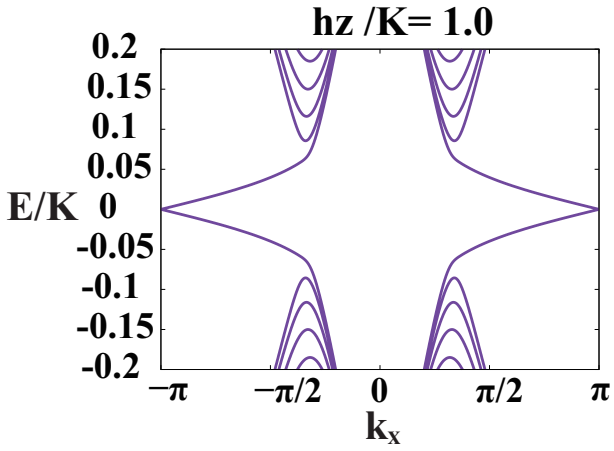


Figure 6.11: Majorana band structures in a magnetic field. For the parameter set $(h_z, \Delta, N, L_x) = (1.0, 0.05, 80, 1000)$[75].

6.5 Application for spintronics

In the previous section, we clarified that the dissipationless spin current generated by the spin Seebeck effects is a unique property of the Kitaev spin liquid, which possesses chiral Majorana edge states. Not only for the basic research, but the discovery of the dissipationless spin transport should also be the key to the direct application of the Kitaev spin liquid to spintronics technology. The application of the spin liquid other than the topological quantum computation is limited now, for example, [79]. Especially it has recently been pointed out that spin liquid states are applicable to spintronics [80]. In the spintronics field, the miniaturization of the devices is desired for the realization of high-speed and high-capacity information processing. However, conventional insulators such as ferromagnet and ferromagnet are hard to realize because, at the nanoscale, the magnon, Goldstone-mode is unstable. Thus, new careers need to be found, and as mentioned above, it has been pointed out that the spin liquids are suitable for nanoscale spintronics devices [80, 81, 82, 83, 84, 85, 86, 87, 88, 89, 90, 91]. It is reported that since quantum fluctuations stabilize the exotic states even on the atomic scale, fractionalized excitations characterizing spin liquids can indeed carry spin currents [80].

The Kitaev spin liquid is suitable for the miniaturization spintronics devices because the Kitaev spin liquid is not broken on the nanoscale. Moreover, in general, observing the spin Seebeck effect requires that the energy gap of the spin excitation is larger than the thermal excitation and that the correlations between spins are long-range. Interestingly the edge current flow, despite that the Kitaev spin liquid has a very short-range correlation length which is a constant lattice order in bulk (See Eq. (3.113)).

Finally, we note that, as seen in Fig. 6.6, even at very low temperatures $T/K \sim 0.001$, the magnitude of the Drude weight part of the spin Seebeck conductivity is roughly $\sim Ka\mu_{\rm B}/\hbar$ with K the Kitaev interaction, a a lattice constant, $\mu_{\rm B}$ the Bohr magneton. For α-$RuCl_3$ [23], $\sim Ka\mu_{\rm B}/\hbar \sim 1000\mu_{\rm B}$ $(m^{-1}\cdot s^{-1}\times\mu_{\rm B})$, which implies that the effect is much enhanced compared to conventional thermoelectric effects of electrons in semiconductors. The origin of the notable enhancement is attributed to two factors; one is the absence of the backward scattering in the chiral edge state, and the other one is the flatness of the edge Majorana band (see Fig. 6.9-6.11), i.e., the large energy-derivative of the density of states, which arises from the unpaired gauge-field Majorana fields at the edges. We stress that these factors are ubiquitous

features of the Kitaev's chiral spin liquid state.

Chapter 7

Nonreciprocal transport of Kitaev spin liquid

In this chapter, we consider the nonreciprocal thermal transport of the Majorana edge states induced by the Dzyaloshinskii-Moriya interaction to detect the Majorana fermion. We consider the Dzyaloshinskii-Moriya interaction at the edge of the system where as shown in Fig. 6.1, inversion symmetry is broken. The Majorana band structure changes from linear to non-linear and becomes asymmetric due to the Dzyaloshinskii-Moriya interaction at the edge. This change induces nonreciprocal thermal or spin transport. This change is expected to develop more experimental studies about the nonequilibrium steady state in the Kitaev materials.

The total Hamiltonian is given by,

$$\begin{aligned} \mathcal{H} &= \mathcal{H}_K + \mathcal{H}_{zeeman} + \mathcal{H}_{DM}, & (7.1) \\ \mathcal{H}_{DM} &= -\sum_{\langle mA,nB\rangle} \mathbf{D}_{mA,nB} \cdot (\mathbf{S}_{mA} \times \mathbf{S}_{nB}), & (7.2) \end{aligned}$$

where Dzyaloshinskii-Moriya interaction acts on the edges in the unit cell of this thesis shown in Fig. 7.1 and m, n are the indices for the unit cell, and A, B are the black site and the white site. Here we perform the perturbative calculations and consider the magnetic field and Dzyaloshinskii-Moriya interaction as the perturbation term. The effective Hamiltonian is given by

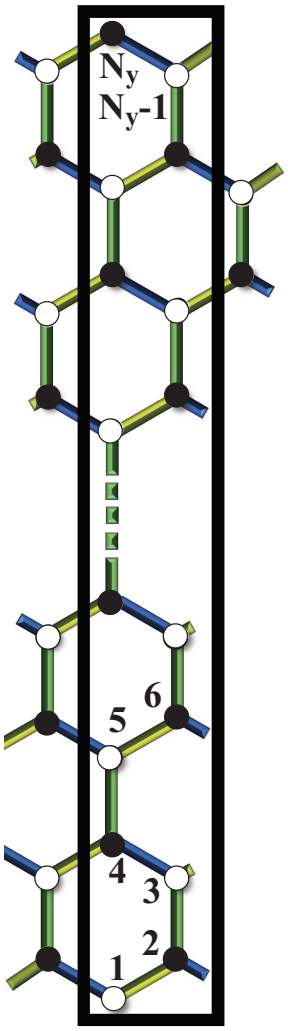


Figure 7.1: Unit cell of the system with open edges in the y direction.[75]

the Kitaev perturbation method [4],

$$\mathcal{H} = \mathcal{H}_K + \mathcal{H}^{(3)} - \sum_l (h_z S^z_{l,1} + h_z S^z_{l,N}) + \mathcal{H}^{(1)}, \tag{7.3}$$

$$=: \frac{1}{2} \sum_{(l,m),(l',n)} c_{l,m} A_{(l,m)(l',n)} c_{l',n}, \tag{7.4}$$

$$\mathcal{H}_K = -\sum_{\langle ij \rangle_\alpha} K_\alpha S^\alpha_i S^\alpha_j, \tag{7.5}$$

$$\mathcal{H}^{(3)} = -\Delta \sum_{i,j,k} S^x_i S^y_j S^z_k, \tag{7.6}$$

$$\mathcal{H}^{(1)} = \sum_{p=1,2,3,4} \sum_{\langle ij \rangle} i D_p c_i c_j + \sum_{p=5,6,7,8} \sum_{\langle ij \rangle} i D_p b^z_i c_j, \tag{7.7}$$

$$D_1 = D_3 = \frac{D(h_x - h_y)}{\Delta}, \tag{7.8}$$

$$D_2 = D_4 = \frac{D h_z}{\Delta}, \tag{7.9}$$

$$D_5 = -D_7 = \frac{2D h_x}{\Delta}, \tag{7.10}$$

$$D_6 = -D_8 = -\frac{2D h_y}{\Delta}, \tag{7.11}$$

$$\Delta \sim \frac{h_x h_y h_z}{K^2}, \tag{7.12}$$

where we assume the magnitude of the Dzyaloshinskii-Moriya interaction to be the same, $D_x = D_y = D_z$ and b^z_j in Eq. (7.7) is the gauge field Majorana which exists at the edges shown in Fig. 6.1, and D is the Dzyaloshinskii-Moriya interaction acting at the top(bottom) edge shown in Fig. 6.1. We show the processes of the perturbations in detail.

First, we show the case of the top edge. Fig. 7.2 show that the operation of $D\sigma^y_1\sigma^z_2$ and $h_x\sigma^x_4$ are acting on a vortex-free initial state, and the final state is the vortex-free state. We denote flips of the Z_2 gauge fields on the bonds by orange color, and the effective Hamiltonian is given by,

$$\mathcal{H}^{D1}_1 = \sum i \frac{D h_x}{\Delta} c_1 c_4. \tag{7.13}$$

Fig. 7.3 show that the operation of $D\sigma^z_2\sigma^y_3$ and $h_x\sigma^x_1$ are acting on a vortex-free initial state, and the final state is the vortex-free state. The

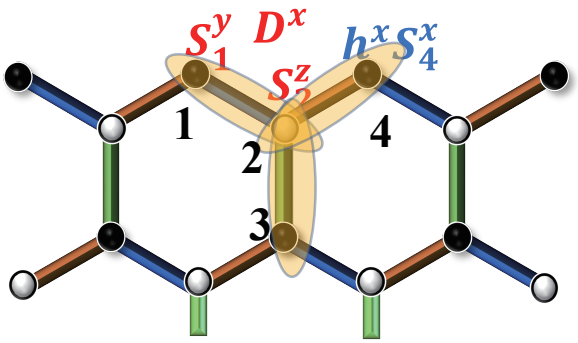


Figure 7.2:

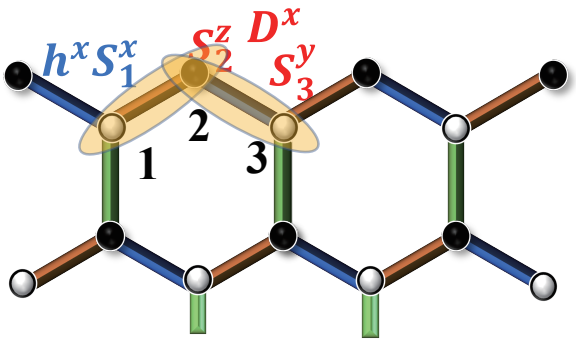


Figure 7.3:

effective Hamiltonian is given by,

$$\mathcal{H}_2^{D1} = \sum -i\frac{Dh_x}{\Delta}c_3c_1. \tag{7.14}$$

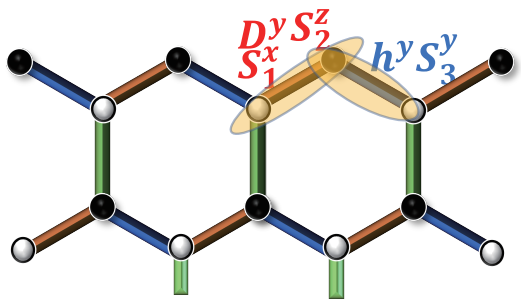


Figure 7.4:

Fig. 7.4 show that the operation of $D\sigma_1^x\sigma_2^z$ and $h_y\sigma_3^y$ are acting on a vortex-free initial state, and the final state is the vortex-free state. The effective Hamiltonian is given by,

$$\mathcal{H}_3^{D1} = \sum -i\frac{Dh_y}{\Delta}c_1c_3. \tag{7.15}$$

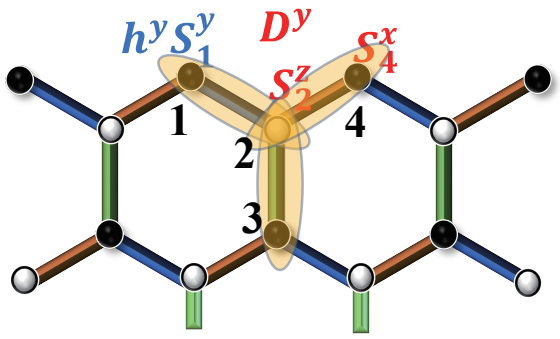


Figure 7.5:

Fig. 7.5 show that the operation of $D\sigma_2^z\sigma_4^x$ and $h_y\sigma_1^y$ are acting on a vortex-free initial state, and the final state is the vortex-free state. The effective

Hamiltonian is given by,

$$\mathcal{H}_4^{D1} = \sum i\frac{Dh_y}{\Delta}c_4c_1. \tag{7.16}$$

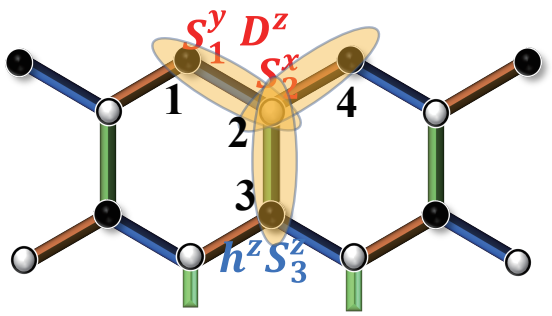


Figure 7.6:

Fig. 7.6 show that the operation of $D\sigma_1^y\sigma_2^x$ and $h_z\sigma_3^z$ are acting on a vortex-free initial state, and the final state is the vortex-free state. The effective Hamiltonian is given by,

$$\mathcal{H}_1^{D2} = \sum i\frac{Dh_z}{\Delta}c_1c_3. \tag{7.17}$$

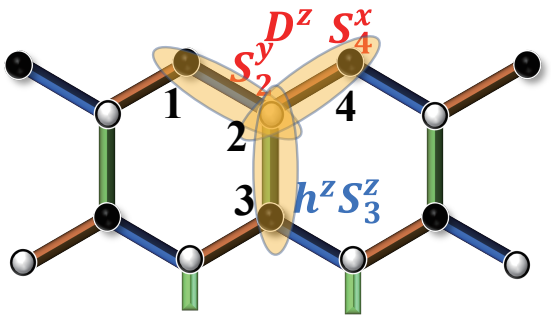


Figure 7.7:

Fig. 7.7 show that the operation of $D\sigma_2^y\sigma_4^x$ and $h_z\sigma_3^z$ are acting on a vortex-free initial state, and the final state is the vortex-free state. The effective Hamiltonian is given by,

$$\mathcal{H}_2^{D2} = \sum i\frac{Dh_z}{\Delta}c_4c_3. \tag{7.18}$$

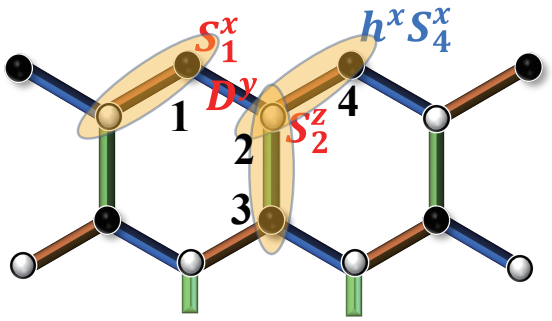


Figure 7.8:

Fig. 7.8 show that the operation of $D\sigma_1^x\sigma_2^z$ and $h_x\sigma_4^x$ are acting on a vortex-free initial state, and the final state is the vortex-free state. The effective Hamiltonian is given by,

$$\mathcal{H}_1^{D5} = \sum i\frac{Dh_x}{\Delta}b_1^zc_4. \tag{7.19}$$

Fig. 7.9 show that the operation of $D\sigma_2^z\sigma_4^x$ and $h_x\sigma_1^x$ are acting on a vortex-free initial state, and the final state is the vortex-free state. The effective Hamiltonian is given by,

$$\mathcal{H}_2^{D5} = \sum i\frac{Dh_x}{\Delta}b_1^zc_4. \tag{7.20}$$

Fig. 7.10 show that the operation of $D\sigma_2^z\sigma_4^y$ and $h_y\sigma_1^y$ are acting on a vortex-free initial state, and the final state is the vortex-free state. The effective Hamiltonian is given by,

$$\mathcal{H}_1^{D6} = \sum -i\frac{Dh_y}{\Delta}b_4^zc_1. \tag{7.21}$$

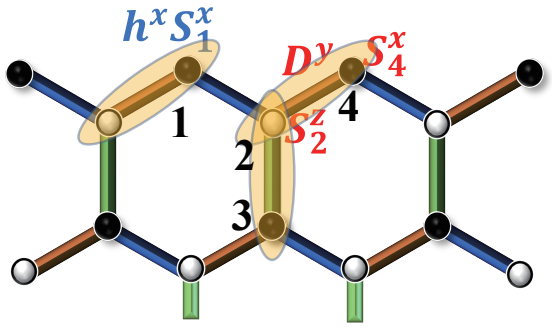


Figure 7.9:

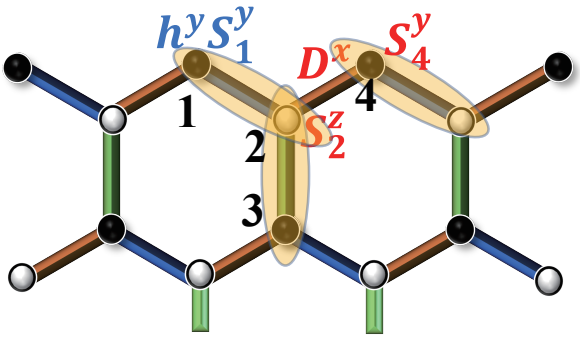


Figure 7.10:

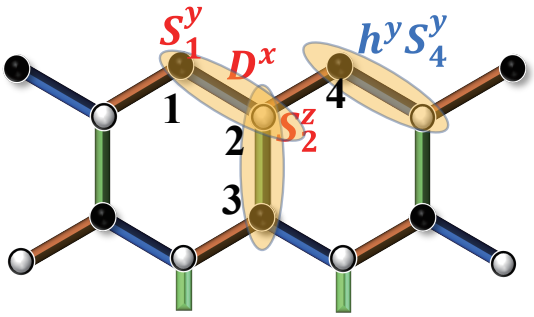


Figure 7.11:

Fig. 7.11 show that the operation of $D\sigma_1^y\sigma_2^z$ and $h_y\sigma_4^y$ are acting on a vortex-free initial state, and the final state is the vortex-free state. The effective Hamiltonian is given by,

$$\mathcal{H}_2^{D6} = \sum -i\frac{Dh_y}{\Delta}b_4^z c_1. \tag{7.22}$$

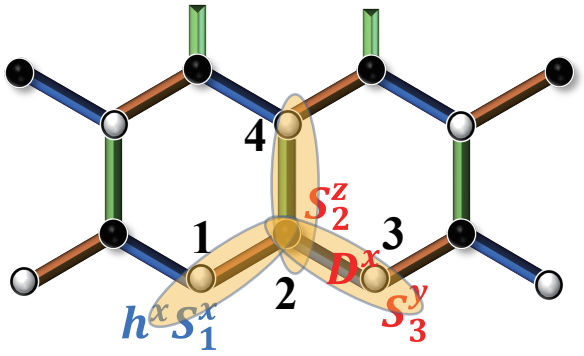


Figure 7.12:

Next, we show the case of the bottom edge. Fig. 7.12 show that the operation of $D\sigma_2^z\sigma_3^y$ and $h_x\sigma_1^x$ are acting on a vortex-free initial state, and the final state is the vortex-free state. We denote flips of the Z_2 gauge fields on the bonds by orange color, and the effective Hamiltonian is given by,

$$\mathcal{H}_1^{D3} = \sum -i\frac{Dh_x}{\Delta}c_3 c_1. \tag{7.23}$$

Fig. 7.13 show that the operation of $D\sigma_1^y\sigma_2^z$ and $h_x\sigma_3^x$ are acting on a vortex-free initial state, and the final state is the vortex-free state. The effective Hamiltonian is given by,

$$\mathcal{H}_2^{D3} = \sum i\frac{Dh_y}{\Delta}c_1 c_3. \tag{7.24}$$

Fig. 7.14 show that the operation of $D\sigma_2^z\sigma_3^x$ and $h_y\sigma_1^y$ are acting on a vortex-free initial state, and the final state is the vortex-free state. The effective Hamiltonian is given by,

$$\mathcal{H}_3^{D3} = \sum i\frac{Dh_y}{\Delta}c_3 c_1. \tag{7.25}$$

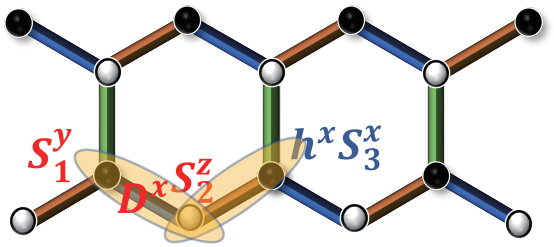


Figure 7.13:

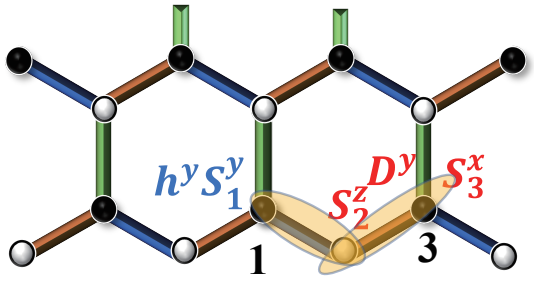


Figure 7.14:

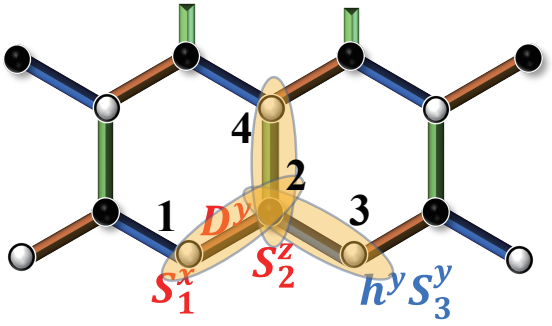


Figure 7.15:

Fig. 7.15 show that the operation of $D\sigma_1^x\sigma_2^z$ and $h_y\sigma_3^y$ are acting on a vortex-free initial state, and the final state is the vortex-free state. The effective Hamiltonian is given by,

$$\mathcal{H}_4^{D3} = \sum -i\frac{Dh_y}{\Delta}c_1c_3. \tag{7.26}$$

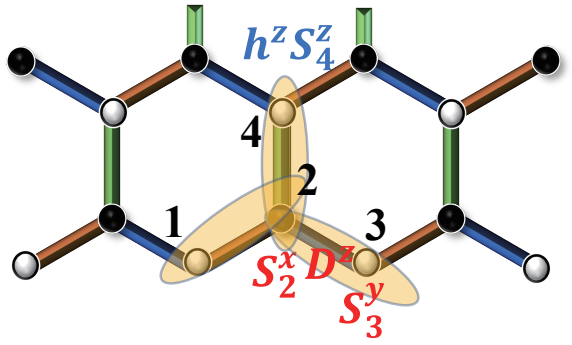


Figure 7.16:

Fig. 7.16 show that the operation of $D\sigma_2^x\sigma_3^y$ and $h_z\sigma_4^z$ are acting on a vortex-free initial state, and the final state is the vortex-free state. The effective Hamiltonian is given by,

$$\mathcal{H}_1^{D4} = \sum -i\frac{Dh_z}{\Delta}c_3c_4. \tag{7.27}$$

Fig. 7.17 show that the operation of $D\sigma_1^x\sigma_2^y$ and $h_z\sigma_4^z$ are acting on a vortex-free initial state, and the final state is the vortex-free state. The effective Hamiltonian is given by,

$$\mathcal{H}_2^{D4} = \sum -i\frac{Dh_z}{\Delta}c_1c_4. \tag{7.28}$$

Fig. 7.18 show that the operation of $D\sigma_2^z\sigma_3^x$ and $h_x\sigma_1^x$ are acting on a vortex-free initial state, and the final state is the vortex-free state. The effective Hamiltonian is given by,

$$\mathcal{H}_1^{D7} = \sum -i\frac{Dh_x}{\Delta}b_3^zc_1. \tag{7.29}$$

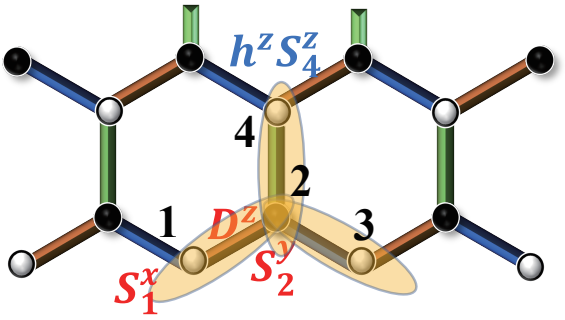


Figure 7.17:

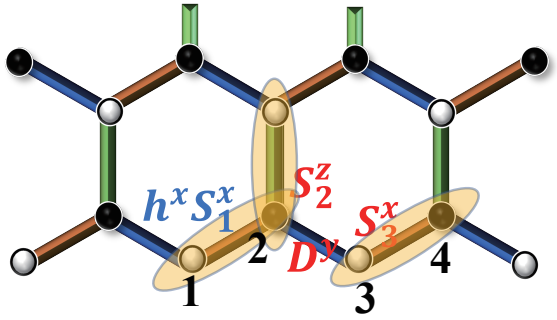


Figure 7.18:

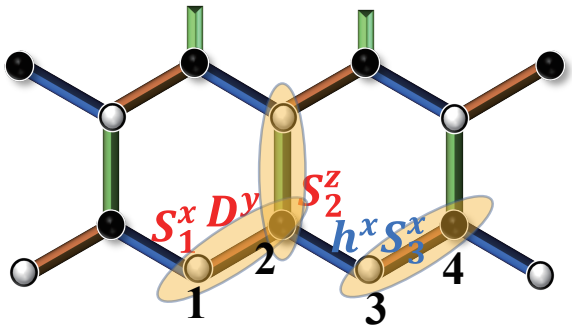


Figure 7.19:

Fig. 7.19 show that the operation of $D\sigma_1^x\sigma_2^z$ and $h_x\sigma_3^x$ are acting on a vortex-free initial state, and the final state is the vortex-free state. The effective Hamiltonian is given by,

$$\mathcal{H}_2^{D7} = \sum -i\frac{Dh_x}{\Delta}b_3^z c_1. \tag{7.30}$$

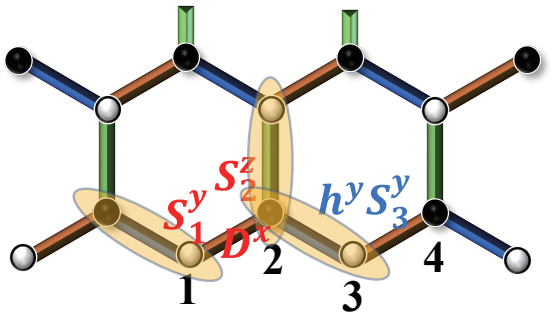


Figure 7.20:

Fig. 7.20 show that the operation of $D\sigma_1^y\sigma_2^z$ and $h_y\sigma_3^y$ are acting on a vortex-free initial state, and the final state is the vortex-free state. The effective Hamiltonian is given by,

$$\mathcal{H}_1^{D8} = \sum i\frac{Dh_y}{\Delta}b_1^z c_3. \tag{7.31}$$

Fig. 7.21 show that the operation of $D\sigma_2^z\sigma_3^y$ and $h_y\sigma_1^y$ are acting on a vortex-free initial state, and the final state is the vortex-free state. The effective Hamiltonian is given by,

$$\mathcal{H}_2^{D8} = \sum i\frac{Dh_y}{\Delta}b_1^z c_3. \tag{7.32}$$

In summary, we show the hopping term in Fig. 7.22 of the top edge and Fig. 7.23 about the bottom edge.

Next, we show the Majorana band structure changing depending on the various values of D_{1-8}. Due to the Dzyaloshinskii-Moriya interaction acting at the edges, the Majorana band structure changes non-linear shown in

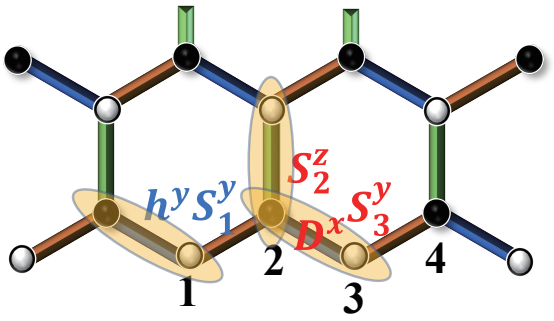


Figure 7.21:

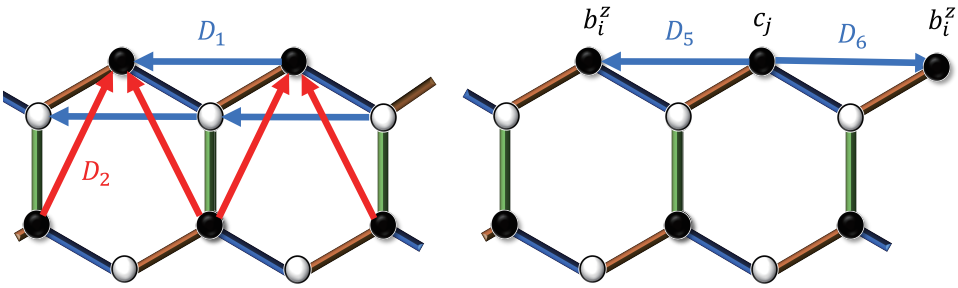


Figure 7.22: top edge

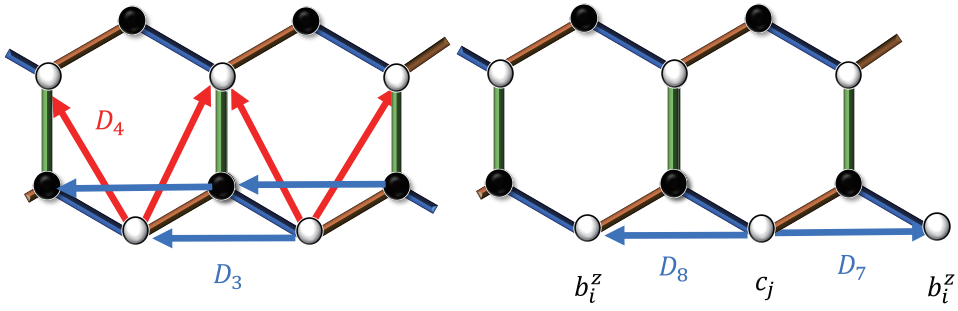


Figure 7.23: bottom edge

Fig. 7.24 at D_1=D_3=1.0 and Fig. 7.26 at D_5=1.0, D_7=-1.0 and Fig. 7.27 at D_6=-1.0, D_8=1.0 at the magnetic field $h_z/K = 1.0$ and the Majorana gap $\kappa/K = 1.0$. These horizontal hoppings break the inversion symmetry, and the Majorana band structure changes to non-linear. However, the Majorana bands do not change from linear for the diagonal hopping case of D_2=D_4=1.0 shown in Fig. 7.25. Asymmetric bands enable the observation of nonreciprocal responses because of the group velocities difference. It is also possible to observe nonreciprocal phenomena not only in thermal transport but also in spin transport. It is an interesting future issue to investigate these nonreciprocal transport phenomena.

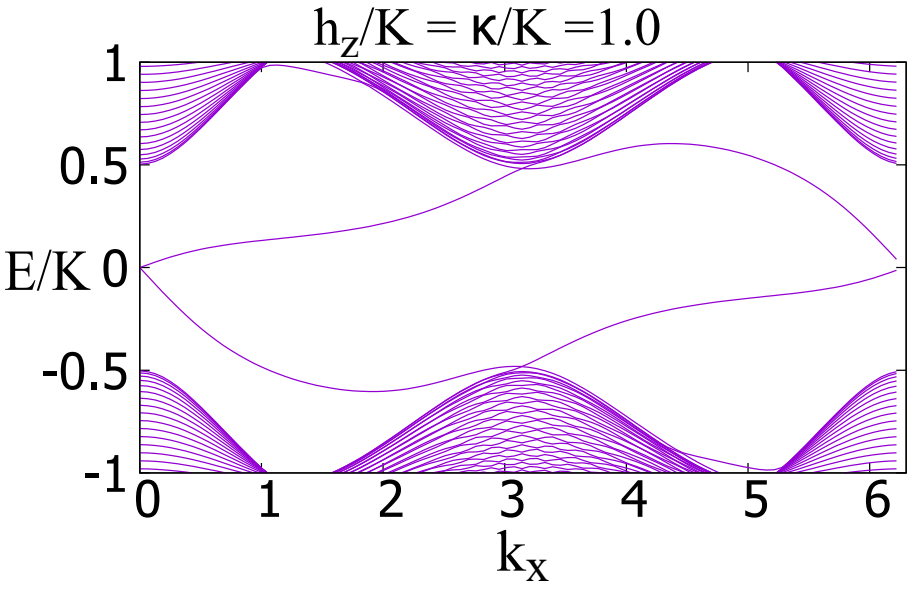


Figure 7.24: The energy spectrum of Majorana particles in the case of D_1=D_3=1.0.

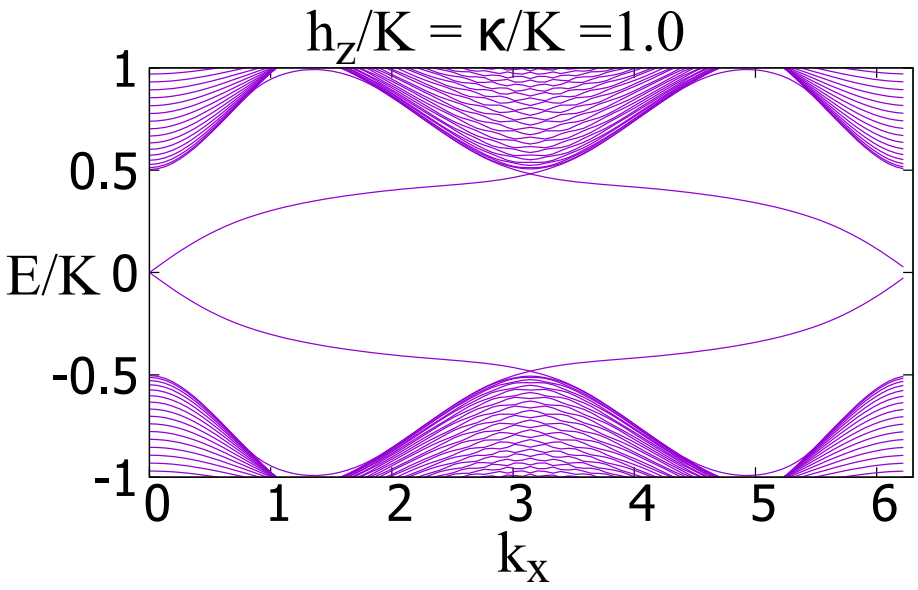


Figure 7.25: The energy spectrum of Majorana particles in the case of D_2=D_4=1.0.

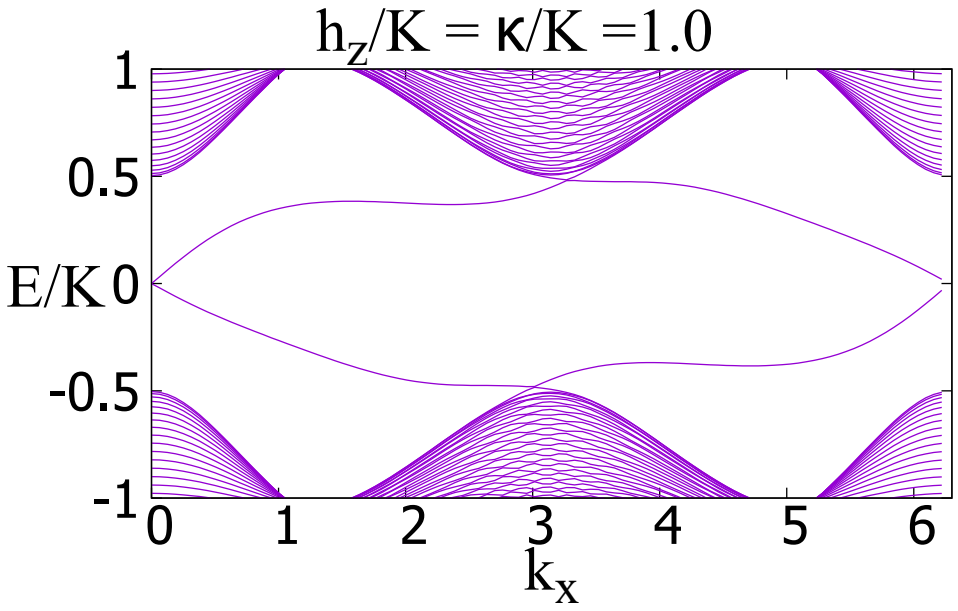


Figure 7.26: The energy spectrum of Majorana particles in the case of D_5=1.0,D_7=-1.0.

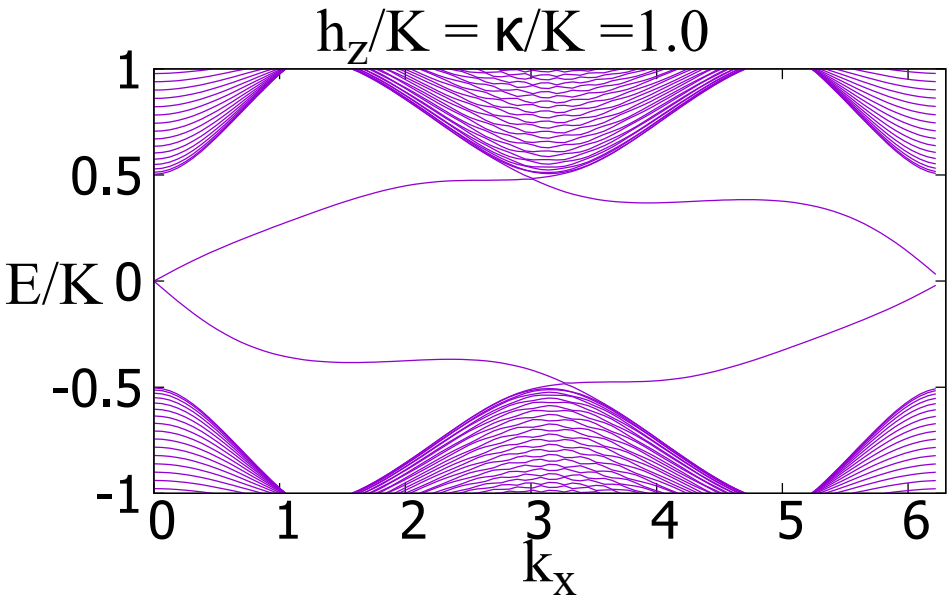


Figure 7.27: The energy spectrum of Majorana particles in the case of D_6=-1.0,D_8=1.0.

Chapter 8

Conclusion

As mentioned in the overview of this thesis, the purposes of this thesis are to investigate the effects of Majorana edge states in Kitaev magnets, to propose experiments that provide conclusive evidence for Majorana fermions, and to propose new applications of the Kitaev spin liquids. We proposed the spin Seebeck effect in chapter 6 to investigate the edge effect on spin transport phenomena. From the results obtained in chapter 6, we propose an experiment that potentially detects Majorana fermions in α-$RuCl_3$, the existence of which is currently still under debate. The dissipationless spin current generated by the spin Seebeck effect is a unique property of the Kitaev spin liquid which possesses chiral Majorana edge states. The universal temperature scaling of the Drude weight in the spin Seebeck effect should be a definite signature of chiral Majorana edge states, because we can expect that the universal scaling is stable with respect to various extrinsic perturbations, such as disorder and phonons, provided that the roughness of the edge is sufficiently weak. In the case that the edge is a strongly random admixture of a zigzag type and an armchair type, the spin current is suppressed. However, it is expected that, even in such situations, the spin current does not vanish entirely as long as a magnetic field h_z is applied. Although disorder due to impurities in real systems may broaden the Drude peak, the total weight is not affected because of the chiral character of the edge states. These results contrast the case without a bulk energy gap, where the Drude weight is substantially suppressed by weak randomness [92]. Not only for the basic research, but the discovery of the dissipationless spin transport should also be the key to the direct application of the Kitaev spin liquid to spintronics technology. Moreover, in chapter 7, we proposed the nonreciprocal transport

phenomena induced by the Dzyaloshinskii-Moriya interaction acting at the edges. The Majorana band structure changes from linear to non-linear and becomes asymmetric, which enables nonreciprocal transport. This discovery develops the experiments of the nonreciprocal transport and leads to an understanding of the nature of the Majorana edge state of the spin liquid state.

Acknowledgement

I thank Satoshi Fujimoto, Masahiko Yamada, Takeshi Mizushima, Atushi Tsuruta, Takumi Sannno, Masahiro Takahashi, Taiki Matsushita, Shinya Matuba, all other laboratory members and Manato Fujimoto, Tomohiro Yamazaki and my parents. We thank Yuji Matsuda, Takahiro Morimoto, and Takasada Shibauchi, Yuichi Kasahara, Martin. Klanjsek, Ken. Shiozaki for valuable discussions. Over the past three years in my Ph.D. course, I have been financially supported by a Japan Society for the Promotion of Science Fellowship for Young Scientists. I sincerely thank this financial support.

Publication

Refereed papers

- D. Takikawa, M. G. Yamada, and S. Fujimoto, Dissipationless spin current generation in a Kitaev chiral spin liquid, Physical Review B 105, 115137 (2022).

- D. Takikawa and S. Fujimoto, Impact of off-diagonal exchange inter- actions on the Kitaev spin-liquid state of α-$RuCl_3$, Physical Review B 99, 224409 (2019).

- D. Takikawa and S. Fujimoto, Topological phase transition to Abelian anyon phases due to off-diagonal exchange interaction in the Kitaev spin liquid state, Physical Review B 102, 174414 (2020).

- M. O. Takahashi, M. G. Yamada, D. Takikawa, T. Mizushima, and S. Fujimoto, Topological nematic phase transition in Kitaev magnets under applied magnetic fields, Physical Review Research 3, 023189 (2021).

Bibliography

[1] Y. Kasahara, T. Ohnishi, Y. Mizukami, O. Tanaka, S. Ma, K. Sugii, N. Kurita, H. Tanaka, J. Nasu, Y. Motome, *et al.*, *Majorana quantization and half-integer thermal quantum Hall effect in a Kitaev spin liquid,* Nature **559**, 227 (2018).

[2] M. Yamashita, J. Gouchi, Y. Uwatoko, N. Kurita, and H. Tanaka, *Sample dependence of half-integer quantized thermal Hall effect in the Kitaev spin-liquid candidate* $\alpha-\mathrm{RuCl_3}$*,* Phys. Rev. B **102**, 220404 (2020).

[3] T. Yokoi, S. Ma, Y. Kasahara, S. Kasahara, T. Shibauchi, N. Kurita, H. Tanaka, J. Nasu, Y. Motome, C. Hickey, S. Trebst, and Y. Matsuda, *Half-integer quantized anomalous thermal Hall effect in the Kitaev material candidate* α*-*$RuCl_3$*,* Science **373**, 568 (2021), https://www.science.org/doi/pdf/10.1126/science.aay5551 .

[4] A. Kitaev, *Anyons in an exactly solved model and beyond,* Annals of Physics **321**, 2 (2006), january Special Issue.

[5] P. Anderson, *Resonating valence bonds: A new kind of insulator?* Materials Research Bulletin **8**, 153 (1973).

[6] G. Baskaran, Z. Zou, and P. Anderson, *The resonating valence bond state and high-Tc superconductivity A mean field theory,* Solid State Communications **63**, 973 (1987).

[7] V. Kalmeyer and R. B. Laughlin, *Equivalence of the resonating-valence-bond and fractional quantum Hall states,* Phys. Rev. Lett. **59**, 2095 (1987).

[8] X. G. Wen, *Vacuum degeneracy of chiral spin states in compactified space,* Phys. Rev. B **40**, 7387 (1989).

[9] A. Kitaev, *Fault-tolerant quantum computation by anyons,* Annals of Physics **303**, 2 (2003).

[10] G. Baskaran, S. Mandal, and R. Shankar, *Exact Results for Spin Dynamics and Fractionalization in the Kitaev Model,* Phys. Rev. Lett. **98**, 247201 (2007).

[11] G. Jackeli and G. Khaliullin, *Mott Insulators in the Strong Spin-Orbit Coupling Limit: From Heisenberg to a Quantum Compass and Kitaev Models,* Phys. Rev. Lett. **102**, 017205 (2009).

[12] X. Liu, T. Berlijn, W.-G. Yin, W. Ku, A. Tsvelik, Y.-J. Kim, H. Gretarsson, Y. Singh, P. Gegenwart, and J. P. Hill, *Long-range magnetic ordering in Na_2IrO_3,* Phys. Rev. B **83**, 220403 (2011).

[13] F. Ye, S. Chi, H. Cao, B. C. Chakoumakos, J. A. Fernandez-Baca, R. Custelcean, T. F. Qi, O. B. Korneta, and G. Cao, *Direct evidence of a zigzag spin-chain structure in the honeycomb lattice: A neutron and x-ray diffraction investigation of single-crystal Na_2IrO_3,* Phys. Rev. B **85**, 180403 (2012).

[14] J. G. Rau, E. K.-H. Lee, and H.-Y. Kee, *Generic Spin Model for the Honeycomb Iridates beyond the Kitaev Limit,* Phys. Rev. Lett. **112**, 077204 (2014).

[15] J. Knolle, D. L. Kovrizhin, J. T. Chalker, and R. Moessner, *Dynamics of a Two-Dimensional Quantum Spin Liquid: Signatures of Emergent Majorana Fermions and Fluxes,* Phys. Rev. Lett. **112**, 207203 (2014).

[16] M. Hermanns and S. Trebst, *Quantum spin liquid with a Majorana Fermi surface on the three-dimensional hyperoctagon lattice,* Phys. Rev. B **89**, 235102 (2014).

[17] K. W. Plumb, J. P. Clancy, L. J. Sandilands, V. V. Shankar, Y. F. Hu, K. S. Burch, H.-Y. Kee, and Y.-J. Kim, *$\alpha-RuCl_3$: A spin-orbit assisted Mott insulator on a honeycomb lattice,* Phys. Rev. B **90**, 041112 (2014).

[18] Y. Yamaji, Y. Nomura, M. Kurita, R. Arita, and M. Imada, *First-Principles Study of the Honeycomb-Lattice Iridates* Na_2IrO_3 *in the Presence of Strong Spin-Orbit Interaction and Electron Correlations,* Phys. Rev. Lett. **113**, 107201 (2014).

[19] Y. Kubota, H. Tanaka, T. Ono, Y. Narumi, and K. Kindo, *Successive magnetic phase transitions in $\alpha-\mathrm{RuCl_3}$: XY-like frustrated magnet on the honeycomb lattice,* Phys. Rev. B **91**, 094422 (2015).

[20] J. Nasu, M. Udagawa, and Y. Motome, *Thermal fractionalization of quantum spins in a Kitaev model: Temperature-linear specific heat and coherent transport of Majorana fermions,* Phys. Rev. B **92**, 115122 (2015).

[21] M. Hermanns, S. Trebst, and A. Rosch, *Spin-Peierls Instability of Three-Dimensional Spin Liquids with Majorana Fermi Surfaces,* Phys. Rev. Lett. **115**, 177205 (2015).

[22] R. D. Johnson, S. C. Williams, A. A. Haghighirad, J. Singleton, V. Zapf, P. Manuel, I. I. Mazin, Y. Li, H. O. Jeschke, R. Valentí, and R. Coldea, *Monoclinic crystal structure of $\alpha-\mathrm{RuCl_3}$ and the zigzag antiferromagnetic ground state,* Phys. Rev. B **92**, 235119 (2015).

[23] A. Banerjee, C. A. Bridges, J. Q. Yan, A. A. Aczel, L. Li, M. B. Stone, G. E. Granroth, M. D. Lumsden, Y. Yiu, J. Knolle, S. Bhattacharjee, D. L. Kovrizhin, R. Moessner, D. A. Tennant, D. G. Mandrus, and S. E. Nagler, *Proximate Kitaev quantum spin liquid behaviour in a honeycomb magnet,* Nature Materials **15**, 733 (2016).

[24] H. B. Cao, A. Banerjee, J.-Q. Yan, C. A. Bridges, M. D. Lumsden, D. G. Mandrus, D. A. Tennant, B. C. Chakoumakos, and S. E. Nagler, *Low-temperature crystal and magnetic structure of $\alpha-\mathrm{RuCl_3}$,* Phys. Rev. B **93**, 134423 (2016).

[25] S. C. Williams, R. D. Johnson, F. Freund, S. Choi, A. Jesche, I. Kimchi, S. Manni, A. Bombardi, P. Manuel, P. Gegenwart, and R. Coldea, *Incommensurate counterrotating magnetic order stabilized by Kitaev interactions in the layered honeycomb $\alpha-\mathrm{Li_2IrO_3}$,* Phys. Rev. B **93**, 195158 (2016).

[26] X.-Y. Song, Y.-Z. You, and L. Balents, *Low-Energy Spin Dynamics of the Honeycomb Spin Liquid Beyond the Kitaev Limit,* Phys. Rev. Lett. **117**, 037209 (2016).

[27] S.-H. Baek, S.-H. Do, K.-Y. Choi, Y. S. Kwon, A. U. B. Wolter, S. Nishimoto, J. van den Brink, and B. Büchner, *Evidence for a Field-Induced Quantum Spin Liquid in* α-$RuCl_3$, Phys. Rev. Lett. **119**, 037201 (2017).

[28] M. G. Yamada, H. Fujita, and M. Oshikawa, *Designing Kitaev Spin Liquids in Metal-Organic Frameworks,* Phys. Rev. Lett. **119**, 057202 (2017).

[29] J. Nasu, J. Yoshitake, and Y. Motome, *Thermal Transport in the Kitaev Model,* Phys. Rev. Lett. **119**, 127204 (2017).

[30] M. G. Yamada, V. Dwivedi, and M. Hermanns, *Crystalline Kitaev spin liquids,* Phys. Rev. B **96**, 155107 (2017).

[31] J. Zheng, K. Ran, T. Li, J. Wang, P. Wang, B. Liu, Z.-X. Liu, B. Normand, J. Wen, and W. Yu, *Gapless Spin Excitations in the Field-Induced Quantum Spin Liquid Phase of* $\alpha-RuCl_3$, Phys. Rev. Lett. **119**, 227208 (2017).

[32] R. Hentrich, A. U. B. Wolter, X. Zotos, W. Brenig, D. Nowak, A. Isaeva, T. Doert, A. Banerjee, P. Lampen-Kelley, D. G. Mandrus, S. E. Nagler, J. Sears, Y.-J. Kim, B. Büchner, and C. Hess, *Unusual Phonon Heat Transport in* $\alpha-RuCl_3$*: Strong Spin-Phonon Scattering and Field-Induced Spin Gap,* Phys. Rev. Lett. **120**, 117204 (2018).

[33] N. Janša, A. Zorko, M. Gomilšek, M. Pregelj, K. W. Krämer, D. Biner, A. Biffin, C. Rüegg, and M. Klanjšek, *Observation of two types of fractional excitation in the Kitaev honeycomb magnet,* Nature physics **14**, 786 (2018).

[34] Z. Zhu, I. Kimchi, D. N. Sheng, and L. Fu, *Robust non-Abelian spin liquid and a possible intermediate phase in the antiferromagnetic Kitaev model with magnetic field,* Phys. Rev. B **97**, 241110 (2018).

[35] Y. Vinkler-Aviv and A. Rosch, *Approximately Quantized Thermal Hall Effect of Chiral Liquids Coupled to Phonons,* Phys. Rev. X **8**, 031032 (2018).

[36] M. Ye, G. B. Halász, L. Savary, and L. Balents, *Quantization of the Thermal Hall Conductivity at Small Hall Angles,* Phys. Rev. Lett. **121**, 147201 (2018).

[37] M. Udagawa, *Vison-Majorana complex zero-energy resonance in the Kitaev spin liquid,* Phys. Rev. B **98**, 220404 (2018).

[38] J. Rusnačko, D. Gotfryd, and J. c. v. Chaloupka, *Kitaev-like honeycomb magnets: Global phase behavior and emergent effective models,* Phys. Rev. B **99**, 064425 (2019).

[39] J. S. Gordon, A. Catuneanu, E. S. Sørensen, and H.-Y. Kee, *Theory of the field-revealed Kitaev spin liquid,* Nature communications **10**, 2470 (2019).

[40] S.-S. Zhang, Z. Wang, G. B. Halász, and C. D. Batista, *Vison Crystals in an Extended Kitaev Model on the Honeycomb Lattice,* Phys. Rev. Lett. **123**, 057201 (2019).

[41] J. Nasu and Y. Motome, *Nonequilibrium Majorana dynamics by quenching a magnetic field in Kitaev spin liquids,* Phys. Rev. Research **1**, 033007 (2019).

[42] M. G. Yamada, *Anderson–Kitaev spin liquid,* npj Quantum Materials **5**, 82 (2020).

[43] M. G. Yamada and S. Fujimoto, *Electric Probe for the Toric Code Phase in Kitaev Materials through the Hyperfine Interaction,* Phys. Rev. Lett. **127**, 047201 (2021).

[44] M. G. Yamada, *Topological Z_2 invariant in Kitaev spin liquids: Classification of gapped spin liquids beyond projective symmetry group,* Phys. Rev. Research **3**, L012001 (2021).

[45] M. O. Takahashi, M. G. Yamada, D. Takikawa, T. Mizushima, and S. Fujimoto, *Topological nematic phase transition in Kitaev magnets under applied magnetic fields,* Phys. Rev. Research **3**, 023189 (2021).

[46] M. H. Freedman, M. Larsen, and Z. Wang, *A modular functor which is universal¶ for quantum computation,* Communications in Mathematical Physics **227**, 605 (2002).

[47] A. T. Bolukbasi and J. Vala, *Rigorous calculations of non-Abelian statistics in the Kitaev honeycomb model,* New Journal of Physics **14**, 045007 (2012).

[48] E. H. Lieb, *Flux Phase of the Half-Filled Band,* Phys. Rev. Lett. **73**, 2158 (1994).

[49] H. Nielsen and M. Ninomiya, *Absence of neutrinos on a lattice: (I). Proof by homotopy theory,* Nuclear Physics B **185**, 20 (1981).

[50] J. R. Wootton, V. Lahtinen, and J. K. Pachos, *Universal quantum computation with a non-Abelian topological memory,* in *Workshop on Quantum Computation, Communication, and Cryptography* (Springer, 2009) pp. 56–65.

[51] J. K. Pachos, *Introduction to topological quantum computation* (Cambridge University Press, 2012).

[52] D. Takikawa and S. Fujimoto, *Impact of off-diagonal exchange interactions on the Kitaev spin-liquid state of* $\alpha-\mathrm{RuCl_3}$*,* Phys. Rev. B **99**, 224409 (2019).

[53] D. Takikawa and S. Fujimoto, *Topological phase transition to Abelian anyon phases due to off-diagonal exchange interaction in the Kitaev spin liquid state,* Phys. Rev. B **102**, 174414 (2020).

[54] H. Sumiyoshi and S. Fujimoto, *Quantum Thermal Hall Effect in a Time-Reversal-Symmetry-Broken Topological Superconductor in Two Dimensions: Approach from Bulk Calculations,* Journal of the Physical Society of Japan **82**, 023602 (2013), https://doi.org/10.7566/JPSJ.82.023602 .

[55] N. Read and D. Green, *Paired states of fermions in two dimensions with breaking of parity and time-reversal symmetries and the fractional quantum Hall effect,* Phys. Rev. B **61**, 10267 (2000).

[56] K. Nomura, S. Ryu, A. Furusaki, and N. Nagaosa, *Cross-Correlated Responses of Topological Superconductors and Superfluids,* Phys. Rev. Lett. **108**, 026802 (2012).

[57] daichi hirobe, *Spin and Heat Transport in Spin Liquids*, Ph.D. thesis, tohoku Univ. (2017).

[58] H.-S. Kim and H.-Y. Kee, *Crystal structure and magnetism in* α*-*$RuCl_3$*: An ab initio study,* Phys. Rev. B **93**, 155143 (2016).

[59] T. Okubo, K. Shinjo, Y. Yamaji, N. Kawashima, S. Sota, T. Tohyama, and M. Imada, *Ground-state properties of* Na_2IrO_3 *determined from an ab initio Hamiltonian and its extensions containing Kitaev and extended Heisenberg interactions,* Phys. Rev. B **96**, 054434 (2017).

[60] G. Jackeli and G. Khaliullin, *Mott Insulators in the Strong Spin-Orbit Coupling Limit: From Heisenberg to a Quantum Compass and Kitaev Models,* Phys. Rev. Lett. **102**, 017205 (2009).

[61] Y. Motome and J. Nasu, *Hunting Majorana Fermions in Kitaev Magnets,* Journal of the Physical Society of Japan **89**, 012002 (2020), https://doi.org/10.7566/JPSJ.89.012002 .

[62] J. G. Rau, E. K.-H. Lee, and H.-Y. Kee, *Generic Spin Model for the Honeycomb Iridates beyond the Kitaev Limit,* Phys. Rev. Lett. **112**, 077204 (2014).

[63] O. Tanaka, Y. Mizukami, R. Harasawa, K. Hashimoto, K. Hwang, N. Kurita, H. Tanaka, S. Fujimoto, Y. Matsuda, E.-G. Moon, *et al.*, *Thermodynamic evidence for a field-angle-dependent Majorana gap in a Kitaev spin liquid,* Nature Physics **18**, 429 (2022).

[64] Y. Kubota, H. Tanaka, T. Ono, Y. Narumi, and K. Kindo, *Successive magnetic phase transitions in* $\alpha - RuCl_3$*: XY-like frustrated magnet on the honeycomb lattice,* Phys. Rev. B **91**, 094422 (2015).

[65] J. A. Sears, Y. Zhao, Z. Xu, J. W. Lynn, and Y.-J. Kim, *Phase diagram of* $\alpha - RuCl_3$ *in an in-plane magnetic field,* Phys. Rev. B **95**, 180411 (2017).

[66] A. U. B. Wolter, L. T. Corredor, L. Janssen, K. Nenkov, S. Schönecker, S.-H. Do, K.-Y. Choi, R. Albrecht, J. Hunger, T. Doert, M. Vojta, and B. Büchner, *Field-induced quantum criticality in the Kitaev system* $\alpha - RuCl_3$*,* Phys. Rev. B **96**, 041405 (2017).

[67] S. Widmann, V. Tsurkan, D. A. Prishchenko, V. G. Mazurenko, A. A. Tsirlin, and A. Loidl, *Thermodynamic evidence of fractionalized excitations in* $\alpha - RuCl_3$*,* Phys. Rev. B **99**, 094415 (2019).

[68] J. Knolle, D. L. Kovrizhin, J. T. Chalker, and R. Moessner, *Dynamics of fractionalization in quantum spin liquids,* Phys. Rev. B **92**, 115127 (2015).

[69] J. Knolle, G.-W. Chern, D. L. Kovrizhin, R. Moessner, and N. B. Perkins, *Raman Scattering Signatures of Kitaev Spin Liquids in A_2IrO_3 Iridates with $A =$ Na or Li,* Phys. Rev. Lett. **113**, 187201 (2014).

[70] L. J. Sandilands, Y. Tian, K. W. Plumb, Y.-J. Kim, and K. S. Burch, *Scattering Continuum and Possible Fractionalized Excitations in $\alpha-RuCl_3$,* Phys. Rev. Lett. **114**, 147201 (2015).

[71] V. S. de Carvalho, H. Freire, E. Miranda, and R. G. Pereira, *Edge magnetization and spin transport in an SU(2)-symmetric Kitaev spin liquid,* Phys. Rev. B **98**, 155105 (2018).

[72] T. Mizoguchi and T. Koma, *Majorana edge magnetization in the Kitaev honeycomb model,* Phys. Rev. B **99**, 184418 (2019).

[73] T. Mizoguchi, T. Koma, and Y. Yoshida, *Oriented propagation of magnetization due to chiral edge modes in Kitaev-type models,* Phys. Rev. B **101**, 014442 (2020).

[74] T. Minakawa, Y. Murakami, A. Koga, and J. Nasu, *Majorana-Mediated Spin Transport in Kitaev Quantum Spin Liquids,* Phys. Rev. Lett. **125**, 047204 (2020).

[75] D. Takikawa, M. G. Yamada, and S. Fujimoto, *Dissipationless spin current generation in a Kitaev chiral spin liquid,* Phys. Rev. B **105**, 115137 (2022).

[76] K. Nomura, S. Ryu, A. Furusaki, and N. Nagaosa, *Cross-Correlated Responses of Topological Superconductors and Superfluids,* Phys. Rev. Lett. **108**, 026802 (2012).

[77] M. Caselle, M. Hasenbusch, A. Pelissetto, and E. Vicari, *Irrelevant operators in the two-dimensional Ising model,* Journal of Physics A: Mathematical and General **35**, 4861 (2002).

[78] S. Fujimoto and N. Kawakami, *Drude Weight at Finite Temperatures for Some Nonintegrable Quantum Systems in One Dimension,* Phys. Rev. Lett. **90**, 197202 (2003).

[79] X.-Y. Liu, Y. Gao, H. Li, W. Jin, J. Xiang, H. Jin, Z. Chen, W. Li, and G. Su, *Quantum spin liquid candidate as superior refrigerant in cascade demagnetization cooling,* Communications Physics **5**, 1 (2022).

[80] D. Hirobe, M. Sato, T. Kawamata, Y. Shiomi, K.-i. Uchida, R. Iguchi, Y. Koike, S. Maekawa, and E. Saitoh, *One-dimensional spinon spin currents,* Nature Physics **13**, 30 (2017).

[81] A.-P. Jauho, N. S. Wingreen, and Y. Meir, *Time-dependent transport in interacting and noninteracting resonant-tunneling systems,* Phys. Rev. B **50**, 5528 (1994).

[82] L. Berger, *Emission of spin waves by a magnetic multilayer traversed by a current,* Phys. Rev. B **54**, 9353 (1996).

[83] J. Sinova, D. Culcer, Q. Niu, N. A. Sinitsyn, T. Jungwirth, and A. H. MacDonald, *Universal Intrinsic Spin Hall Effect,* Phys. Rev. Lett. **92**, 126603 (2004).

[84] Y. K. Kato, R. C. Myers, A. C. Gossard, and D. D. Awschalom, *Observation of the Spin Hall Effect in Semiconductors,* Science **306**, 1910 (2004), https://www.science.org/doi/pdf/10.1126/science.1105514 .

[85] J. Wunderlich, B. Kaestner, J. Sinova, and T. Jungwirth, *Experimental Observation of the Spin-Hall Effect in a Two-Dimensional Spin-Orbit Coupled Semiconductor System,* Phys. Rev. Lett. **94**, 047204 (2005).

[86] A. Azevedo, L. Vilela Leão, R. Rodriguez-Suarez, A. Oliveira, and S. Rezende, *dc effect in ferromagnetic resonance: Evidence of the spin-pumping effect?* Journal of applied physics **97**, 10C715 (2005).

[87] E. Saitoh, M. Ueda, H. Miyajima, and G. Tatara, *Conversion of spin current into charge current at room temperature: Inverse spin-Hall effect,* Applied physics letters **88**, 182509 (2006).

[88] S. O. Valenzuela and M. Tinkham, *Direct electronic measurement of the spin Hall effect,* Nature **442**, 176 (2006).

[89] H. Adachi, J.-i. Ohe, S. Takahashi, and S. Maekawa, *Linear-response theory of spin Seebeck effect in ferromagnetic insulators,* Phys. Rev. B **83**, 094410 (2011).

[90] J. Flipse, F. K. Dejene, D. Wagenaar, G. E. W. Bauer, J. B. Youssef, and B. J. van Wees, *Observation of the Spin Peltier Effect for Magnetic Insulators,* Phys. Rev. Lett. **113**, 027601 (2014).

[91] S. Daimon, R. Iguchi, T. Hioki, E. Saitoh, and K.-i. Uchida, *Thermal imaging of spin Peltier effect,* Nature communications **7**, 13754 (2016).

[92] W.-H. Kao and N. B. Perkins, *Disorder upon disorder: Localization effects in the Kitaev spin liquid,* Annals of Physics **435**, 168506 (2021), special issue on Philip W. Anderson